Pattern Formation of Active Filaments with Polar and Antipolar Interactions

TMP Master thesis
Faculty of Physics
Ludwig-Maximilians-Universität Munich

presented by
Filippo De Luca
born in Rome, Italy

Supervisor: Prof. Erwin Frey
Munich, October 17th, 2022

Abstract

Microtubule-motor mixtures are a prime example of how living matter self-organises into complex structures emerging from interactions between relatively simple constituents. Recently, experimental advances [1] found a novel non-equilibrium phase of matter in these mixtures known as active foams, consisting of a bilayer network that experiences continuous reconfiguration. Inspired by these results, we extend previously developed methods to rigorously derive continuum equations from microscopic models by considering asymmetric polar/antipolar interactions with antiparallel sliding. We find a transition linking radially symmetric micelles and active bilayer networks that crucially relies on the asymmetry of the interaction as well as the inhomogeneity of free motors. Moreover, we inspect the mechanisms that lead to the emergence of length scales and instabilities in the system, which allows us to characterise the branching instability occurring in the micelle-foam transition. Our work demonstrates the link between microscopic interactions and mesoscopic pattern formation and paves the way for higher-level theoretical studies on active foams.

Contents

Chapter 1

Introduction

A fascinating property of life is its ability to self-organise into more and more complex structures in a hierarchical manner. On each level of this hierarchy, elementary constituents interact among each other to give rise to functional collective behaviour at a larger scale [2]. During gene expression, amino acids are assembled to form proteins, which constitute the fundamental building block of life. Proteins engage in chemical reactions and exert mechanical forces, forming the machinery that is capable of providing the cell with the innumerable functions it needs to perform. Cells form tissues, tissues build organs and finally macroscopic organisms. While the self-organisation of each structure on this hierarchy relies on its elementary constituents, attempting to trace the complexity of living systems back to the most fundamental level would not only be frustratingly difficult, but also not particularly useful. Indeed, it is the study of how new mechanisms emerge on each scale that provides the deepest understanding of biological complexity. This is a consequence of the hierarchical nature of self-organisation.

A spectacular example of self-organisation on the cellular level is the mitotic spindle found in animal cells [3, 4]. During cell division, this adaptive machine is assembled from microtubules and molecular motor proteins in order to segregate chromosomes into the two daughter cells. Microtubules are hollow polymers built from tubulin dimers. They have an intrinsic polarity, exhibiting a plus end that can rapidly grow and shrink, as well as a more stable minus end. A wide variety of motor proteins can bind to the microtubules, in some cases crosslinking two filaments by binding to them simultaneously. Some of the molecular motors can walk in a directional manner along the microtubules. For most types of motors, the walking direction is fixed, i.e. they always walk towards the plus end or the minus end. By walking along the filaments, the motors can generate forces, which allow them to slide microtubules with respect to each other, leading to alignment and polarity sorting. The interaction that emerges between microtubules in this way, mediated by molecular motors, is one of the mechanisms driving mitotic spindle assembly.

The complexity of the assembly process is staggering. The microtubules in the spindle are dynamic, i.e. they undergo constant polymerisation and depolymerisation, while the motors appear in a large number of forms, exhibiting different behaviours and functions that are partly overlapping and partly competing. This complexity gives rise to a very robust spindle, which is able to undergo self-healing as well as fusion with other spindles [2]. Experiments in living cells, however, are quite difficult to control. To achieve greater freedom

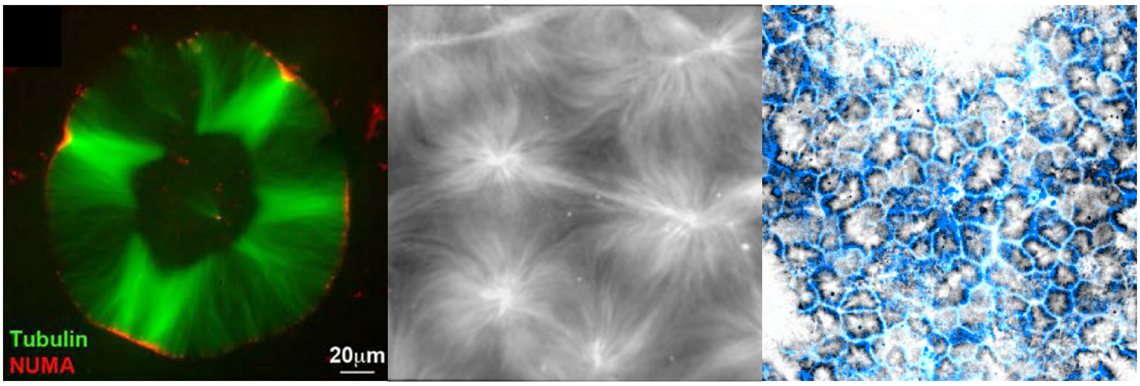

a) Micelle with open centre b) Aster network c) Active foam

Figure 1: a) Micelles with open centre in *Xenopus* meiotic extract, adapted with permission from [5]. NUMA (in red) accumulates at the minus ends of microtubules (shown in green). b) Network of asters in mixture of microtubules and kinesin clusters, adapted with permission from [6]. c) 2d slice of an active foam in microtubule-motor mixture, adapted with permission from [1]. The edges of the foam are bilayers where kinesin-4 (in blue) accumulates and microtubules (in black) have inward-pointing plus ends.

in changing experimental parameters while retaining high complexity, one approach is to inspect cytoskeletal pattern formation in cell-free extract systems. In 1992, Sawin *et al.* [7] could verify that the mitotic spindle is able to form in *Xenopus* egg extract when adding chemicals that stabilise microtubules (i.e. stop depolymerisation), but that the spindle fails to form when anti-kinesin-5 antibodies are added to the system, suggesting that the motors are essential for pattern formation. Sometimes, new patterns are observed: in [5], meiotic *Xenopus* egg cytosol was investigated. The experiment showed the formation of interconnecting bilayer-like structures, as well as round micelles with centres depleted of microtubules (see Fig. 1a).

Another approach is to design *in vitro* experiments from scratch, selecting a low number of constituents to verify which ingredients are necessary to reproduce the patterns seen in living cells. In 1997, Nédélec *et al.* [6] found that aster-like patterns formed in mixtures of kinesin motor clusters and stabilised microtubules. These asters (shown in Fig. 1b) had radial symmetry, with the plus ends of the filaments clustering in the centre and the minus ends extending outward. This reproduced a pattern found in the mitotic spindle, where aster-like structures form at the poles, albeit with opposite polarity, since the aster formation in the cell is driven by motors walking into the other direction.

In addition to reproducing biological pattern formation, the synthetic approach allows to explore a much larger phase space compared to the one realised *in vivo*. Thus, it allows to design simple experimental realisations of theoretical models, allowing for quantitative tests that can rarely be performed in living cells. Furthermore, bioinspired synthetic systems provide the opportunity to discover new phenomena, that can give fundamental insights into principles of non-equilibrium physics [2].

Recently, Lemma *et al.* [1] designed an experiment combining stabilised microtubules and plus-end-directed kinesin-4 motors in a three-dimensional chamber. They observed a plethora of active states in dependence on the microtubule density. At low densities, the microtubules organised into asters with kinesin-rich cores. Increasing the tubulin concentration, the asters gave way to contracting gels that over time generated 2d flat bilayer sheets, with microtubules oriented in opposite directions normally to the sheet. At even higher tubulin concentrations, the contracting gel showed surface roughening, where at the interface the initially forming monolayer with perpendicular microtubules developed spherical cavities. Finally, at the highest tubulin concentrations probed, the initially ordered homogeneous state became unstable, forming condensates with roughening monolayer surfaces. When two monolayers met, they formed bilayers, that later connected among each other to form a large-scale network. This bilayer-based foam-like network continuously rearranged over time, so the authors called it *active foam* (see Fig. 1c).

Inspired by these experimental results, the goal of this thesis is to develop a theory for microtubule-motor mixtures. There are several ways one could approach this task. In a phenomenological perspective, one writes down a continuum theory for the microtubule and motor densities, as well as the order parameter(s) of interest, including all terms allowed by symmetry. This is the approach taken by Lee and Kardar in [8], where they formulate a theory including the motor density and a polarisation field that undergoes Ginzburg-Landau ordering. While these theories have the advantage of having high generality, they fail to provide a microscopic explanation for the phenomena they can reproduce. If this is to be achieved, the formulation of a microscopic interaction model is needed.

Two interactions between microtubules are particularly relevant: the antiparallel sliding of microtubules, which leads to the separation of filaments pointing in opposite directions, and the clustering of the ends of a certain type, which aligns the tips of two parallel microtubules together [3, 9]. It has been shown that the same type of motor molecule can perform these two tasks. For example, the tetrameric motor kinesin-5, which is able to walk on two filaments simultaneously, can align microtubules in an antiparallel fashion and then slide them with respect to each other, or orient them in a parallel way while aligning their plus ends together, depending on their relative orientation [10]. Similarly, kinesin-4 can align plus ends together, as well as induce sliding of antiparallel filaments, at least in presence of PRC1 crosslinkers. Importantly, the antiparallel sliding does not have to be complete, i.e. fully separate the two filaments, since crowding effects in the overlapping area lead to stalling before the plus ends can meet [11].

These considerations suggest that a full theory of motor-mediated filament-filament interactions should include both polar and antipolar interactions, in dependence on the initial intersection angle. While early models, like the one by Aranson and Tsimring [12, 13], considered only polar interactions, both kinds of interactions are mixed in the model by Maryshev *et al.* [14]. This model considered a fully symmetric interaction, which aligns filaments in a parallel way for acute angles and in an antiparallel way for obtuse ones. This leads to a nematic order transition. At least some patterns seen in experiment, however, are inherently polar, like the bilayers in [1]. Hence, it seems reasonable to generalise these models by allowing both polar and antipolar interactions with a tuneable bias towards one or the other. For self-propelled particles, such a model was proposed in [15].

Once a microscopic model has been formulated, one option is to perform agent-based simulations. However, for large numbers of particles, this rapidly becomes computationally expensive. Moreover, the analytical tools that can be applied to an agent-based model are limited. Thus, the approach we follow is to coarse-grain the microscopic model and derive a continuum description in terms of the slow variables of the system, i.e. the conserved fields (the microtubule and motor densities) as well as the order parameter close to the threshold of the ordering transition [16]. There are several methods to derive such equations from microscopy.

One of these is the Smoluchowski approach, which starts from Langevin equations for the position and orientation of the N particles, from which an N-body Fokker-Planck equation is derived. This is reduced to a Smoluchowski equation for the single-particle PDF, from which the equations for the slow variables are extracted [16, 17]. The Smoluchowski approach was applied to microtubule-motor mixtures by several authors [18–22]. These models all take into account the possibility of polar and antipolar interactions, and an inhomogeneous motor density is included in [21]. However, only [22] inspected the nonlinear equations by means of numerical simulations, which were limited to densities below the ordering threshold.

Another way of deriving coarse-grained equations is the Boltzmann-Ginzburg-Landau (BGL) formalism used in [12–14, 17, 23–25]. This approach starts from a kinetic equation for the single-particle PDF. Interactions are assumed to take place instantly, unlike in the Smoluchowski approach. While this might be less realistic, the BGL formalism requires a smaller number of parameters to describe the interaction rules compared to the Smoluchowski approach, and these parameters provide an easier physical interpretation. This is the motivation that led us to choose this approach to develop our theory.

In the first part of the thesis, throughout chapter 2, we formulate a microscopic model that takes into account the properties of motor-induced interactions discussed above. In particular, we mix polar and antipolar interactions depending on the initial intersection angle, and we introduce a tuneable parameter to control the strength of the antipolar sliding. We discuss two levels of interaction anisotropy, one arising due to the inhomogeneous profile of bound motors, and one due to the inhomogeneous distribution of free motors across the system. Then, we apply the BGL formalism to our model and obtain continuum equations for the density and the order parameter, which will be polar or nematic order depending on the bias towards a polar interaction.

In the second part of the thesis, in chapter 3, we investigate the derived model using numerical simulations, and inspect its phase diagram, which features micelles, bilayers and active foams. Then, we discuss the effect of the terms in the equations on the dynamics and generalise the model to a phenomenological set of equations. We derive expressions for the stationary profiles of the bilayers and the micelles as well as the length scales emerging in these solutions, verifying our predictions by means of the phenomenological model. Finally, we discuss the stability of the homogenous state as well as the micelles, and discuss the role of the instabilities in the topology of the phase diagram of our continuum model.

Chapter 2

From Microscopy to Mesoscopy

The goal of this chapter is to coarse-grain a microscopic interaction model to obtain a description for microtubule-motor mixtures in terms of continuous fields. A continuum description is advantageous to study collective behaviour in many-particle systems, since it provides equations for the quantities of interest – the density and the order parameters – that are much easier to treat both analytically and numerically compared to agent-based models. Indeed, a hydrodynamic description makes it possible to use techniques from the theory of differential equations and to identify simple mechanisms in the equations that lead to the emergence of complex behaviour. Furthermore, it's certainly less cumbersome to simulate a handful of equations than a very large number of interacting agents. For many problems a rigorous derivation of hydrodynamic equations is highly challenging, if not impossible. In our case, however, such a derivation can be performed, with the right assumptions and approximations, by making use of the Boltzmann-Ginzburg-Landau formalism.

The first step in the coarse-graining procedure is to set up a microscopic model that takes into account the main characteristics of the interaction between microtubules mediated by molecular motors. It will be necessary to define the nature of the interaction, which we do in section 2.1.1, as well as the dependence of the interaction rate on the initial configuration of the microtubules, which we encode into an interaction kernel in section 2.1.2. We refine this kernel by taking into account inhomogeneities of the motor concentration both on individual microtubules and across the system in section 2.1.3.

Once the microscopic model has been constructed, we are ready to apply the Boltzmann-Ginzburg-Landau formalism. The fundament of this formalism is the kinetic equation, which determines the time evolution of the single-particle probability density function (PDF) for the microtubule configurations. We set up this equation in sec. 2.2.1. The fields of interest are the Fourier components of this PDF, as discussed in sec. 2.2.2. In sec. 2.2.3, we analyse the system neglecting the spatial dependence of the PDF. This allows us to determine which Fourier modes show exponential growth, which we identify as the slow variables of the system close to the threshold. We will find that there is a parameter regime for which the dominant order is nematic, as well as a regime where polar order dominates. Next, in sec. 2.2.4, we define a closure scheme that allows us to neglect higher-order Fourier modes consistently. This gives us all the necessary tools to reintroduce spatial dependence and derive the full equations. The terms arising due to diffusion and steric interactions are derived in 2.2.5, while the derivation of those emerging from the motor-mediated interaction is discussed in sec. 2.2.6. Finally, the resulting hydrodynamic equations for the nematic and polar regimes are detailed in sec. 2.3.

2.1 Setting up the microscopic model

2.1.1 Interaction rules

We model the microtubules as ideal, perfectly rigid rods. Thus, their only degrees of freedom are the position of their midpoints $\boldsymbol{r}$ and their orientation, which in 2d can be described by a single angle ϕ. Furthermore, we assume all rods to be of fixed length L, excluding any variation in length within the microtubule population. This means that the microtubules are stabilised, i.e. they do not undergo polymerisation and depolymerisation as they would in a cell environment [3]. However, investigating the role of different microtubule lengths is an interesting question to be tackled in further research.

Two microtubules can interact through the action of molecular motors. In the following, we denote the initial orientations of the two microtubules by $\phi_{1,2}$ and the initial positions of their midpoints by $\boldsymbol{r}_{1,2}$. We define:

$$\omega := \phi_2 - \phi_1, \tag{2.1}$$

$$\boldsymbol{s} := \boldsymbol{r}_2 - \boldsymbol{r}_1. \tag{2.2}$$

When an interaction takes place, the microtubules are aligned along the same axis. A polar interaction aligns them in a parallel way, while an antipolar interaction results in an antiparallel configuration. Inspired by experimental findings [10, 11], in our model the type of interaction is determined by the initial angle between the microtubules: we introduce a critical angle ω_c, such that the final configuration is parallel for $\omega \in (-\omega_c, \omega_c) \bmod 2\pi$ and antiparallel for $\omega \in (\omega_c, 2\pi - \omega_c) \bmod 2\pi$. Thus, the collision rule for the angles can be written as follows:

$$\begin{pmatrix} \phi_1' \\ \phi_2' \end{pmatrix} = \begin{pmatrix} 1/2 & 1/2 \\ 1/2 & 1/2 \end{pmatrix} \begin{pmatrix} \phi_1 \\ \phi_2 \end{pmatrix} + \chi_{\text{apol}}(\omega) \operatorname{sgn} \omega \begin{pmatrix} -\pi/2 \\ \pi/2 \end{pmatrix}, \tag{2.3}$$

where $\phi_{1,2}'$ are the final configurations of the two microtubules and χ_{apol} is the characteristic function of the interval $(\omega_c, 2\pi - \omega_c) \bmod 2\pi$, being 1 inside the interval and 0 outside. Note that a polar interaction aligns the filaments along their bisector, while an antipolar interaction aligns them along the axis perpendicular to it. We assume that the interactions are fully inelastic, i.e. they always result in total alignment. The interaction rules are summarised in Fig. 2. A similar tuneable admixture of polar and antipolar interactions was studied in [15] for a system of self-propelled particles.

As for the microtubule positions, we assume that the centre of mass is not affected by the interaction. Thus, we neglect any net displacement of the microtubule pair which can arise if the fluid friction tensor is anisotropic (see [19]). The remaining degree of freedom is relative sliding of the filaments with respect to each other. In a polar interaction, this leads to an alignment of the plus tips of the tubules, so that after the interaction the two microtubules have the same configuration in terms of both angles and position. On the other hand, in the case of an antipolar interaction, the motors slide the microtubules in opposite directions, separating them. We take this effect into account by introducing a parameter $\eta \in [0,1]$ that controls the amount of antipolar sliding, $\eta = 0$ signifying no sliding at all and $\eta = 1$ full sliding until the plus ends of the two microtubules are at the same position. This allows to capture stalling effects seen in experiments [11]. Hence, the midpoint positions change to:

$$\boldsymbol{r}'_{1,2} = \frac{\boldsymbol{r}_1 + \boldsymbol{r}_2}{2} - \chi_{\text{apol}}(\omega)\frac{\eta L}{2}\hat{\boldsymbol{n}}(\phi'_{1,2}), \tag{2.4}$$

where we have introduced the unit vector

$$\hat{\boldsymbol{n}}(\phi) = \begin{pmatrix} \cos\phi \\ \sin\phi \end{pmatrix}. \tag{2.5}$$

This model generalises the fully polar interactions ($\omega_c = \pi$) studied in [12, 13, 23] as well as the fully symmetric interactions with antipolar sliding ($\omega_c = \pi/2$) considered in [14].

2.1.2 Choosing an interaction kernel

Now that we have established what happens when an interaction takes place, we need to indicate with which rate interactions occur, and how this rate depends on the initial configuration of the microtubules. This information is encoded into the choice of the interaction kernel, which we construct in this section.

Since interactions between microtubules are mediated by molecular motors, we assume that the interaction rate is proportional to the free motor density m (which, as we will discuss below in sec. 2.1.3, is in turn proportional to the density of bound motors). As motors are much smaller than microtubules, the interaction is short-ranged: two microtubules can only interact if they intersect.

We introduce a contour parameter $\tau \in [0,1]$ that parametrises a microtubule from its plus end ($\tau = 0$) to its minus end ($\tau = 1$). At the point of intersection, this parameter will in general have different values for the two microtubules. We denote these values by $\tau_{1,2}$. They are fixed by the following intersection condition [23]:

$$\boldsymbol{r}_1 + L\left(\frac{1}{2} - \tau_1\right)\hat{\boldsymbol{n}}_1 = \boldsymbol{r}_2 + L\left(\frac{1}{2} - \tau_2\right)\hat{\boldsymbol{n}}_2, \tag{2.6}$$

where we have introduced the shorthand $\hat{\boldsymbol{n}}_{1,2} := \hat{\boldsymbol{n}}(\phi_{1,2})$. Now, taking the cross product of this equation with $\hat{\boldsymbol{n}}_{1,2}$, we obtain:

$$\tau_{1,2} = \frac{1}{2} - \frac{(\boldsymbol{s} \times \hat{\boldsymbol{n}}_{2,1}) \cdot \hat{\boldsymbol{e}}_z}{L \sin\omega} \tag{2.7}$$

The two microtubules intersect if both parameters are inside the range $[0,1]$.

Using this condition, and assuming that the interaction rate is constant for any microtubule configuration as long as the microtubules intersect, we write down the isotropic Heaviside kernel:

$$W_{\text{iso}}(\boldsymbol{s}; \phi_1, \phi_2) = Gm\Theta(\tau_1)\Theta(1-\tau_1)\Theta(\tau_2)\Theta(1-\tau_2). \tag{2.8}$$

The right hand side is dependent on the initial angles $\phi_{1,2}$ as well as the distance vector $\boldsymbol{s}$ via (2.7). Here G is a proportionality constant with units of area over time. In the following, we absorb the physical mean free motor density $\bar{m}_{\mathrm{ph}}$ into G, which then indicates the interaction rate at that density. This amounts to measuring m in units of its average, s.t. $\bar{m} \equiv 1$.

If we fix the center of mass of the first microtubule $\boldsymbol{r}_1$ at the origin, the Heaviside functions in the kernel (2.8) define a rhombus of side length L in which the second microtubule's midpoint $\boldsymbol{r}_2$ needs to be in order to give rise to an intersection, as shown in Figure 3a. The rhombus has opening angle ω and is oriented along the direction of the bisector angle $\bar{\phi}$, defined as:

$$\bar{\phi} := \frac{\phi_1 + \phi_2}{2}. \tag{2.9}$$

We denote this rhombus by $R_0(\bar{\phi}, \omega)$. It is convenient to introduce the following unit vectors:

$$\bar{\boldsymbol{n}} := \hat{\boldsymbol{n}}(\bar{\phi}), \tag{2.10a}$$

$$\bar{\boldsymbol{n}}_\perp := \hat{\boldsymbol{n}}(\bar{\phi} - \pi/2). \tag{2.10b}$$

They form a right-handed orthonormal basis $\{\bar{\boldsymbol{n}}_\perp, \bar{\boldsymbol{n}}\}$, in which we will decompose the vector $\boldsymbol{s} = \boldsymbol{r}_2 - \boldsymbol{r}_1$ as $\boldsymbol{s} = s_\parallel \bar{\boldsymbol{n}} + s_\perp \bar{\boldsymbol{n}}_\perp$.

2.1.3 Motor anisotropy on two scales

The assumption that the interaction rate is constant for all configurations as long as the microtubules intersect, which we built into the choice of the kernel (2.8), is not quite correct in real systems. Indeed, as shown in experiments [26], the concentration profile of bound molecular motors along the microtubules is not constant: due to low detachment rates at the plus ends of the microtubules, motors tend to get stuck in the vicinity of the tip. This anisotropy between the two microtubule ends emerges on the microscopic level, on individual microtubules. On the other hand, the concentration of free motors across the system is also not constant. As they bind to microtubules, walk towards their plus ends and detach, motors experience directed advection into other parts of the system. In highly ordered regions, where many microtubules point into the same direction, this advection results in large-scale displacement along the collective polarisation of the tubules. In regions of the system where motors accumulate, interactions will be more frequent than in other regions, which leads to an anisotropy of the system on the mesoscopic scale.

Anisotropy on the microscopic scale

As a first step, we investigate the anisotropy along individual microtubules, following the treatment in [13]. We introduce $\sigma := L(1 - \tau)$ as a 1d spatial coordinate along the tubule, running from 0 (minus end) to L (plus end). The concentration $M_b(\sigma, t)$ of bound motors along a microtubule obeys the following dynamics:

$$\partial_t M_b = -p_{\mathrm{off}} M_b + p_{\mathrm{on}} m - \partial_\sigma (v M_b), \tag{2.11}$$

where we have included a loss term due to detachment at a rate p_{off}, and a gain term proportional to the free motor density $m(\sigma, t)$ in the proximity of the microtubule, which reflects the attachment of motors at a rate p_{on}. The last term represents the advection of

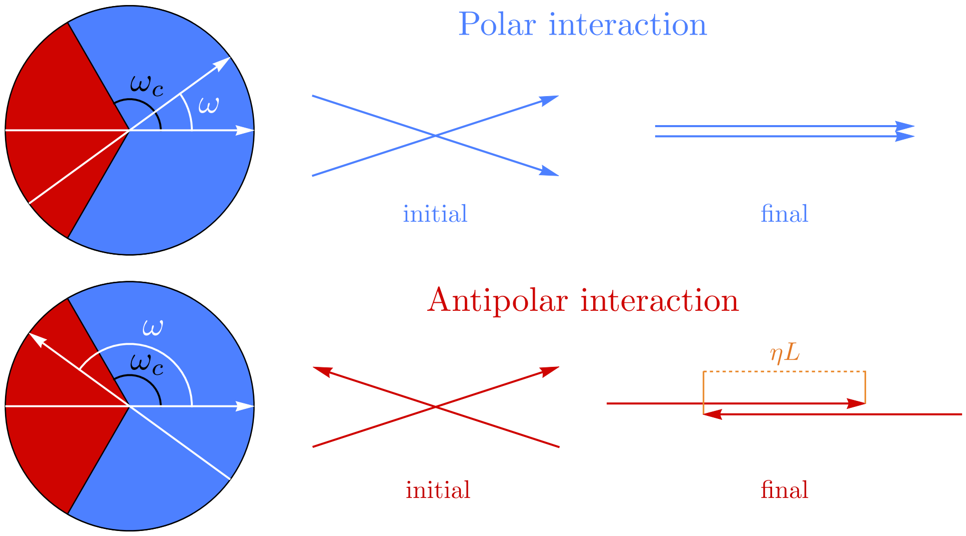

Figure 2: Interaction rules. We mix polar interactions, which lead to parallel alignment of the microtubules, and antipolar interactions with sliding (controlled by the parameter η), which lead to antiparallel alignment of the microtubules. The initial angle $\omega = \phi_2 - \phi_1$ between the microtubules determines whether the interaction is polar or antipolar: for $\omega \in (-\omega_c, \omega_c) \mod 2\pi$, the interaction is polar, while for $\omega \in (\omega_c, 2\pi - \omega_c) \mod 2\pi$ it is antipolar.

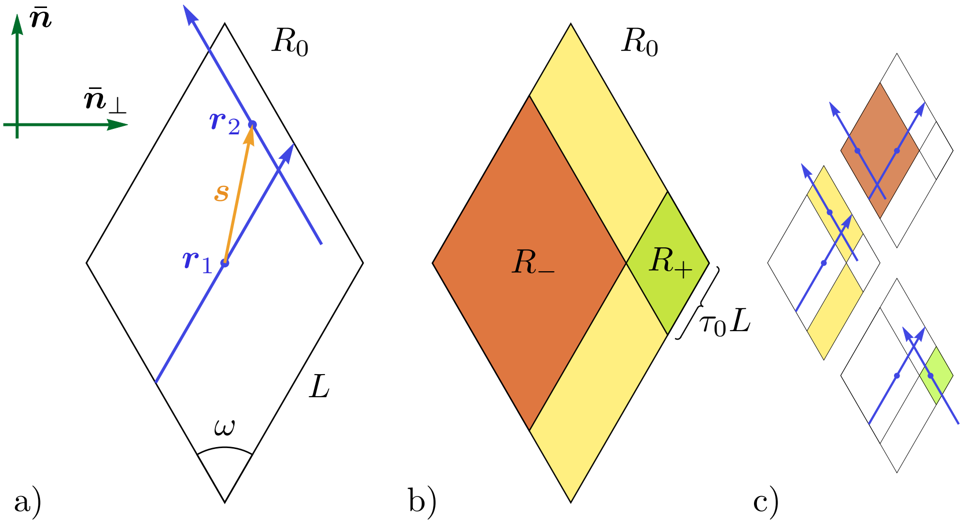

Figure 3: Definition of the rhombi for the interaction kernel. a) Fixing $\boldsymbol{r}_1$ at the origin, an intersection occurs if $\boldsymbol{r}_2$ is placed inside a rhombus of side length L and opening angle ω, oriented along the bisector $\bar{\phi} = \phi_2 - \phi_1$, which we denote as $R_0(\bar{\phi}, \omega)$. Defining an orthonormal basis $\{\bar{\boldsymbol{n}}_\perp, \bar{\boldsymbol{n}}\}$ as in eq. (2.10a), we can decompose the vector $\boldsymbol{s} = \boldsymbol{r}_2 - \boldsymbol{r}_1$ as $\boldsymbol{s} = s_\parallel \bar{\boldsymbol{n}} + s_\perp \bar{\boldsymbol{n}}_\perp$. b) The rhombi $R_+(\bar{\phi}, \omega)$ and $R_-(\bar{\phi}, \omega)$ are defined as shown, with side lengths $\tau_0 L$ and $(1 - \tau_0)L$, respectively. c) When $\boldsymbol{r}_2$ is placed in the rhombus R_- (red area), the intersection point is in the gas phase for both tubules and the interaction rate will be the lowest; when it is placed in R_+ (green area), the intersection occurs in the solid phase for both tubules and the interaction rate will be the highest. Finally, in the regions in yellow, $R_0 \setminus (R_- \cup R_+)$, the intersection is in the solid phase for one tubule and in the gas phase for the other, leading to intermediate interaction strength.

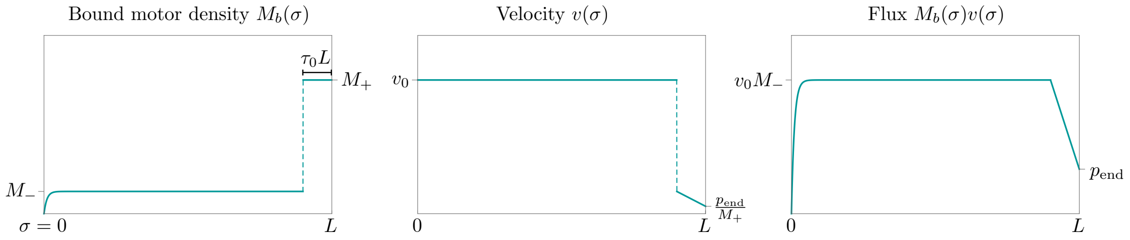

Figure 4: Microscopic anisotropy. The profile of bound motors along an individual microtubule separates into a low density ("gas") phase and a high density ("solid") phase. The density in the gas phase is determined by the attachment and detachment rates and the density of free motors in the vicinity of the tubule, see eq. (2.14). The density in the solid state is equal to the maximum possible density of one motor per attachment site. The high density phase emerges due to slow detachment at the plus end: while in the gas phase motors walk with their unhindered velocity v_0, for low enough rates p_end, there are more motors incoming than can detach at the end of the tubule, and a "traffic jam" occurs, with high densities and slow velocities. The position of the interface between the two phases, τ_0, is determined by requiring that the flux be continuous, see eq. (2.17).

the motors along the tubule, with a velocity v that can depend on the position along the tubule.

At the plus end, motors can detach one at a time at a rate p_end. Due to the discrete nature of the microtubules, which are tubulin polymers, the motor density is capped from above: if ℓ_0 is the length of an attachment site, which can carry only one motor at a time, the maximum density $M_+ = 1/\ell_0$ cannot be exceeded. If p_end is sufficiently low, motors will get stuck in the vicinity of the microtubule tip, as they wait for the motors preceding them to detach.

Near the minus end of the tubule, on the other hand, we can assume that the motor density is low enough to make steric effects negligible. Then, nothing hinders the motors from walking freely down the tubule, so that the advection velocity of the motors can be set constant, $v = v_0$. Requiring stationarity in eq. (2.11) yields:

$$0 = -p_\text{off} M_b(\sigma) + p_\text{on} m(\sigma) - v_0 \partial_\sigma M_b(\sigma). \tag{2.12}$$

If, for the time being, we assume the concentration profile of the free motors to be constant over the length scale of the microtubule, $m(\sigma) = m_0$, we can solve this differential equation with the boundary condition $M_b(\sigma = 0) = 0$, obtaining an exponential profile:

$$M_b(\sigma) = \frac{p_\text{on}}{p_\text{off}} m_0 \left[1 - \exp\left(-\frac{p_\text{off}}{v_0}\sigma\right)\right], \tag{2.13}$$

which for $v_0/p_\text{off} \ll L$, i.e. for a typical walking distance before detachment which is much smaller than the microtubule length, quickly saturates to $M_b(\sigma) = M_-$, with

$$M_- = \frac{p_\text{on}}{p_\text{off}} m_0. \tag{2.14}$$

Near the end of the microtubule, on the other hand, we know that due to the traffic jam the motor density is constant, $M_b = M_+$, while the velocity, being affected by the high packing of motors, can vary spatially. Thus, eq. (2.11) at stationarity gives a differential equation for $v(\sigma)$:

$$0 = -p_{\text{off}} M_+ + p_{\text{on}} m_0 - M_+ \partial_\sigma v(\sigma). \tag{2.15}$$

The boundary condition here is given by the conservation of motors at the tip of the tubule, i.e. by the balance of the advective flux $M_+ v(\sigma = L)$ and the detachment flux p_{end}. We obtain:

$$M_+ v(\sigma) = p_{\text{end}} + (p_{\text{off}} M_+ - p_{\text{on}} m_0)(L - \sigma). \tag{2.16}$$

The position τ_0 of the interface between the low density ("gas") and high density ("solid") phases can be estimated by requiring that the respective advective fluxes balance, yielding the condition:

$$v_0 M_- = p_{\text{end}} + (p_{\text{off}} M_+ - p_{\text{on}} m_0) L \tau_0,$$

where the left hand side indicates the constant flux in the gas phase. This can be solved for τ_0 to give:

$$\tau_0 = \frac{v_0}{p_{\text{off}} L} \left(1 - \frac{p_{\text{end}}}{v_0 M_-}\right) \left(\frac{M_+}{M_-} - 1\right)^{-1}. \tag{2.17}$$

From this equation, we can read off the condition for traffic jam to occur: we have $\tau_0 > 0$ for $p_{\text{end}} < v_0 M_-$, i.e. a high-density phase of non-vanishing size emerges near the tip of the microtubule when the tip detachment rate p_{end} is too low to guarantee the timely detachment of the incoming motors, which have flux $v_0 M_-$ in the gas phase. Furthermore, the interface position is affected by the characteristic walking distance of a motor v_0/p_{off}, as well as the ratio of the motor densities in the two phases.

The different motor densities in the two phases will lead to different interaction rates depending on the point of intersection. We assume the rates to be proportional to the combined densities of bound motors on the two filaments, i.e. $2M_-$ for an intersection in the gas phase for both tubules, $M_+ + M_-$ for an intersection which is in the gas phase for one tubule and in the solid phase for the other, and $2M_+$ for an intersection in the solid phase. Given that the tubules intersect, the rate should therefore have the form:

$$W \sim M_- \left\{1 + \Xi \left[\Theta(\tau_0 - \tau_1) + \Theta(\tau_0 - \tau_2)\right]\right\},$$

where we introduced

$$\Xi = \frac{1}{2}\left(\frac{M_+}{M_-} - 1\right) \tag{2.18}$$

as a parameter quantifying the difference in densities between the two phases. Since $M_- \sim m$ (see eq. (2.14)), we can absorb the proportionality factor into G and write down the full kernel as:

$$W = W_{\text{iso}}\{1 + \Xi\left(\Theta(\tau_0 - \tau_1) + \Theta(\tau_0 - \tau_2)\right]\}, \tag{2.19}$$

with the isotropic part W_{iso} from eq. (2.8). These Heaviside functions also define rhombic domains in which the intersection rate is increased, which we show in Fig. 3b-c.

It is interesting to consider the $M_+ \gg M_-$ limit, in which the accumulation at the tip is very strong. In this limit, the parameters defined above have singular behaviour, $\Xi \to \infty$ and $\tau_0 \to 0$. However, the quantity

$$\xi := 2\Xi\tau_0 = \frac{v_0}{p_{\text{off}} L}\left(1 - \frac{p_{\text{end}}}{v_0 M_-}\right). \tag{2.20}$$

stays finite. Taking this limit allows us to understand the effect of microscopic anisotropy in a simpler way, since it reduces the number of parameters needed to describe it from two (Ξ and τ_0) to one (ξ).

Anisotropy on the mesoscopic scale

As we mentioned at the beginning of this section, the inhomogeneity of the free motor concentration results in an anisotropy on the mesoscopic scale. It can be built into the theory by assuming the following dynamic equation for the free motors [8, 13]:

$$\partial_t m = D_m \nabla^2 m - v_m \boldsymbol{\nabla}(\boldsymbol{p} m). \tag{2.21}$$

The first term of this equation represents diffusion, with diffusivity D_m. The second term, on the other hand, reflects the advection of motors in ordered regions. Here, we introduced the polarisation $\boldsymbol{p} = \langle \rho \hat{\boldsymbol{n}} \rangle$ as the local expectation value of the orientation times the MT density, and assume that as this becomes non-zero the motors are advected at a velocity given by $v_m \boldsymbol{p}$. It is useful to introduce the Péclet number γ, which is the ratio of the characteristic diffusive and advective times over the length of a microtubule [27]:

$$\gamma := \frac{t_{\text{diff}}}{t_{\text{adv}}} = \frac{L^2/D_m}{L/v_m} = \frac{v_m L}{D_m}. \tag{2.22}$$

Since the dynamics of the motor field will be much faster than that of the filaments, we can assume quasi-stationarity. A stationary solution of eq. (2.21) in which the diffusive and advective fluxes balance out has:

$$\boldsymbol{\nabla} m = \frac{1}{L} \gamma m \boldsymbol{p}. \tag{2.23}$$

The gradients in the free motor concentration hence follow the direction of the collective order, with an amplitude that depends on γ and the polarisation strength. The characteristic length scale on which m varies is then given by $\ell_m = m/|\boldsymbol{\nabla} m| = |\boldsymbol{p}|^{-1}\gamma^{-1}L$. In the following, we will assume $\gamma \ll 1$, so that the inhomogeneity in the motor concentration is relevant for length scales much larger than the length of a microtubule, $L \ll \ell_m$. This motivates the choice $m = m_0$ in the derivation above. Furthermore, this allows us to neglect the dependence of m on space in the following derivation, and promote it back to a field at the end, the only requirement being that mass conservation must be fulfilled. A derivation is also possible keeping the motor field inhomogeneous from the start; however, the extra terms one obtains are of order $\mathcal{O}(\gamma)$.

2.2 The Boltzmann-Ginzburg-Landau formalism

Now that we have designed a microscopic model for our system, we are ready to derive coarse-grained continuum equations using the Boltzmann-Ginzburg-Landau formalism.

2.2.1 The kinetic equation

The object describing a single microtubule statistically is the one-particle probability density function $P(\boldsymbol{r}, \phi)$. The probability of finding the microtubule at a position inside the infinitesimal rectangle $[\boldsymbol{r}, \boldsymbol{r} + dx\hat{\boldsymbol{e}}_x + dy\hat{\boldsymbol{e}}_y]$ and at an angle inside the infinitesimal interval $[\phi, \phi + d\phi]$ is given by $P(\boldsymbol{r}, \phi)dxdyd\phi$.

Assuming that we have a sufficiently large ensemble of microtubules, and the individual microtubules are identically distributed, we can now reinterpret this probability density function as a mean concentration of particles in the infinitesimal domain of phase space around the point $(\boldsymbol{r}, \phi)$, such that the integral over the entirety of phase space gives the total number of particles:

$$\int_{\mathbb{R}^2} \mathrm{d}^2 r \int_0^{2\pi} \mathrm{d}\phi \, P(\boldsymbol{r}, \phi) = N_{tot}. \tag{2.24}$$

In addition to the binary interactions (collisions) defined in sec. 2.1.1, we consider diffusion of the microtubules as well as steric (excluded volume) interactions. Thus, the time evolution of the probability density function will involve three terms:

$$\partial_t P(\boldsymbol{r}, \phi) = I_{\text{diff}} + I_{\text{excl}} + I_{\text{coll}} \tag{2.25}$$

The diffusive part I_{diff} involves rotational and translational diffusion:

$$I_{\text{diff}} = D_r \partial_\phi^2 P(\boldsymbol{r}, \phi) + \partial_i D_{ij} \partial_j P(\boldsymbol{r}, \phi), \tag{2.26}$$

where D_r is a rotational diffusion constant with dimension $[t^{-1}]$, and D_{ij} is a translational diffusion tensor with dimension $[L^2/t]$. The tensor can be decomposed into a longitudinal and perpendicular part:

$$D_{ij} = D_\| n_i n_j + D_\perp (\delta_{ij} - n_i n_j).$$

For rigid rodlike molecules, as shown in [13], the following relation holds:

$$D_\| = \frac{L^2}{24} D_r = 2 D_\perp. \tag{2.27}$$

The excluded volume part I_{excl} can be derived from a term reminiscent of the Smoluchowski equation:

$$I_{\text{excl}} = \partial_i D_{ij} [P(\boldsymbol{r}, \phi) \partial_j U], \tag{2.28}$$

where the role of the external potential U is taken by a self-consistent potential that can be derived from an Onsager free energy. Following [23], we include two-body and three-body interactions, so that the resulting self-consistent potential reads:

$$U = \frac{2}{\pi} L^2 \rho(\boldsymbol{r}) + \frac{1}{4\pi} L^4 \rho(\boldsymbol{r})^2.$$

Finally, the collision part of eq. (2.25) contains gain and loss terms, like they would appear in a master equation:

$$I_{\text{coll}} = I_{\text{gain}}^{\text{pol}} + I_{\text{gain}}^{\text{apol}} - I_{\text{loss}}. \tag{2.29}$$

The gain term consists of an integral over all configurations that result in the configuration $(\boldsymbol{r}, \phi)$ via an interaction event. Thus, $\boldsymbol{r}$ and ϕ can be identified with $\boldsymbol{r}_1'$ and ϕ_1' in the collision rules (2.3) and (2.4). With $\phi_{1,2}$ and $\boldsymbol{r}_{1,2}$ denoting the configurations before the interaction, the full gain has the form:

$$I_{\text{gain}} = \int\limits_{S^1} \mathrm{d}\omega \int\limits_{\mathbb{R}^2} \mathrm{d}^2 s\, W(\boldsymbol{s}; \phi_1, \phi_2) P(\boldsymbol{r}_1; \phi_1) P(\boldsymbol{r}_2; \phi_2). \tag{2.30}$$

W is the chosen interaction kernel, in our case the Heaviside kernel from eq. (2.19). By writing the collision integral as we did here, we are incorporating two assumptions. The first assumption is that the dominant contribution is coming from *binary collisions*, which allows us to neglect the possibility of more than two microtubules interacting at the same time. The second assumption is the *molecular chaos hypothesis*, which states that the particles decorrelate between interaction events, such that we can factorise the two-particle PDF into two single-particle PDFs as we did in the collision integral. These two assumptions are likely to be fulfilled when the system is dilute enough to ensure a length scale separation between the interaction radius and the typical distance between microtubules, as well as a time scale separation between the duration of an interaction event and the time passing between two collisions [17]. As discussed in [24], however, the validity of the molecular chaos hypothesis in particular is not obvious, which makes a full quantitative correspondence between the microscopic level and the continuum model derived from a Boltzmann-type kinetic equation difficult to achieve.

Due to the presence of χ_{apol} in the collision rules, the form of the terms in (2.30) will be different for polar and antipolar interactions. Solving for $\phi_{1,2}$ and $\boldsymbol{r}_{1,2}$ in (2.3) and (2.4), and plugging the expressions into (2.30), we find:

$$I_{\text{gain}}^{\text{pol}} = \int_{-\omega_c}^{\omega_c} \mathrm{d}\omega \int\limits_{\mathbb{R}^2} \mathrm{d}^2 s\, W(\boldsymbol{s}; \phi_-, \phi_+) P(\boldsymbol{r}_-; \phi_-) P(\boldsymbol{r}_+; \phi_+), \tag{2.31a}$$

$$I_{\text{gain}}^{\text{apol}} = \int_{\omega_c}^{2\pi-\omega_c} \mathrm{d}\omega \int\limits_{\mathbb{R}^2} \mathrm{d}^2 s\, W\left(\boldsymbol{s}; \phi_- + \frac{\pi}{2}, \phi_+ + \frac{\pi}{2}\right) P\left(\boldsymbol{r}_-^{(\eta)}; \phi_- + \frac{\pi}{2}\right) P\left(\boldsymbol{r}_+^{(\eta)}; \phi_+ + \frac{\pi}{2}\right), \tag{2.31b}$$

where we have used the abbreviations:

$$\boldsymbol{r}_\pm = \boldsymbol{r} \pm \frac{\boldsymbol{s}}{2}, \quad \boldsymbol{r}_\pm^{(\eta)} = \boldsymbol{r}_\pm + \frac{\eta L}{2} \bar{\boldsymbol{n}}_\perp, \quad \phi_\pm = \phi \pm \frac{\omega}{2}.$$

Note that the angle $\bar{\phi} = (\phi_1 + \phi_2)/2$ used in the definition (2.10a) of the base vectors $\{\bar{\boldsymbol{n}}_\perp, \bar{\boldsymbol{n}}\}$ differs for the two integrals by a shift of $\pi/2$. This is why in the definition of $\boldsymbol{r}_\pm^{(\eta)}$ we have $\bar{\boldsymbol{n}}_\perp = \hat{\boldsymbol{n}}(\bar{\phi} - \pi/2) = \hat{\boldsymbol{n}}(\phi)$: the sliding occurs along the axis of the final microtubule orientation, which is perpendicular to the initial bisector of the microtubules.

The loss term considers all the possible interactions that involve microtubules in the current configuration $(\boldsymbol{r}, \phi)$, which will be changed as a consequence of an interaction event. The final configuration does not matter here, which is why a distinction between polar and antipolar interactions is not necessary. $(\boldsymbol{r}, \phi)$ thus takes the role of $(\boldsymbol{r}_1, \phi_1)$ in (2.3) and (2.4). The resulting integral reads:

$$I_{\text{loss}} = \int_{-\pi}^{\pi} \mathrm{d}\omega \int\limits_{\mathbb{R}^2} \mathrm{d}^2 s\, W(\boldsymbol{s}; \phi, \phi + \omega)\; P(\boldsymbol{r}; \phi)\; P(\boldsymbol{r} + \boldsymbol{s}; \phi + \omega). \tag{2.31c}$$

In the following, we use the Heaviside kernel (2.19) as the interaction kernel. It is convenient to introduce the equation below for collision integrals involving this kernel:

$$\begin{aligned}\int\limits_{W(\bar{\phi},\omega)} \mathrm{d}^2 s\, f(\boldsymbol{s}) &:= \int\limits_{\mathbb{R}^2} \mathrm{d}^2 s\, W(\boldsymbol{s};\phi_1,\phi_2) f(\boldsymbol{s}) \\ &= Gm \left[(1+\Xi) \int\limits_{R_0(\phi,\omega)} \mathrm{d}^2 s\, f(\boldsymbol{s}) + \Xi \int\limits_{R_+(\phi,\omega)} \mathrm{d}^2 s\, f(\boldsymbol{s}) - \Xi \int\limits_{R_-(\phi,\omega)} \mathrm{d}^2 s\, f(\boldsymbol{s}) \right], \qquad (2.32)\end{aligned}$$

where $f(\boldsymbol{s})$ is any function that may depend on other variables in addition to the integration variable $\boldsymbol{s}$, and the rhombi $R_{0,\pm}$ are defined in Figure 3.

2.2.2 Expansion in angular Fourier modes

Since the angle ϕ is 2π-periodic, we can expand the single-particle PDF as a Fourier series:

$$P(\boldsymbol{r};\phi) = \sum_{k=-\infty}^{\infty} P_k(\boldsymbol{r}) e^{ik\phi}. \qquad (2.33)$$

The Fourier modes $P_k(\boldsymbol{r})$ can be extracted via the formula:

$$P_k(\boldsymbol{r}) = \frac{1}{2\pi} \int_0^{2\pi} \mathrm{d}\phi e^{-ik\phi} P(\boldsymbol{r};\phi).$$

We have $P_{-k}(\boldsymbol{r}) = P_k^*(\boldsymbol{r})$, which follows from $P(\boldsymbol{r};\phi)$ being a real function.

The Fourier modes have a physical interpretation. Indeed, the 0th, 1st and 2nd modes correspond to the density, the polarisation and the nematic tensor, respectively [23]:

$$\rho(\boldsymbol{r}) = \int_0^{2\pi} \mathrm{d}\phi P(\boldsymbol{r},\phi) = 2\pi P_0(\boldsymbol{r}), \qquad (2.34a)$$

$$\boldsymbol{p}(\boldsymbol{r}) = \int_0^{2\pi} \mathrm{d}\phi \begin{pmatrix} \cos\phi \\ \sin\phi \end{pmatrix} P(\boldsymbol{r},\phi) = 2\pi \begin{pmatrix} \mathrm{Re}\, P_{-1} \\ \mathrm{Im}\, P_{-1} \end{pmatrix}, \qquad (2.34b)$$

$$\begin{pmatrix} Q_{xx}(\boldsymbol{r}) \\ Q_{xy}(\boldsymbol{r}) \end{pmatrix} = \int_0^{2\pi} \mathrm{d}\phi \begin{pmatrix} \cos 2\phi \\ \sin 2\phi \end{pmatrix} P(\boldsymbol{r},\phi) = 2\pi \begin{pmatrix} \mathrm{Re}\, P_{-2} \\ \mathrm{Im}\, P_{-2} \end{pmatrix}. \qquad (2.34c)$$

Thus, obtaining the time evolution of the density and the order parameters corresponds to the task of finding the time evolution of the Fourier modes of the PDF. Note that this definition of the polarisation and nematic tensor order parameters implicitly includes the concentration of particles, i.e. $p_i = \langle \rho n_i \rangle$ and $Q_{ij} = 2\,\langle \rho(n_i n_j - \delta_{ij}/2) \rangle$.

2.2.3 The spatially homogeneous system

We can already obtain some information about the collective behaviour of the microtubule-motor mixture by analysing a spatially homogeneous system, in which $P(\boldsymbol{r},\phi) = P(\phi)$. We immediately see that only rotational diffusion and collisions will play a role in such a system, since translational diffusions and excluded volume interactions matter in the presence of spatial gradients of the PDF. In the collision integrals (2.31), we can pull out the PDF terms from the spatial integrals, s.t. we are left to calculate the integral (2.32) with $f(\boldsymbol{s}) = 1$. This is nothing more than a weighted sum over the areas of the rhombi in Fig. 3b. A rhombus with side length d and aperture ω has area $L^2|\sin\omega|$. Weighting the different rhombi gives us:

$$\int_{W(\phi,\omega)} \mathrm{d}^2 s = Gm[(1+\Xi) + \Xi\tau_0 - \Xi(1-\tau_0)]L^2|\sin\omega| = Gm(1+a_1)L^2|\sin\omega|, \tag{2.35}$$

where $a_1 = 2\Xi\tau_0$. For brevity, we will set $a_1 = 0$ for now and restore it later. Plugging this result into the kinetic equation (2.25) gives:

$$\begin{aligned}\partial_t P(\phi) = {} & GL^2 m \int_{-\omega_c}^{\omega_c} \mathrm{d}\omega\, |\sin\omega| P(\phi_-)P(\phi_+) \\ & + GL^2 m \int_{\omega_c}^{2\pi-\omega_c} \mathrm{d}\omega\, |\sin\omega| P\left(\phi_- + \frac{\pi}{2}\right) P\left(\phi_+ + \frac{\pi}{2}\right) \\ & - GL^2 m \int_{-\pi}^{\pi} \mathrm{d}\omega\, |\sin\omega| P(\phi+\omega)P(\phi) - D_r \partial_\phi^2 P(\phi). \end{aligned} \tag{2.36}$$

We can make the equations dimensionless by choosing to measure time in units of the characteristic time of rotational diffusion D_r^{-1} and space in units of the microtubule length L. The PDF, being a density, is then measured in units of $1/L^2$. Additionally, to simplify the equations, we rescale the PDF by the ratio between the characteristic time scales of interaction and rotational diffusion, which we denote as $\alpha := D_r/G$:

$$t \to D_r t \tag{2.37a}$$

$$x \to x/L, \tag{2.37b}$$

$$P \to \alpha^{-1} L^2 \cdot P. \tag{2.37c}$$

Note that in eq. (2.8) we had absorbed the physical mean motor density $\bar{m}_{\mathrm{ph}}$ into the definition of G. Hence, $\alpha \sim 1/\bar{m}_{\mathrm{ph}}$. Hence, the rescaling (2.37) absorbs the physical mean motor density into the field ρ, while the field m takes into account deviations from the mean value of the motor field.

With this rescaling, equation (2.36) is simplified to:

$$\begin{aligned}\partial_t P(\phi) = {} & m \int_{-\omega_c}^{\omega_c} \mathrm{d}\omega\, |\sin\omega| P(\phi_-)P(\phi_+) + m \int_{\omega_c}^{2\pi-\omega_c} \mathrm{d}\omega\, |\sin\omega| P\left(\phi_- + \frac{\pi}{2}\right) P\left(\phi_+ + \frac{\pi}{2}\right) \\ & - m \int_{-\pi}^{\pi} \mathrm{d}\omega\, |\sin\omega| P(\phi+\omega)P(\phi) - \partial_\phi^2 P(\phi). \end{aligned}$$

Plugging in the Fourier transform (2.33), we find:

$$\begin{aligned}\partial_t \sum_k P_k e^{ik\phi} = {} & \sum_{k,q} e^{i(k+q)\phi} m P_k P_q \left(I_\omega^{\mathrm{pol}}(k-q) + e^{i(k+q)\pi/2} I_\omega^{\mathrm{apol}}(k-q) - I_\omega^{\mathrm{loss}}(q)\right) \\ & - \sum_k k^2 P_k, \end{aligned} \tag{2.38}$$

where we have introduced a shorthand for the ω integrals:

$$I_\omega^{\text{pol}}(k) = \int_{-\omega_c}^{\omega_c} \mathrm{d}\omega\, |\sin\omega| e^{ik\omega/2} = 2\int_0^{\omega_c} \mathrm{d}\omega \sin\omega \cos\frac{k\omega}{2} \tag{2.39a}$$

$$I_\omega^{\text{apol}}(k) = \int_{\omega_c}^{2\pi-\omega_c} \mathrm{d}\omega\, |\sin\omega| e^{ik\omega/2} = \begin{cases} 2\int_{\omega_c}^{\pi} \mathrm{d}\omega \sin\omega \cos\frac{k\omega}{2} & \text{for } k \text{ even,} \\ 2i\int_{\omega_c}^{\pi} \mathrm{d}\omega \sin\omega \sin\frac{k\omega}{2} & \text{for } k \text{ odd,} \end{cases} \tag{2.39b}$$

$$I_\omega^{\text{loss}}(k) = \int_{-\pi}^{\pi} \mathrm{d}\omega\, |\sin\omega| e^{-ik\omega} = 2\int_0^{\pi} \mathrm{d}\omega \sin\omega \cos(k\omega). \tag{2.39c}$$

We now project equation (2.38) onto the k-th Fourier mode to obtain its time evolution:

$$\partial_t P_k = \sum_q m P_q P_{k-q} \left(I_\omega^{\text{pol}}(k-2q) + e^{ik\pi/2} I_\omega^{\text{apol}}(k-2q) - I_\omega^{\text{loss}}(q) \right) - k^2 P_k. \tag{2.40}$$

To assess whether the mode will experience exponential growth or decay, we are interested in the terms proportional to P_k in this equation. We observe that only the choices $q = 0$ and $q = k$ will produce such terms in the sum above. Using the symmetry properties of the integrals defined above, we obtain:

$$\partial_t P_k = \left[\left(2I_\omega^{\text{pol}}(k) + (-1)^{k/2}(1+(-1)^k) I_\omega^{\text{apol}}(k) - I_\omega^{\text{loss}}(k) - 4 \right) \frac{m\rho}{2\pi} - k^2 \right] P_k + \cdots . \tag{2.41}$$

The equations for $k = \pm 1$ and $k = \pm 2$ show exponential growth for sufficiently large densities in a specific range of critical angles ω_c. Using the definitions (2.34) in (2.41), the resulting equations for the polarisation and nematic tensor can be written as:

$$\partial_t \boldsymbol{p} = \left(\frac{m\rho}{\rho_c^{(p)}} - 1 \right) \boldsymbol{p} + \cdots , \tag{2.42a}$$

$$\partial_t Q_{ij} = 4 \left(\frac{m\rho}{\rho_c^{(n)}} - 1 \right) Q_{ij} + \cdots . \tag{2.42b}$$

The polar and nematic critical densities read (see appendix A.1 for derivation):

$$\rho_c^{(p)} = \frac{3\pi}{2(1+a_1)\left[1 - 3\cos\left(\frac{\omega_c}{2}\right) - \cos\left(\frac{3\omega_c}{2}\right)\right]}, \tag{2.43a}$$

$$\rho_c^{(n)} = \frac{12\pi}{-(1+a_1)[1 + 3\cos(2\omega_c)]}, \tag{2.43b}$$

where we have reintroduced a_1. In the range of ω_c where $\rho_c > 0$, the corresponding order undergoes a Ginzburg-Landau transition for $m\rho > \rho_c$, acquiring a non-vanishing value [25].

On the other hand, the Fourier modes for which the square bracket in eq. (2.41) is negative will have fast dynamics compared to that of the density and the order parameter(s) close to the critical density. Hence, we can assume that on the relevant time scale of the dynamics, which is much longer than the relaxation time of these Fourier modes, they are always in equilibrium, and we are allowed to adiabatically eliminate them by setting $\partial_t P_k = 0$.

Their value is then imposed by the slow variables. In appendix A.1, we show that Fourier modes with $|k| > 2$ exhibit exponential decay independently on ω_c and $m\rho$, and therefore we can always adiabatically eliminate them. On the other hand, the polar and nematic orders can be adiabatically eliminated only in certain regions of the parameter space.

The sign of $\rho_c^{(p,n)}$ in eq. (2.43) depends exclusively on the critical angle ω_c, since $a_1 > 0$. The ω_c line is therefore divided into four domains (see Fig. 5):

(I) When $\rho_c^{(p,n)} < 0$, no orientational order can emerge. This is the case for $\omega_c \lesssim 55°$. In this regime, antipolar interactions occur even for small intersection angles. Since such an interaction aligns the tubules along the axis perpendicular to the bisector, any order that may emerge is disrupted.

(II) When $\rho_c^{(p)} < 0 < \rho_c^{(n)}$, nematic order is a slow variable exhibiting an ordering transition, while polar order can be adiabatically eliminated. This occurs in the range $55° \lesssim \omega_c \lesssim 102°$. In particular, this regime contains the fully symmetric ($\omega_c = \pi/2$) polar-antipolar interactions considered in [14].

(III) When $\rho_c^{(p,n)} > 0$, both polar and nematic order show an ordering transition. The relevant range is $102° \lesssim \omega_c \lesssim 125°$. In general, no adiabatic elimination can be performed, unless we assume that the densities stay below the critical density for one of the two kinds of order:

  (III-n) For $\omega_c \lesssim 108°$, polar order can be eliminated as long as $m\rho < \rho_c^{(p)}$ holds everywhere.

  (III-p) For $108° \lesssim \omega_c$, nematic order can be eliminated as long as $m\rho < \rho_c^{(n)}$ holds everywhere.

(IV) Finally, when $\rho_c^{(n)} < 0 < \rho_c^{(p)}$, i.e. for $125° \lesssim \omega_c \leq 180°$, polar order is the slow variable, while the dynamics of the nematic order is fast. This regime contains the fully polar interactions ($\omega_c = \pi$) considered in [12, 13, 23].

As is typical for Ginzburg-Landau transitions, the exponential growth above criticality in equations (2.42) is saturated by a term which is cubic in the order parameter. In our case, this term emerges by considering the contribution proportional to P_{-k} in equation (2.40). In the polar case ($k = 1$), this contribution involves $mP_{-1}P_2$. This leads to a term which couples to the nematic tensor, with some coefficient $\tilde{\beta}^{(p)}$:

$$\partial_t p_i = \left(\frac{m\rho}{\rho_c^{(p)}} - 1 \right) p_i - \tilde{\beta}^{(p)} m Q_{ij} p_j + \cdots .$$

In regions (III-p) and (IV), the nematic order can be adiabatically eliminated. As we will see below, the expression for the nematic tensor includes a term $Q_{ij} \sim m p_i p_j$, which indeed gives rise to a cubic term in the polarisation equation:

$$\partial_t \boldsymbol{p} = \left(\frac{m\rho}{\rho_c^{(p)}} - 1 \right) \boldsymbol{p} - \beta^{(p)} m^2 p^2 \boldsymbol{p} + \cdots . \tag{2.44}$$

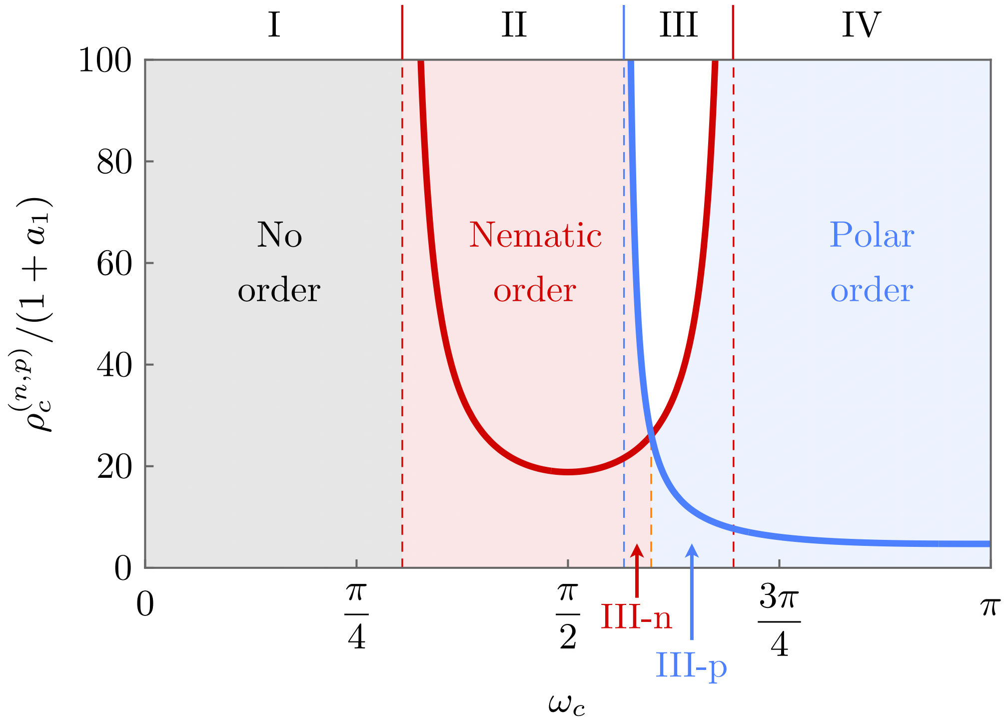

Figure 5: Nematic critical density ($\rho_c^{(n)}$, in red) and polar critical density ($\rho_c^{(p)}$, in blue), normalised by $1+a_1$, as a function of ω_c. Four domains emerge: in (I), no Ginzburg-Landau transition occurs, as $\rho_c^{(n,p)} < 0$. A nematic transition can take place ($\rho_c^{(n)} > 0$) in domains (II) and (III), while a polar transition can take place ($\rho_c^{(n)} > 0$) in domains (III) and (IV). In domains (II) and (IV), the kind of order that is not showing a phase transition can be adiabatically eliminated. In domain (III), on the other hand, both kinds of order are relevant. However, if the densities everywhere in the system are low enough, such that only one order parameter shows exponential growth, adiabatic elimination is still possible: in domain (III-n), for $m\rho < \rho_c^{(p)}$, polar order can be eliminated, while in domain (III-p), for $m\rho < \rho_c^{(n)}$, nematic order can be eliminated.

For nematic order ($k = 2$), on the other hand, the relevant term in (2.40) is proportional to $mP_{-2}P_4$. Adiabatic elimination of the fourth Fourier mode leads to a dependence of the form $P_4 \sim mP_2P_2$, which results in a cubic term:

$$\partial_t Q_{ij} = \left(\frac{m\rho}{\rho_c^{(n)}} - 1 \right) Q_{ij} - \beta^{(n)} m^2 Q_{kl} Q_{kl} Q_{ij} + \cdots . \tag{2.45}$$

The precise form of these terms is indicated in sec. 2.3.

2.2.4 Defining a closure scheme

Besides the terms we have analysed in the previous section, leading to exponential growth or decay, equation (2.40) contains a sum over all other Fourier modes, of which there are infinitely many. To obtain equations of finite length, a closure scheme must be introduced, which should justify the exclusion of higher order modes from the equations. In order to do so, we need a small parameter ϵ in which to expand the equations. This role can be played by the order parameter if we assume that we are close to an ordering transition. Thus, in the following, we specialise on the regions (II), (III-n), (III-p) and (IV), where only one of the two orders exhibits a transition and the other one can be adiabatically eliminated. We assume to be starting from a system with average density $\bar{\rho}$ slightly larger than the critical value ρ_c (remember that $\bar{m} \equiv 1$), and define $\epsilon^2 := \bar{\rho} - \rho_c$.

The closure we derive here hinges on the smallness of the parameter ϵ, and is thus strictly valid only close to the ordering transition. We do not expect the observations we will make far from criticality to be exact in quantitative terms. Nonetheless, the extrapolation of the equations obtained through the Ginzburg-Landau closure to regimes far from the threshold should give at least a qualitative insight into the collective behaviour of the system. After all, the validity of the derived equations close to the transition already imposes a heavy constraint on their form [17].

Polar dominance

In regions (III-p) and (IV), polar order is the slow variable. The proper scaling for this regime is discussed in [23]. Balancing the Ginzburg-Landau terms in eq. (2.44), we find that the order parameter scales as $p \sim \epsilon$, while the time derivative (i.e. the inverse of the characteristic time scale of the dynamics) scales as $\partial_t \sim \epsilon^2$.

The higher Fourier modes ($|k| > 1$) can all be adiabatically eliminated. Expanding the sum in equation (2.40) and setting $\partial_t P_k = 0$ schematically yields:

$$P_k \sim P_1 P_{k-1} + P_{-1} P_{k+1} + \cdots , \tag{2.46}$$

where the terms left out involve higher and higher Fourier modes. Since $P_{\pm 1} \sim p \sim \epsilon$, the lowest order dependence here is $P_{\pm|k|} \sim p P_{\pm(|k|-1)}$. Iterating this relation, we find $P_k \sim \epsilon^{|k|}$. In particular, $Q_{ij} \sim P_{\pm 2} \sim \epsilon^2$.

Once we restore spatial dependence (see next section), translational diffusion will give rise to a term of the form $\nabla^2 \boldsymbol{p}$ in equation (2.44), which gives $\partial_i \sim \epsilon$ for the scaling of the spatial derivative (in other words, the characteristic length scale is of order ϵ^{-1}). In the $\partial_t \rho$ equation, on the other hand, diffusion will give rise to terms $\nabla^2 \rho$ and $\partial_i \partial_j Q_{ij}$. Balancing these two terms implies that typical deviations of the density from its average value scale as $\rho - \bar{\rho} \sim \epsilon^2$.

Thus, overall, we keep terms up to $\mathcal{O}(\epsilon^4)$ in the $\partial_t \rho$ equation, and up to $O(\epsilon^3)$ in the $\partial_t \boldsymbol{p}$ equation. All other terms will have a negligible effect on the dynamics close to criticality, as they are of higher order in ϵ.

Nematic dominance

In regions (II) and (III-n), nematic order is the slow variable. The scaling is then the same as for the active nematics class discussed in [17]. Balancing terms in eq. (2.45) implies a scaling of the order parameter as $Q_{ij} \sim \epsilon$, while the time derivative scales as $\partial_t \sim \epsilon^2$. Just as for the polar regime, translational diffusion will give rise to a term of the form $\nabla^2 Q_{ij}$ in equation (2.45), which gives $\partial_i \sim \epsilon$ for the scaling of the spatial derivative. Balancing $\nabla^2 \rho$ and $\partial_i \partial_j Q_{ij}$ in the $\partial_t \rho$ equation then yields $\rho - \bar{\rho} \sim \epsilon$.

Polar order, on the other hand, can be adiabatically eliminated in this regime. For $\eta > 0$ or $\xi > 0$, as will become apparent below once we take into account spatial dependence, the elimination will lead to a dependence of the form $p_i \sim \partial_i \rho + \partial_i Q_{ij}$, which implies $p_i \sim \epsilon^2$.

The higher Fourier modes ($|k| > 2$) can all be adiabatically eliminated as well. Setting equation (2.40) to zero, and using $P_{\pm 1} \sim \epsilon^2$ and $P_{\pm 2} \sim \epsilon$, we find the scaling

$$P_{\pm|k|} \sim \epsilon P_{\pm(|k|-2)} + \epsilon^2 P_{\pm(|k|-1)} + \cdots . \tag{2.47}$$

For even k, the second term is of higher order, and iterating the relation starting from $k = 2$ gives $P_k \sim \epsilon^{|k/2|}$. For odd k, the two terms are of the same order and we obtain $P_k \sim \epsilon^{|2+(|k|-1)/2|}$.

Overall, we keep terms up to $\mathcal{O}(\epsilon^3)$ in both the $\partial_t \rho$ equation and the $\partial_t Q_{ij}$ equation.

2.2.5 Diffusion and excluded volume terms

In this section, we reintroduce the spatial dependence in the PDF $P(\boldsymbol{r}, \phi)$ and derive the contributions of the diffusion and steric interaction terms (2.26) and (2.28) to the density and order parameter equations. We will need the relation:

$$\begin{aligned} 4 n_i n_j \partial_i \partial_j &= 2[1 + \cos(2\phi)]\partial_x^2 + 2[1 - \cos(2\phi)]\partial_y^2 + 4\sin(2\phi)\partial_x \partial_y \\ &= 2\nabla^2 + e^{2i\phi}\nabla_-^2 + e^{-2i\phi}\nabla_+^2, \end{aligned} \tag{2.48}$$

where we have introduced the complex (Wirtinger) derivatives:

$$\nabla_\pm := \partial_x \pm i\partial_y .$$

Note that $\nabla_+ = \nabla_-^*$ and $\nabla^2 = \nabla_- \nabla_+$.

Diffusion contributions

Plugging the Fourier transform (2.33) into the diffusion term (2.26), we obtain:

$$\begin{aligned} I_{\text{diff}} &= \sum_k [(D_\parallel - D_\perp) n_i n_j \partial_i \partial_j P_k + D_\perp \nabla^2 P_k - D_r k^2 P_k] e^{ik\phi} \\ &= \sum_k \left[\frac{D_\parallel - D_\perp}{4} (e^{2i\phi}\nabla_-^2 + e^{-2i\phi}\nabla_+^2) P_k + \frac{D_\parallel + D_\perp}{2} \nabla^2 P_k - D_r k^2 P_k \right] e^{ik\phi}, \end{aligned}$$

where in the second line we have used (2.48). Extracting the coefficient of $e^{ik\phi}$, the contribution of this term to $\partial_t P_k(\boldsymbol{r})$ reads:

$$\partial_t P_k = \frac{D_\parallel - D_\perp}{4} (\nabla_-^2 P_{k-2} + \nabla_+^2 P_{k+2}) + \frac{D_\parallel + D_\perp}{2} \nabla^2 P_k - D_r k^2 P_k + \cdots . \tag{2.49}$$

While the two last terms yield trivial contributions, the first term requires some manipulation.

For $k = 0$, we rewrite it using the relation:

$$\begin{aligned}
\pi(\nabla_-^2 P_{-2} + \nabla_+^2 P_2) &= 2\pi\,\mathrm{Re}(\nabla_-^2 P_{-2}) \\
&= 2\pi[(\partial_x^2 - \partial_y^2)\,\mathrm{Re}\,P_{-2} + 2\partial_x\partial_y\,\mathrm{Im}\,P_{-2}] \\
&= [(\partial_x^2 - \partial_y^2)Q_{xx} + 2\partial_x\partial_y Q_{xy}] \\
&= \partial_i\partial_j Q_{ij}. \qquad (2.50)
\end{aligned}$$

For $k = -1$, the $\nabla_-^2 P_{-3}$ term is of higher order in the closure scheme, while the other term gives:

$$\begin{aligned}
\begin{pmatrix} \mathrm{Re}\,\nabla_+^2 P_1 \\ \mathrm{Im}\,\nabla_+^2 P_1 \end{pmatrix} &= \begin{pmatrix} (\partial_x^2 - \partial_y^2)\,\mathrm{Re}\,P_1 - 2\partial_x\partial_y\,\mathrm{Im}\,P_1 \\ 2\partial_x\partial_y\,\mathrm{Re}\,P_1 + (\partial_x^2 - \partial_y^2)\,\mathrm{Im}\,P_1 \end{pmatrix} \\
&= 2\pi \begin{pmatrix} (\partial_x^2 - \partial_y^2)p_x + 2\partial_x\partial_y p_y \\ 2\partial_y\partial_x p_x - (\partial_x^2 - \partial_y^2)p_y \end{pmatrix} \\
&= 2\pi[2\boldsymbol{\nabla}(\boldsymbol{\nabla}\cdot\boldsymbol{p}) - \nabla^2\boldsymbol{p}]. \qquad (2.51)
\end{aligned}$$

Finally, for $k = -2$, the $\nabla_-^2 P_{-4}$ term is of higher order in the closure scheme, while the other term yields:

$$\begin{pmatrix} \mathrm{Re}\,\nabla_+^2 P_0 \\ \mathrm{Im}\,\nabla_+^2 P_0 \end{pmatrix} = \begin{pmatrix} (\partial_x^2 - \partial_y^2)P_0 \\ 2\partial_x\partial_y P_0 \end{pmatrix} = 2\pi\cdot 2(\partial_i\partial_j\rho)^{\mathsf{TS}}, \qquad (2.52)$$

where we have introduced the notation A_{ij}^{TS} for the traceless symmetric part of a 2-tensor:

$$A_{ij}^{\mathsf{TS}} := \frac{1}{2}\left(A_{ij} + A_{ji} - \mathrm{tr}\,A\cdot\delta_{ij}\right). \qquad (2.53)$$

Putting everything together gives:

$$\begin{aligned}
\partial_t\rho &= \frac{D_\parallel + D_\perp}{2}\nabla^2\rho + \frac{D_\parallel - D_\perp}{2}\partial_i\partial_j Q_{ij} + \cdots\,, \\
\partial_t\boldsymbol{p} &= -D_r\boldsymbol{p} + \frac{D_\parallel + 3D_\perp}{4}\nabla^2\boldsymbol{p} + \frac{D_\parallel - D_\perp}{2}\boldsymbol{\nabla}(\boldsymbol{\nabla}\cdot\boldsymbol{p}) + \cdots\,, \\
\partial_t Q_{ij} &= -4D_r Q_{ij} + \frac{D_\parallel + D_\perp}{2}\nabla^2 Q_{ij} + \frac{D_\parallel - D_\perp}{2}(\partial_i\partial_j\rho)^{\mathsf{TS}} + \cdots\,.
\end{aligned}$$

Rescaling time, space and the fields as indicated in (2.37) and using the relations (2.27), the contribution from the diffusion term finally reads:

$$\partial_t\rho = \frac{1}{32}\nabla^2\rho + \frac{1}{96}\partial_i\partial_j Q_{ij} + \cdots\,, \qquad (2.54a)$$

$$\partial_t\boldsymbol{p} = -\boldsymbol{p} + \frac{5}{192}\nabla^2\boldsymbol{p} + \frac{1}{96}\boldsymbol{\nabla}(\boldsymbol{\nabla}\cdot\boldsymbol{p}) + \cdots\,, \qquad (2.54b)$$

$$\partial_t Q_{ij} = -4Q_{ij} + \frac{1}{32}\nabla^2 Q_{ij} + \frac{1}{96}(\partial_i\partial_j\rho)^{\mathsf{TS}} + \cdots\,. \qquad (2.54c)$$

Excluded volume contributions

The excluded volume term (2.28) reads:

$$I_{\text{excl}} = \sum_k [(D_\parallel - D_\perp) n_i n_j \partial_i (P_k \partial_j U) + D_\perp \partial_j (P_k \partial_j U)] e^{ik\phi}$$

Like for diffusion, in the $\partial_t P_k$ equation this will result in a term involving P_k only, as well as another one involving P_{k+2} and P_{k-2}. The former is only relevant for the ρ equation in both regimes, while being of higher order in the GL closure for the order parameter equations. The latter term, on the other hand, leads to higher order contributions in the ρ and $\boldsymbol{p}$ equations for both nematic and polar dominance. It will, however, be relevant for the Q equation in the nematic regime.

Using a generalisation of (2.48), the contribution of the excluded volume term to the $\partial_t \rho$ equation reads:

$$\frac{D_\parallel + D_\perp}{2} \partial_j \left[\rho \partial_j \left(\frac{2}{\pi} L^2 \rho + \frac{1}{4\pi} L^4 \rho^2 \right) \right] = \frac{D_\parallel + D_\perp}{2} \nabla^2 \left(\frac{1}{\pi} L^2 \rho^2 + \frac{1}{6\pi} L^4 \rho^3 \right),$$

where we used $\partial_j \rho^2 = 2\rho \partial_j \rho$, $\partial_j \rho^3 = \frac{3}{2} \rho \partial_j \rho^2$. Applying the rescaling (2.37) results in:

$$\partial_t \rho = \frac{1}{32\pi} \nabla^2 \left(\alpha \rho^2 + \frac{1}{6} \alpha^2 \rho^3 \right) + \cdots$$

The contribution to the $\partial_t P_{-2}$ equation, on the other hand, reads:

$$\frac{D_\parallel - D_\perp}{4} \nabla_+ \left[P_0 \nabla_+ \left(\frac{2}{\pi} L^2 \rho + \frac{1}{4\pi} L^4 \rho^2 \right) \right] = \frac{D_\parallel - D_\perp}{4 \cdot 2\pi} \nabla_+^2 \left(\frac{1}{\pi} L^2 \rho^2 + \frac{1}{6\pi} L^4 \rho^3 \right),$$

which results in a contribution to the Q equation of the form:

$$\partial_t Q_{ij} = \frac{1}{96\pi} \left[\partial_i \partial_j \left(\alpha \rho^2 + \frac{1}{6} \alpha^2 \rho^3 \right) \right]^{\mathsf{TS}} + \cdots$$

2.2.6 Performing the collision integrals

The only part of the kinetic equation (2.25) we are left to evaluate are the collision integrals (2.31). In order to perform them in the general case, keeping spatial dependence, we must extract the dependence on $\boldsymbol{s}$ out of the PDF. Since we are interested in a coarse-grained description of the system, the continuum fields we obtain in the end should vary on a length scale which is much larger than the microscopic length scale, which here is the microtubule length L. Hence, for a vector $\boldsymbol{v}$ with $|v| \sim L$, we can perform a Taylor expansion of the PDF in its spatial argument [23]:

$$P(\boldsymbol{r} + \boldsymbol{v}; \phi) = P(\boldsymbol{r}; \phi) + \boldsymbol{v} \cdot \boldsymbol{\nabla} P(\boldsymbol{r}; \phi) + \frac{1}{2} (\boldsymbol{v} \cdot \boldsymbol{\nabla})^2 P(\boldsymbol{r}; \phi) + \mathcal{O}((\boldsymbol{v} \cdot \boldsymbol{\nabla})^3 P). \qquad (2.55)$$

We stop this gradient expansion at the second order (which corresponds to the diffusion and excluded volume terms).

Plugging the gradient expansion (2.55) into the integrals (2.31), we notice that the gradients (in $\boldsymbol{r}$) can be taken out of the integrals over $\boldsymbol{s}$; by doing so, the only integrals over $\boldsymbol{s}$ we need to perform are of the type:

$$I_s^W(j,k) := \int\limits_{W(\phi,\omega)} \mathrm{d}^2 s \; s_\parallel^j s_\perp^k. \tag{2.56}$$

To handle these integrals, we apply a change of coordinates that maps the rhombus from Fig. 3 onto a square. To this goal, we choose new coordinates $u_{1,2}$ parallel to the sides of the rhombus, centred at its origin. The inverse coordinate transformation is given by:

$$\begin{pmatrix} s_\perp \\ s_\parallel \end{pmatrix} = L \begin{pmatrix} \sin\left(\frac{\omega}{2}\right) & -\sin\left(\frac{\omega}{2}\right) \\ \cos\left(\frac{\omega}{2}\right) & \cos\left(\frac{\omega}{2}\right) \end{pmatrix} \begin{pmatrix} u_1 \\ u_2 \end{pmatrix}. \tag{2.57}$$

The matrix appearing here is the Jacobian $\frac{\partial \boldsymbol{s}}{\partial \boldsymbol{u}}$, and we have included a factor L to make the new coordinates dimensionless. Note that the new coordinate system is not orthogonal, since the basis vector are at an angle ω with respect to each other; indeed, the Jacobi determinant reads $\det \frac{\partial \boldsymbol{s}}{\partial \boldsymbol{u}} = 2L^2 \sin\left(\frac{\omega}{2}\right)\cos\left(\frac{\omega}{2}\right) = L^2 \sin\omega$.

Using this coordinate transformation, the different rhombi R_0, R_+ and R_- defined in Fig. 3 are distinguished only by the integral bounds. Hence, the integral from eq. (2.56) reads:

$$\begin{aligned} I_s^W(j,k) &= \int\limits_{W(\phi,\omega)} \mathrm{d}^2 s \; s_\parallel^j s_\perp^k = \int\limits_{W(\phi,\omega)} \mathrm{d}^2 u \, |\sin\omega| \cos^j\left(\frac{\omega}{2}\right) \sin^k\left(\frac{\omega}{2}\right) (u_1+u_2)^j (u_1-u_2)^k \\ &= L^{2+j+k} Gm \, |\sin\omega| \cos^j\left(\frac{\omega}{2}\right) \sin^k\left(\frac{\omega}{2}\right) \cdot \\ &\quad \cdot \left((1+\Xi) \int_{-1/2}^{1/2} \mathrm{d}^2 u + \Xi \int_{1/2-\tau_0}^{1/2} \mathrm{d}^2 u - \Xi \int_{-1/2}^{1/2-\tau_0} \mathrm{d}^2 u \right) (u_1+u_2)^j (u_1-u_2)^k. \end{aligned}$$

By doing so, we have removed the dependence on ω from the integral. The last line will give prefactors depending only on Ξ and τ_0, which result from the integration of simple polynomials over square domains. Since we consider the gradient expansion above only to second order, we only need to calculate the integrals with $j+k \leq 2$, whose values are listed in the table below:

$\frac{I_s^W(j,k)}{GmL^{2+j+k}}$	$j=0$	$j=1$	$j=2$
$k=0$	$(1+a_1)\lvert\sin\omega\rvert$	$\frac{1}{4}a_2\lvert\sin\omega\rvert\sin\left(\frac{\omega}{2}\right)$	$\frac{1}{12}(1+a_3)(1-\cos\omega)\lvert\sin\omega\rvert$
$k=1$	0	0	
$k=2$	$\frac{1}{12}(1+a_3)(1+\cos\omega)\lvert\sin\omega\rvert$		

Note that $I_s^W(0,0)$ corresponds to the weighted area of the rhombi, which we had calculated already in eq. (2.35). We have introduced the abbreviations:

$$a_1 = 2\Xi\tau_0, \tag{2.58a}$$

$$a_2 = 4\Xi\tau_0[1-\tau_0], \tag{2.58b}$$

$$a_3 = 4\Xi\tau_0\left[1-\frac{3}{2}\tau_0+\tau_0^2\right]. \tag{2.58c}$$

In the strong tip accumulation limit discussed in eq. (2.20), these reduce to $a_1 = \xi$ and $a_2 = a_3 = 2\xi$.

After performing the spatial integrals, one needs to take the integrals over ω as well, and project the kinetic equation onto the various Fourier components to obtain the continuum equations. A glimpse into how the procedure works can be found in appendix A.2, where we extract the contributions to the $\partial_t \boldsymbol{p}$ equation that are quadratic in $\boldsymbol{p}$ and linear in η, as an example. As can be seen already from the derivation of those terms, the calculation is very lengthy. To obtain the full equations, which we present below, we therefore made use of Mathematica.

2.3 Mesoscopic continuum equations

After having performed all necessary integrals and collected the terms belonging to the dynamic equations of the various Fourier modes, we apply the closure scheme defined in sec. 2.2.4 to obtain the sought continuum equations. Since the closure scheme differs for nematic and polar dominance, the resulting set of equations is going to be different for these two cases.

We reintroduce the inhomogeneity of the free motor concentration m by promoting it from a constant to a spatial field. This entails a choice to be made on where to position this field with respect to the spatial gradients that appear in our equations. The difference between the possible choices will be given by terms of order $\boldsymbol{\nabla} m = \mathcal{O}(\gamma)$, so it does not matter in the small γ limit. Therefore, for simplicity, we will keep the m field outside of all gradients, except in the density equation, where the inclusion of m inside the gradients is necessary to ensure mass conservation. This is also what would result if we kept the spatial dependence of m throughout the derivation, evaluating the field at the midpoint of the centres of mass in the collision integrals (see [13]).

Furthermore, in order to improve the validity of the equations far from the critical threshold [17], we keep the full ρ dependence in the isotropic term of the ρ equation, i.e. we do not linearise the ρ^2 and ρ^3 terms resulting from collisions and steric interactions in the ρ equation, following [23].

2.3.1 Nematic dominance

In the case of nematic dominance, i.e. in regimes (II) and (III-n), using the nematic closure scheme from sec. 2.2.4, we obtain the equations below:

$$\partial_t \rho = \nabla^2\left(D_\rho \rho + m\nu\rho^2 + \alpha_2\rho^2 + \alpha_3\rho^3\right) + \partial_i\partial_j[(D_Q + m\tilde{\chi}_Q)Q_{ij}], \tag{2.59a}$$

$$\partial_t p_i = (m\rho/\rho_c^{(p)} - 1)p_i + m\tilde{\zeta}_1\partial_i\rho + m\lambda_Q\partial_j Q_{ij}, \tag{2.59b}$$

$$\begin{aligned}\partial_t Q_{ij} = {}& 4(m\rho/\rho_c^{(n)} - 1)Q_{ij} - m^2\beta^{(n)}Q_{kl}Q_{kl}Q_{ij} + (\tilde{\kappa}_Q + m\tilde{\kappa}'_Q)\nabla^2 Q_{ij} \\ & - (\tilde{\zeta}_Q + m\tilde{\zeta}'_Q)(\partial_i\partial_j\rho)^{\mathsf{TS}} + 2m\zeta_P(\partial_i p_j)^{\mathsf{TS}}.\end{aligned} \tag{2.59c}$$

The coefficients in these equations are all functions of the microscopic parameters, which we list in appendix A.3.

Since $\rho_c^{(p)} < 0$, the polarisation experiences exponential decay at a rate which is much faster than the time scales of the slow variables. Thus, it can be adiabatically eliminated by setting $\partial_t p_i = 0$. We find:

$$p_i = B_P\left(m\tilde{\zeta}_1\partial_i\rho + m\lambda_Q\partial_j Q_{ij}\right), \tag{2.60}$$

with $B_P = \left(1 - \bar{\rho}/\rho_c^{(p)}\right)^{-1}$. Polarisation thus emerges wherever there are gradients in the density or the nematic order.

We obtain the final equations by plugging in this relation into equations (2.59a) and (2.59c). It is convenient to define the following expressions:

$$\begin{aligned}\chi_Q &= D_Q + m\tilde{\chi}_Q, \\ \kappa_Q &= \tilde{\kappa}_Q + m\tilde{\kappa}'_Q + m^2 B_P\zeta_P\lambda_Q, \\ \zeta_Q &= \tilde{\zeta}_Q + m\tilde{\zeta}'_Q + 2m^2 B_P\zeta_P\tilde{\zeta}_1.\end{aligned}$$

In the dynamic equation for the free motor concentration (2.21), the diffusion term is one order lower in the Ginzburg-Landau closure compared to the advection term. Hence, for consistency, we will ignore free motor inhomogeneity in the nematic regime and set $m \equiv 1$. We obtain:

$$\boxed{\begin{aligned}\partial_t \rho &= \nabla^2\left(D_\rho\rho + (\nu + \alpha_2)\rho^2 + \alpha_3\rho^3\right) + \partial_i\partial_j(\chi_Q Q_{ij}), && (2.61\text{a}) \\ \partial_t Q_{ij} &= 4(\rho/\rho_c^{(n)} - 1)Q_{ij} - \beta^{(n)}Q_{kl}Q_{kl}Q_{ij} \\ &\quad + \kappa_Q\nabla^2 Q_{ij} - \zeta_Q(\partial_i\partial_j\rho)^{\mathsf{TS}}. && (2.61\text{b})\end{aligned}}$$

Similar equations were proposed phenomenologically in [28], up to rescalings and a different form of the ζ_Q term, which there reads $+\zeta_Q(\partial_i\rho\partial_j\rho)^{\mathsf{TS}}$. That choice would not be consistent with our derivation, since that term is of higher order in the Ginzburg-Landau closure compared to $(\partial_i\partial_j\rho)^{\mathsf{TS}}$.

The nematic equations show interesting phenomenology, such as a transition from contractile to extensile behaviour controlled by the sliding strength, that follows from a sign change in χ_Q, as well as novel instabilities. However, the detailed study of these equations is outside the scope of the present work and must be deferred to future investigations.

2.3.2 Polar dominance

For polar dominance, i.e. in regimes (III-p) and (IV) of Fig. 5, using the closure defined in sec. 2.2.4, we obtain the following equations:

$$\begin{aligned}
\partial_t \rho &= \nabla^2\big(D_\rho \rho + m\nu\rho^2 + \alpha_2\rho^2 + \alpha_3\rho^3\big) + \partial_i\partial_j[(D_Q + m\tilde{\chi}_Q)Q_{ij}] \\
&\quad + \tilde{\chi}_1\partial_i\partial_j(mp_ip_j) + \tilde{\chi}_2\nabla^2\big(mp^2\big), && (2.62\text{a})\\
\partial_t p_i &= (m\rho/\rho_c^{(p)} - 1)p_i + (\tilde{\kappa}_1 + m\tilde{\kappa}_1')\nabla^2 p_i + (\tilde{\kappa}_2 + m\tilde{\kappa}_2')\partial_i(\boldsymbol{\nabla}\cdot\boldsymbol{p}) - m\tilde{\beta}^{(p)}Q_{ij}p_j \\
&\quad + m\lambda_Q\partial_j Q_{ij} + m\tilde{\zeta}_1\partial_i\rho + m\tilde{\zeta}_2\partial_i p^2 - m\tilde{\lambda}_1 p_j\partial_j p_i - m\tilde{\lambda}_2 p_i\partial_j p_j, && (2.62\text{b})\\
\partial_t Q_{ij} &= 4(m\rho/\rho_c^{(n)} - 1)Q_{ij} + 2mg_P(p_ip_j)^{\mathsf{TS}} + 2m\zeta_P(\partial_i p_j)^{\mathsf{TS}}. && (2.62\text{c})
\end{aligned}$$

The coefficients are functions of the microscopic parameters, which we list in appendix A.3. The nematic tensor can be adiabatically eliminated:

$$Q_{ij} = 2B_Q\left(mg_P(p_ip_j)^{\mathsf{TS}} + m\zeta_P(\partial_i p_j)^{\mathsf{TS}}\right), \tag{2.63}$$

with $B_Q = \left(4 - 4\bar{\rho}/\rho_c^{(n)}\right)^{-1}$. The first term here is the nematic order emerging as a consequence of the polar order (with $\boldsymbol{p}$ as a nematic director), while the second term gives rise to nematic order along polarisation gradients.

Plugging in the adiabatically eliminated nematic tensor into equations (2.62) leads to a number of contributions. For brevity, we define the following quantities, which are functions of the microscopic parameters as well as the local motor density m:

$$\begin{aligned}
\chi_1 &= m\tilde{\chi}_1 + 2(mD_Q + m^2\tilde{\chi}_Q)B_Q g_P,\\
\chi_2 &= m\tilde{\chi}_2 - (mD_Q + m^2\tilde{\chi}_Q)B_Q g_P,\\
\beta^{(p)} &= \tilde{\beta}^{(p)}B_Q g_P,\\
\kappa_1 &= \tilde{\kappa}_1 + m\tilde{\kappa}_1' + m^2 B_Q\lambda_Q\zeta_P,\\
\kappa_2 &= \tilde{\kappa}_2 + m\tilde{\kappa}_2',\\
\zeta_1 &= m\tilde{\zeta}_1,\\
\zeta_2 &= m\tilde{\zeta}_2 - m^2 B_Q(\lambda_Q g_P + \zeta_P\tilde{\beta}^{(p)}/2),\\
\lambda_1 &= m\tilde{\lambda}_1 - m^2 B_Q(2\lambda_Q g_P - \zeta_P\tilde{\beta}^{(p)}),\\
\lambda_2 &= m\tilde{\lambda}_2 - m^2 B_Q(2\lambda_Q g_P + \zeta_P\tilde{\beta}^{(p)}).
\end{aligned}$$

With these abbreviations, and taking into account the equation for the free motor concentration, the hydrodynamic equations for the polar regime read:

$$\begin{aligned}
\partial_t \rho &= \nabla^2\big(D_\rho\rho + m\nu\rho^2 + \alpha_2\rho^2 + \alpha_3\rho^3\big) + \partial_i\partial_j(\chi_1 p_ip_j) + \nabla^2\big(\chi_2 p^2\big), && (2.64\text{a})\\
\partial_t \boldsymbol{p} &= \left[(m\rho/\rho_c^{(p)} - 1) - m^2\beta^{(p)}p^2\right]\boldsymbol{p} + \kappa_1\nabla^2\boldsymbol{p} + \kappa_2\boldsymbol{\nabla}(\boldsymbol{\nabla}\cdot\boldsymbol{p}) \\
&\quad + \zeta_1\boldsymbol{\nabla}\rho + \zeta_2\boldsymbol{\nabla}p^2 - \lambda_1(\boldsymbol{p}\cdot\boldsymbol{\nabla})\boldsymbol{p} - \lambda_2(\boldsymbol{\nabla}\cdot\boldsymbol{p})\boldsymbol{p}, && (2.64\text{b})\\
\partial_t m &= D_m\nabla^2 m - v_m\boldsymbol{\nabla}(m\boldsymbol{p}). && (2.64\text{c})
\end{aligned}$$

These equations have not been studied phenomenologically. If we set m to be constant, the polarisation equation has the same form as in the Toner-Tu model for self-propelled particles [29]. There, however, the polarisation vector is interpreted as the velocity of the particles, and the density equation takes the form of an advective continuity equation $\partial_t \rho + \boldsymbol{\nabla}(\boldsymbol{p}\rho) = 0$.

In the rest of this thesis, we will focus on the polar regime, and on the system of equations (2.64). For brevity, we will write $\beta = \beta^{(p)}$ and $\rho_c = \rho_c^{(p)}$.

Chapter 3

Micelles and Foams

Now that we have obtained a hydrodynamic description for our system in the polar regime, we can inspect the equations (2.64) analytically as well as numerically, in order to understand the collective behaviour that they give rise to.

In section 3.1, we perform numerical simulations of the continuum model and determine its phase diagram, exhibiting stable micelles, micelles that are unstable with respect to bilayer formation, as well as active foam-like networks of bilayers. We discuss the effect that the various microscopic parameters we've introduced (i.e. the critical angle ω_c, the sliding strength η, the anisotropy parameter ξ and the motor Péclet number γ, as well as the microtubule and motor densities) have on the phase structure of the system.

In section 3.2, we discuss the hydrodynamic equations we have derived from a mathematical standpoint, explaining the role of the various terms in the density and polarisation equations. The goal is to obtain intuition about the interplay between density, order strength and order orientation. In section 3.3, we introduce a phenomenological generalisation of the continuum model that allows for free variation of the equations' coefficients, which will be useful to verify the analytical predictions we make.

In section 3.4, we derive the stationary profiles of the bilayers and the micelles, and discuss the role the terms in the equation have in selecting the length scales of these solutions. We check the validity of our results by comparing them with measurements made in numerical simulations of the phenomenological model.

In section 3.5, we examine the instabilities of the homogenous states with respect to density and order perturbations, and discuss the feedback mechanisms among the different terms in the equations that give rise to these instabilities. In section 3.6, we show that these mechanisms are also relevant for the stability of radially symmetric solutions. In particular, we discuss two distinct instabilities that arise for micelles, which we call fingering instability and branching instability. These instabilities help us explain the phase diagram observed in numerical simulations.

3.1 Phase diagram of the derived model

To inspect the phase diagram of the system in the polar regime, we numerically simulated the equations (2.64) using the finite difference PDE solver provided by COMSOL Multiphysics. In all simulations, we chose a square geometry with periodic boundary conditions. We initiated the system in the isotropic state ($\boldsymbol{p} = 0$) with constant $\rho = \bar{\rho}$ and $m = 1$, adding a random perturbation to the fields at every mesh point. We kept the motor diffusion constant fixed at $D_m = 0.2$. Unless otherwise stated, the snapshots in this chapter were taken at $t = 500$.

3.1.1 The micelle-foam transition

For sufficiently low critical angles ω_c, i.e. a sufficiently strong admixture of antipolar interactions, we observe a transition between different inhomogeneous states as we increase the initial density $\bar{\rho}$ (see Fig. 6).

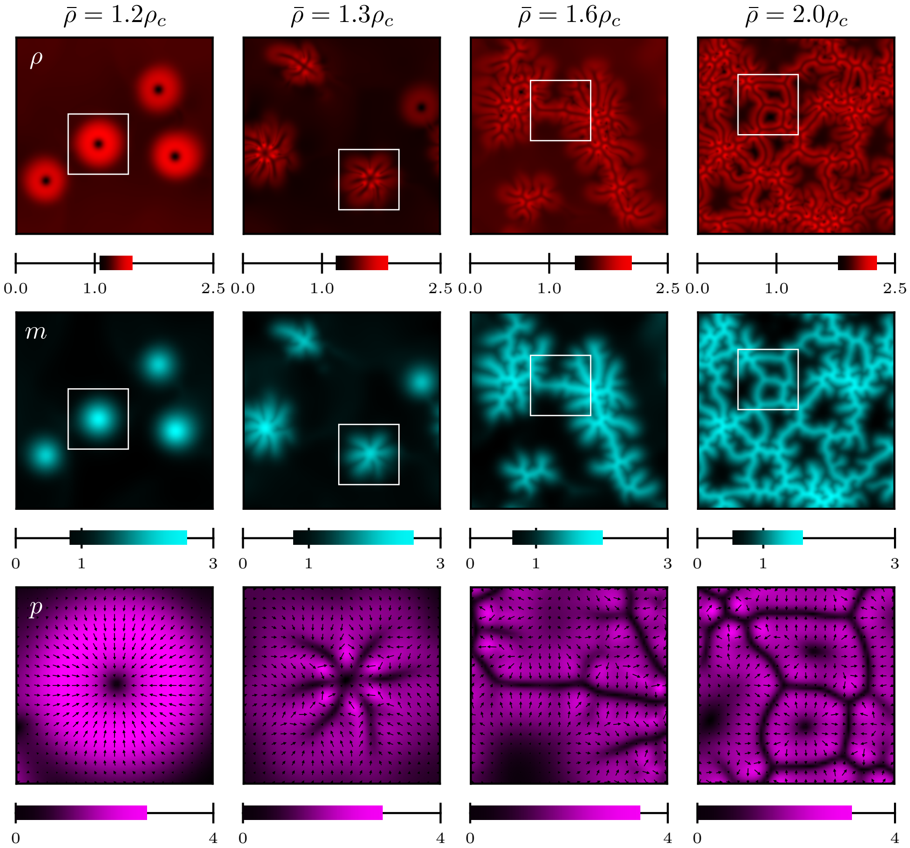

Figure 6: Snapshots of numerical simulations for $\omega_c = 2.18$, $\eta = 0.58$, $\alpha = 0.7$, $\xi = 0$, $\gamma = 0.02$ in a periodic box of size 60×60, for different initial densities $\bar{\rho}$. From top to bottom, the microtubule density field ρ, the motor density field m and the polarisation $\boldsymbol{p}$ are shown. The bottom plots zoom in on an area of size 18×18, showing a micelle, a branching micelle, a bilayer and two active foam cells in detail. The colorbars indicate the minimum and the maximum in the snapshot. Microtubule density values are indicated in units of ρ_c, motor density values in units of $\bar{m} \equiv 1$.

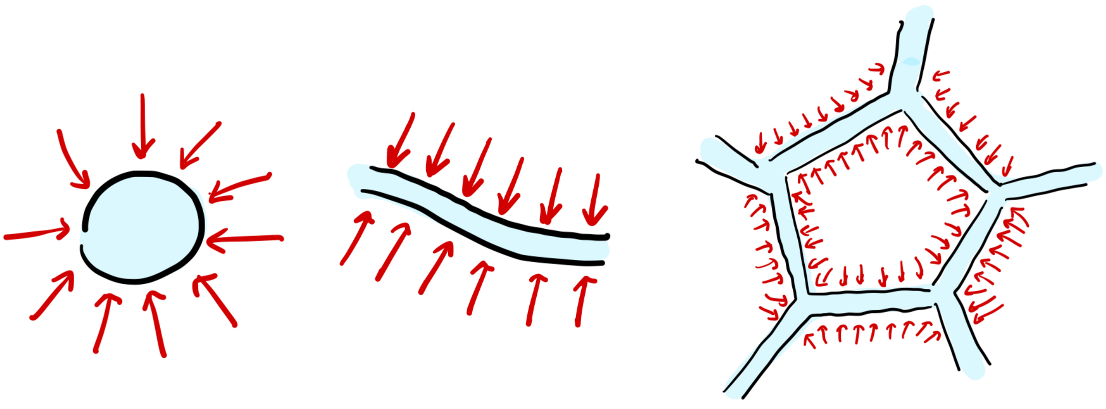

Aster/Micelle Bilayer Active foam cell

Figure 7: Cartoon representation of micelles, bilayers and active foam cells. The arrows indicate the direction of the polarisation field; the motors are advected along this field and accumulate in the blue regions. In this sense, the inside of the micelle corresponds to the inside of the bilayer. In the active foam phase, the bilayers connect to form a network, and the motors accumulate in its edges. With respect to the centre of a unit cell, the polarisation is therefore pointing outwards.

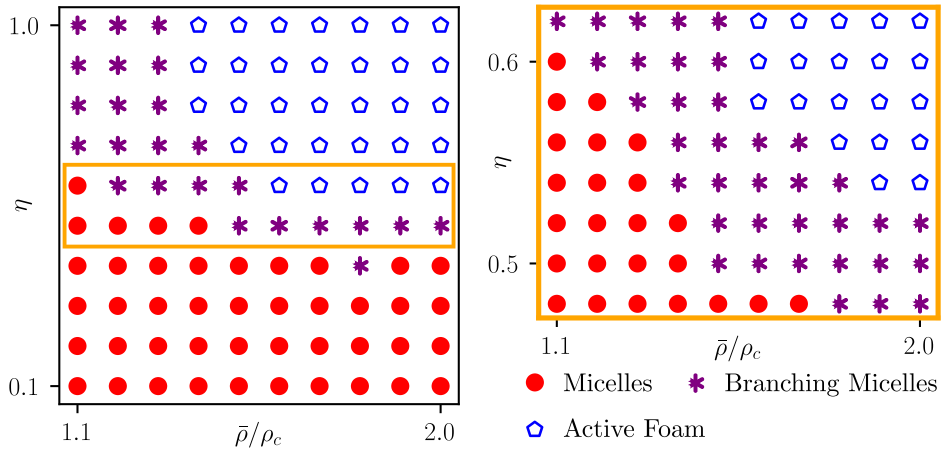

Figure 8: Phase diagram for fixed $\omega_c = 2.18$, $\alpha = 0.7$, $\xi = 0$, $\gamma = 0.02$. System size 60×60, run time $t = 500$. In the Micelle phase, a population of radially symmetric micelles is left at the end of the simulation (compare first column in Fig. 6). In the Branching Micelle phase, at least one micelle is unstable to branching, so that bilayers form (second and third columns in Fig. 6). In the Active Foam phase, the bilayers connect with each other to form at least one loop, i.e. a unit cell of the foam (fourth column in Fig. 6). For intermediate values of η (orange box shown in the detail on the right), a micelle-foam transition can be observed as the initial density $\bar{\rho}$ is varied.

At low densities, radially symmetric aster-like structures take shape (first column of Fig. 6). At the centre of these structures a defect is found, where the polarisation vanishes and the microtubule density has a minimum. Around this defect, a ring of elevated microtubule density forms, in which the polarisation field points inward. In contrast, the motor density shows a peak in the middle of the aster. In the following, we refer to these structures as *micelles*, in analogy to lipid monolayer rings [30]. This terminology takes into account that the microtubule-depleted zone in the centre can be quite large, in contrast to what is normally referred to as an aster (e.g. in [13]).

At higher microtubule densities (second column of Fig. 6), while micelles form at first, they become unstable and lose their continuous rotational symmetry. The high-density ring breaks apart, and several branches form that extend radially outward. Along the branches, the polarisation field is rotated to point in the direction perpendicular to the branch on both sides, in a bilayer-like fashion. At even higher densities, the branches from different unstable micelles connect to form longer bilayers (third column of Fig. 6). The motor field accumulates in the inside of these bilayers.

Finally, as the density is increased even more (fourth column of Fig. 6), the bilayers form a foam-like network, which can extend throughout the simulated system. As time progresses, the network undergoes constant reconfiguration, as new bilayers branch out of its edges and connect to other parts of the network. This leads to the formation of new vertices and new cells. We call this the *active foam* phase. A cell of the active foam has a centre depleted of both microtubules and motors, with the polarisation pointing outward. Figure 7 illustrates the orientation of the polarisation in the different phases.

In Figure 8, we show the phase diagram for different initial densities $\bar{\rho}$ and sliding strengths η. We distinguish the phases as follows: In the micelle phase, a population of stable micelles is formed. If at least one micelle exhibits branching, we assign the parameter set to the branching micelles phase. Finally, we define active foams as networks of bilayers with at least one closed loop. With this definitions, we see that a transition from stable micelles to branching micelles and finally to active foam networks is possible by increasing the initial density $\bar{\rho}$ at fixed intermediate sliding strengths η. Importantly, while the critical angle and the sliding strength are determined by the microscopic properties of the microtubules and motors used, the microtubule density is a control parameter that can be varied locally within the same system: hence, we expect that for large enough systems, micelles and foams can coexist, depending on the local microtubule density.

3.1.2 The role of antipolar sliding and anisotropy

The phase diagram in Fig. 8 shows that the formation of active foams is only possible at high enough values of the sliding parameter η. Indeed, at lower values of the parameter one always finds non-branching micelles. Changing the sliding parameter within the micelle phase affects the inner length scale of the micelles: for weaker sliding strengths, the depleted region in the centre of the micelle is larger (see Fig. 9). Within the active foam phase, on the other hand, changing the sliding parameter affects how much the edges of the network branch out: for higher values of η, the bilayers branch out so much that the network fills out a large portion of the space. The shape of the unit cell deviates more and more from a simple polygon, so that we can hardly speak of foams anymore (see Fig. 10).

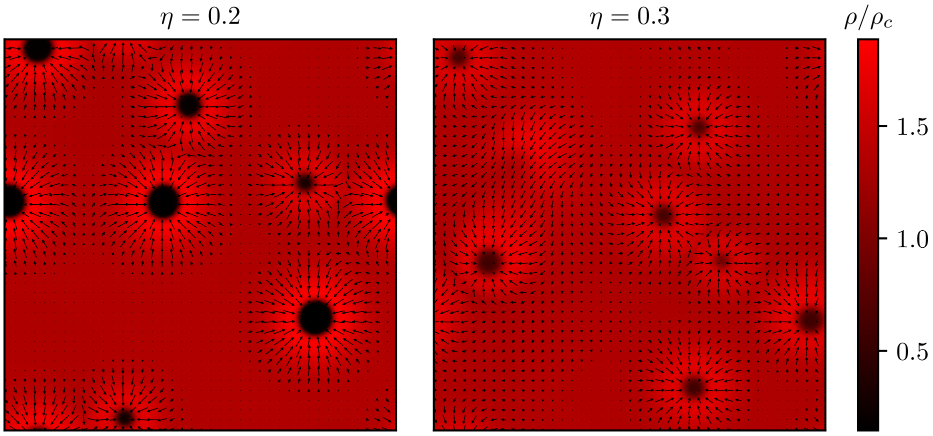

Figure 9: Snapshots of the ρ field for fixed $\omega_c = 2.18$, $\bar{\rho} = 1.4\rho_c$, $\alpha = 0.7$, $\xi = 0$, $\gamma = 0.02$. System size 60×60. As the sliding strength is lowered, the micelles open up, exhibiting a larger depleted centre.

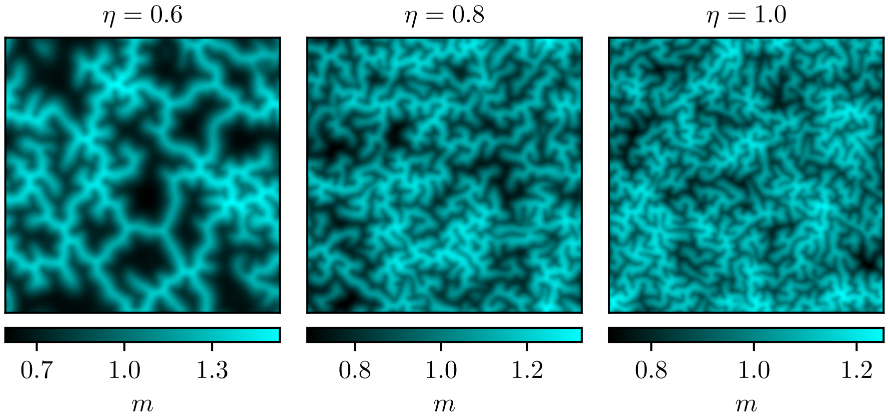

Figure 10: Snapshots of the m field for fixed $\omega_c = 2.18$, $\bar{\rho} = 1.8\rho_c$, $\alpha = 0.7$, $\xi = 0$, $\gamma = 0.02$. System size 60×60. As the sliding strength is increased, the edges of the active foam branch out more and more, making it difficult to identify unit cells.

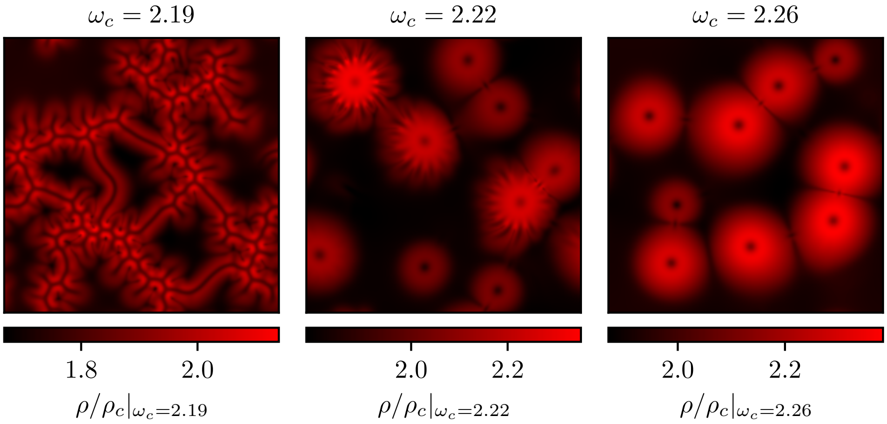

Figure 11: Snapshots of the ρ field for fixed $\eta = 0.6$, $\alpha = 0.7$, $\xi = 0$, $\gamma = 0.02$. System size 60×60. The initial density was kept fixed at $\bar{\rho} = 1.8\rho_c|_{\omega_c=2.18}$, so that the distance from criticality becomes larger as ω_c is increased. In spite of this, the simulations show that foams take shape only for low ω_c, and give way to branching micelles and stable micelles as the critical angle is increased. This illustrates that antipolar interactions are essential for the formation of active foams.

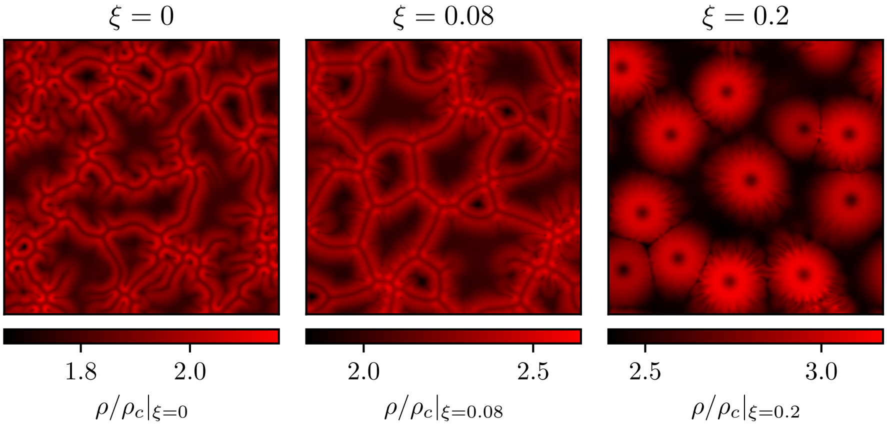

Figure 12: Snapshots of the ρ field for fixed $\omega_c = 2.18$, $\eta = 0.58$, $\alpha = 0.7$, $\gamma = 0.02$. System size 60×60. The initial density was kept fixed at $\bar{\rho} = 1.9\rho_c|_{\xi=0}$, so that the distance from criticality becomes larger as ξ is increased. Nevertheless, the foams give way to branching micelles for larger values of the anisotropy parameter, so that we conclude that a low value of ξ is needed for foam formation.

Hence, overall, well-shaped foams are only found at intermediate values of η.

To verify the role of antipolar interaction in the formation of foams, we vary the critical angle ω_c. Increasing this angle reduces the admixture of antipolar interactions, while increasing the range where polar alignment takes place. As ω_c is increased, we find that active foams are relegated to higher and higher values of η and $\bar{\rho}$. Indeed, increasing the critical angle at fixed η and $\bar{\rho}$, we see how active foams give way to branching micelles, and eventually to stable micelles (see Fig. 11). Note that since the critical density ρ_c decreases at higher ω_c (see Fig. 5), keeping $\bar{\rho}$ constant means that we are increasing the distance from criticality. Even so, active foams disappear from the phase diagram. We conclude that antipolar interactions are needed for the emergence of this phase. Since foams do not appear at low values of η, it seems that *antipolar sliding* is the essential ingredient for the stability of bilayers and the formation of foams. This can be understood in a microscopic picture: as microtubules from the two sides of the bilayer diffuse into the low-density region at its centre, they will interact among each other. Antipolar alignment with sliding is the only interaction that keeps the filaments aligned to the axis perpendicular to the bilayer and that will bring them back in place on the opposite sides of the line defect at its centre.

The importance of antipolar sliding explains why polar bilayer foams have not been observed in previous theoretical studies: a fully polar interaction ($\omega_c = \pi$), as was investigated in [12, 13, 23], will disrupt the bilayer as the microtubules on opposite sides interact; a fully symmetric interaction ($\omega_c = \pi/2$) as discussed in [14] will lead to dominating nematic order, so that a polar bilayer cannot take shape.

To inspect the role of bound motor anisotropy, we vary the parameter ξ at fixed η and $\bar{\rho}$. As for the critical angle, increasing ξ leads to a lower critical density ρ_c (see eq. (2.43a)), so that keeping $\bar{\rho}$ fixed increases the distance from criticality. Nonetheless, we see that at higher values of ξ active foams disappear and give way to branching micelles (see Fig. 12). This hints at the fact that strong tip accumulation is necessary for the formation of foams. Indeed, a non-zero value of ξ means that the a_is defined in (2.58) will be non-vanishing. This is also the case when we do not take the strong tip accumulation limit, i.e. for finite Ξ and τ_0. Thus, by increasing ξ we get a hint of what happens when there is no strong tip accumulation: the foams become unstable. Microscopically, this can be understood as follows: for finite τ_0, there is a large domain at the end of the microtubules where the interaction strength is increased. If this domain is too large, the microtubules of the bilayers will frequently interact with the filaments behind them, which leads to a disruption of the bilayer. The strong tip accumulation, on the other hand, ensures that the interaction is limited to the central region of the bilayer, so that it remains stable.

3.1.3 The motor Peclét number

To inspect the role of the inhomogeneity of the free motor field m, we vary the Peclét number $\gamma = v_m/D_m$ (see Fig. 13). As discussed below eq. (2.23), the strength of γ will determine the strength of the gradients of the motor field. For $\gamma = 0$, the motor field is completely homogeneous, while for $\gamma > 0$ motor gradients will align with the polarisation field.

Inspecting the region where the micelle-foam transition is found (i.e. for low ω_c and intermediate η) for $\gamma = 0$, we observe the formation of aster-like structures for all initial densities. However, the density field does not form a ring around the centre of these structures, but instead plateaus far from the centre. Hence, unlike micelles, which are well-separated by broad low-density regions, the asters in the $\gamma = 0$ case are neighbouring each other, separated by depleted defect lines where the polarisation changes direction. Only at non-vanishing γ do these asters separate, giving way to stable micelles or bilayer structures depending on the initial density $\bar{\rho}$, as we saw in Fig. 6. Increasing γ further affects the length scale on which the density decays outside of the central defect, in both micelles and bilayers. This happens because for non-zero γ the inward-pointing polarisation gives rise to gradients in the motor field, which point towards the centre of the micelle and of the bilayer. This leads to a weakening of the linear Ginzburg-Landau term in (2.44) in regions far from the centre, which causes a suppression of the order in these regions. As we will see in section 3.2, however, gradients in the order induce gradients in the density: Hence, the space between individual micelles as well as between individual bilayers is depleted from microtubules. This depletion depends on the strength of γ, which thus selects the external length scale of the micelles and bilayers.

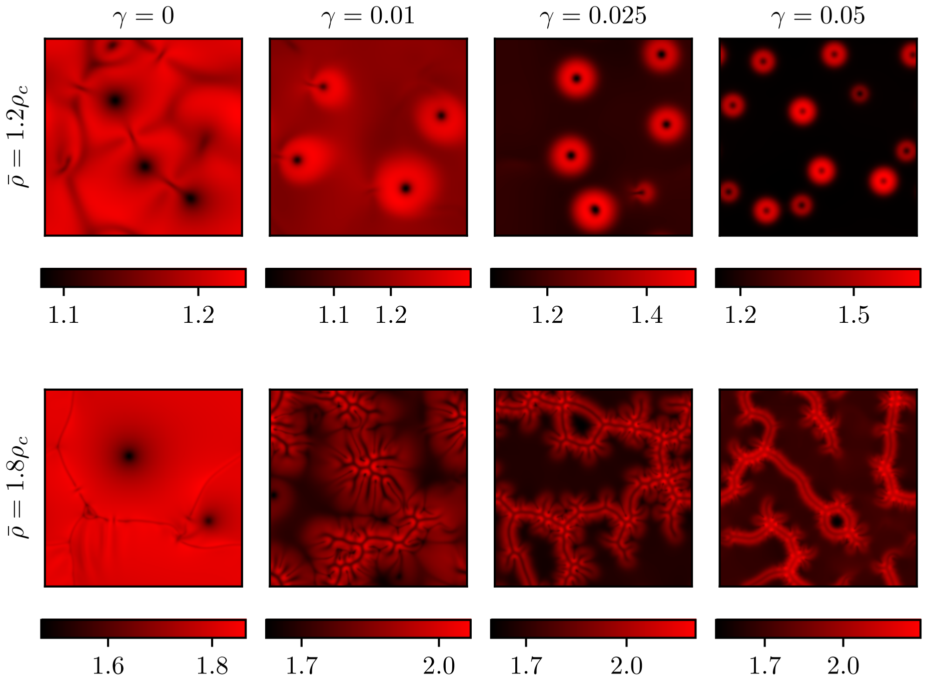

Figure 13: Snapshots of the ρ field for fixed $\omega_c = 2.18$, $\eta = 0.56$, $\alpha = 0.7$, $\xi = 0$. System size 60×60. For $\gamma = 0$, i.e. a homogeneous free motor field, the simulations show points of depleted density (asters) with the polarisation pointing inward. Unlike for micelle solutions, the density shows a plateau far from these depleted centres, with defect lines arising where the polarisation changes its direction. As γ is activated, an external length scale emerges on which the density decays far from the central defect, both for micelles (top row) and bilayer structures (bottom row). This length scale becomes shorter as γ is increased. For micelles, this means that the distance of separation between one micelle and the other is increased; furthermore, the number of coexisting micelles is larger. For bilayer structures, on the other hand, as γ is increased and the microtubule density accumulates in a smaller portion of space, branching micelles give way to bilayer networks with loops (i.e. foams).

3.1.4 The excluded volume strength α

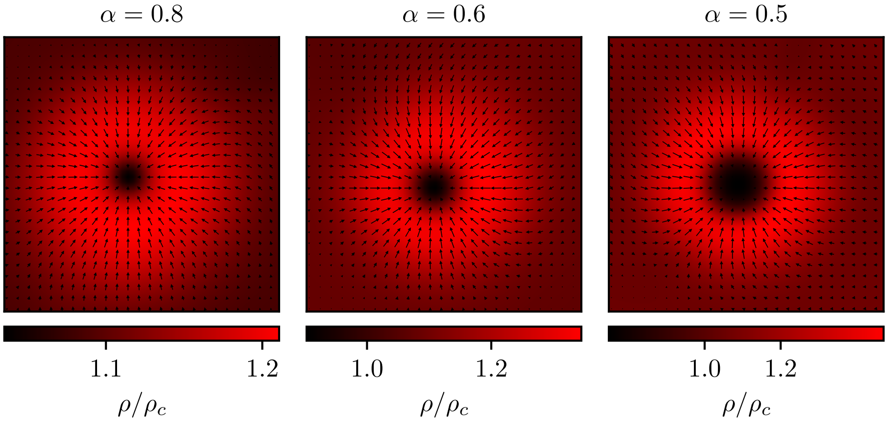

Figure 14: Details (15 × 15) of snapshots of the ρ field for fixed $\bar{\rho} = 1.1\rho_c$, $\omega_c = 2.18$, $\eta = 0.56$, $\xi = 0$, $\gamma = 0.02$. Run time $t = 300$, system size 60×60. As α is decreased, the micelles open up, exhibiting a larger length scale of the depleted region in the centre.

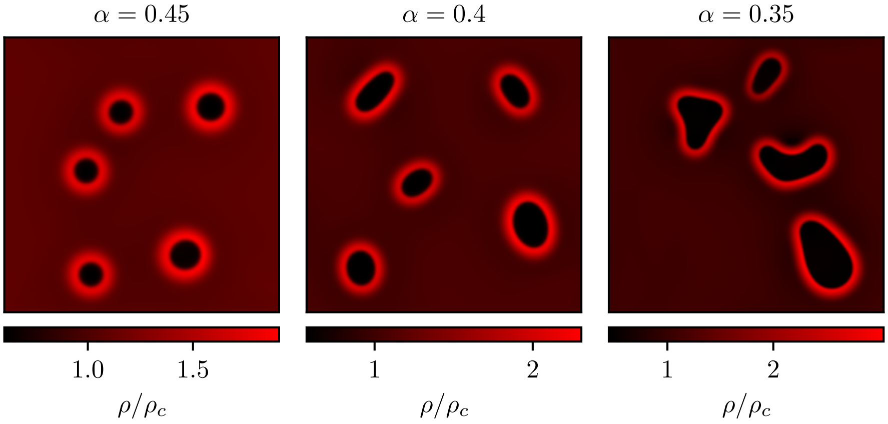

Figure 15: Snapshots of the ρ field for fixed $\bar{\rho} = 1.1\rho_c$, $\omega_c = 2.18$, $\eta = 0.5$, $\xi = 0$, $\gamma = 0.02$. System size 60×60. Color bars in units of ρ_c. As α is decreased, the micelles deviate more and more from a symmetric circular shape.

Before we discuss the effect of changing the excluded volume strength α in the simulations, it is useful to recall what this amounts to in physical terms. As we discussed below eq. (2.37), the definition of the excluded volume strength $\alpha = D_r/G$ includes the interaction rate G, into which we absorbed the average motor density $\bar{m}_{\text{ph}}$. If we increase α while while keeping $\bar{\rho}$ fixed, therefore, we are decreasing the total amount of motors in the system while keeping the distance to criticality $m_{\text{ph}}\rho_{\text{ph}}$ fixed, i.e. effectively we are increasing the physical microtubule density ρ_{ph}. On the other hand, keeping α fixed and increasing $\bar{\rho}$ corresponds to increasing the physical microtubule density at fixed motor density.

If we start in a regime where micelles are found, as α is decreased, the length scale of the depleted centre is increased (see Fig. 14). Lowering α more causes the micelles to lose their circular shape (see Fig. 15). The first breaking of spherical symmetry encountered is the elongation of the micelles along an axis; decreasing α even more activates higher instability modes, and we find micelles with more complicated shapes.

Since lower values of α correspond to higher motor concentrations in a physical system, we can think of this shape instability taking place in time as well, since due to the inward-pointing polarisation motors will be advected more and more into the inside of the micelles, increasing the local motor density. Thus, we expect micelles to undergo a kinetic pathway in which they first open up and then lose their spherical symmetry.

3.2 Understanding the terms in the equations

In this section, we inspect the equations mathematically and discuss the effect each term has on the dynamics of the density and polarisation. The intuition we will gain about these terms will be useful to interpret the analytical expressions we will derive in later sections. In the following, we neglect the inhomogeneity of the motor field m, since for small γ it is negligible on the local scale.

3.2.1 Terms in the density equation

The density equation (2.64a) is a continuity equation of the form:

$$\partial_t \rho + \boldsymbol{\nabla} \cdot \boldsymbol{J} = 0. \tag{3.1}$$

Neglecting motor inhomogeneity, the conserved flux reads as follows:

$$\boldsymbol{J} = -\boldsymbol{\nabla}\big(D_\rho \rho + m\nu\rho^2 + \alpha_2\rho^2 + \alpha_3\rho^3\big) - \chi_1[(\boldsymbol{p}\cdot\boldsymbol{\nabla})\boldsymbol{p} + (\boldsymbol{\nabla}\cdot\boldsymbol{p})\boldsymbol{p}] - \chi_2\boldsymbol{\nabla}p^2. \tag{3.2}$$

The first term of this flux can be written as $\boldsymbol{J}_\rho = -D_{\text{eff}}\boldsymbol{\nabla}\rho$, with an effective diffusivity D_{eff} emerging from the combined effect of diffusion (D_ρ), aligning interactions (ν) and excluded volume interactions ($\alpha_{2,3}$):

$$D_{\text{eff}} := D_\rho + 2m\nu\rho + 2\alpha_2\rho + 3\alpha_3\rho^2. \tag{3.3}$$

This term leads to an isotropic diffusive flux that for $D_{\text{eff}} > 0$ flows into regions of lower density, evening out the gradients.

The other terms, which we summarise as $\boldsymbol{J}_\chi$, are polarisation-dependent. To understand the different fluxes in terms of order direction and amplitude, we write:

$$\boldsymbol{p} = p\hat{\boldsymbol{n}}, \tag{3.4}$$

where $p > 0$ is the order amplitude and the unit vector $\hat{\boldsymbol{n}}$ points along the order direction. Moreover, we define a unit vector $\hat{\boldsymbol{n}}_\perp$ which is clockwise perpendicular to $\hat{\boldsymbol{n}}$, s.t. $\{\hat{\boldsymbol{n}}_\perp, \hat{\boldsymbol{n}}\}$ forms a right-handed orthonormal basis. Then, the polarisation-dependent flux from eq. (3.2) reads:

$$\begin{aligned}
\boldsymbol{J}_\chi &= -\chi_1 p\,[(\hat{\boldsymbol{n}}\cdot\boldsymbol{\nabla})(p\hat{\boldsymbol{n}}) + \boldsymbol{\nabla}\cdot(p\hat{\boldsymbol{n}})\hat{\boldsymbol{n}}] - \chi_2\boldsymbol{\nabla}p^2 \\
&= -\chi_1 p\left[p\partial_\parallel\hat{\boldsymbol{n}} + 2(\partial_\parallel p)\hat{\boldsymbol{n}} + (\boldsymbol{\nabla}\cdot\hat{\boldsymbol{n}})p\hat{\boldsymbol{n}}\right] - \chi_2[(\partial_\parallel p^2)\hat{\boldsymbol{n}} + (\partial_\perp p^2)\hat{\boldsymbol{n}}_\perp] \\
&= -\chi(\partial_\parallel p^2)\hat{\boldsymbol{n}} - \chi_1 p^2(\boldsymbol{\nabla}\cdot\hat{\boldsymbol{n}})\hat{\boldsymbol{n}} - \chi_1 p^2\partial_\parallel\hat{\boldsymbol{n}} - \chi_2(\partial_\perp p^2)\hat{\boldsymbol{n}}_\perp,
\end{aligned} \tag{3.5}$$

where we have introduced $\partial_{||} = \hat{\boldsymbol{n}} \cdot \boldsymbol{\nabla}$ and $\partial_\perp = \hat{\boldsymbol{n}}_\perp \cdot \boldsymbol{\nabla}$, as well as $\chi = \chi_1 + \chi_2$.

Four fluxes appear in equation (3.5), which are shown in Figure 16. The first term in the equation leads to accumulation of density in highly ordered regions (contractility) for $\chi < 0$, or enhanced diffusion away from these regions (extensility) for $\chi > 0$. Only the first case will be relevant in the following, so we call this term the *contractile flux*. The second term, the *splay flux*, leads to a flow along the splay vector $(\boldsymbol{\nabla} \cdot \hat{\boldsymbol{n}})\hat{\boldsymbol{n}}$ for $\chi_1 < 0$, while the third term, the *bend flux*, advects density towards the interior of the osculating circle of the polarisation streamline. Note that it is perpendicular to the order, since $\hat{\boldsymbol{n}} \cdot \partial_{||}\hat{\boldsymbol{n}} = 0$ due to the unit vector condition. The last term causes enhanced diffusion ($\chi_2 > 0$) or contractile behaviour ($\chi_2 < 0$) perpendicularly to the order, which is why we denote it as *transversal flux*. We can classify these four fluxes as follows:

	Gradients in the order strength p	Gradients in the order orientation $\hat{\boldsymbol{n}}$
Flux along the order	Contractile flux (χ)	Splay flux (χ_1)
Flux perpendicular to the order	Transversal flux (χ_2)	Bend flux (χ_1)

3.2.2 Terms in the polarisation equation

To understand the effect of the terms in the polarisation equation (2.64b), we separate the dynamics of the order amplitude and the order orientation. To this goal, we write $\boldsymbol{p} = p\hat{\boldsymbol{n}}$ as before; by taking the scalar product of equation (2.64b) with $\hat{\boldsymbol{n}}$ and $\hat{\boldsymbol{n}}_\perp$ respectively, and using that $\hat{\boldsymbol{n}} \cdot \partial_t \hat{\boldsymbol{n}} = 0$ holds to preserve the unit vector length, we find:

$$\begin{aligned} \partial_t p &= \left[(m\rho/\rho_c - 1) - m^2\beta p^2 - \lambda_2 p \boldsymbol{\nabla} \cdot \hat{\boldsymbol{n}}\right] p \\ &\quad + \kappa_1(\hat{\boldsymbol{n}} \cdot \nabla^2 \boldsymbol{p}) + \kappa_2 \partial_{||}(\boldsymbol{\nabla} \cdot \boldsymbol{p}) \\ &\quad + \zeta_1 \partial_{||}\rho - \lambda p \partial_{||} p, \qquad (3.6a) \\ p\hat{\boldsymbol{n}}_\perp \cdot \partial_t \hat{\boldsymbol{n}} &= \kappa_1(\hat{\boldsymbol{n}}_\perp \cdot \nabla^2 \boldsymbol{p}) + \kappa_2 \partial_\perp(\boldsymbol{\nabla} \cdot \boldsymbol{p}) \\ &\quad - \lambda_1 p^2 \hat{\boldsymbol{n}}_\perp \cdot (\partial_{||}\hat{\boldsymbol{n}}) \\ &\quad + \zeta_1 \partial_\perp \rho + \zeta_2 \partial_\perp p^2. \qquad (3.6b) \end{aligned}$$

We have introduced the shorthand $\lambda = \lambda_1 + \lambda_2 - 2\zeta_2$.

In the dynamic equation for the order strength (3.6a), the first line describes an ordering transition taking place in regions with $m\rho > \rho_c$, whose exponential growth is saturated by the β term. In addition to the standard Ginzburg-Landau ordering, however, we see that for $\lambda_2 < 0$ the order is amplified (reduced) in regions with positive (negative) splay, and vice versa for $\lambda_2 > 0$. We call this effect *active splay*. As λ_2 does not appear in eq. (3.6b), it has no direct effect on the orientational dynamics.

The λ_1 term in the orientational equation (3.6b) contains $\hat{\boldsymbol{n}}_\perp \cdot (\partial_{||}\hat{\boldsymbol{n}})$, which describes how much the orientation is changing along the polarisation streamline. Note that $\partial_{||}\hat{\boldsymbol{n}}$ has no component in the direction of $\hat{\boldsymbol{n}}$. Since this term appears in the orientational equation,

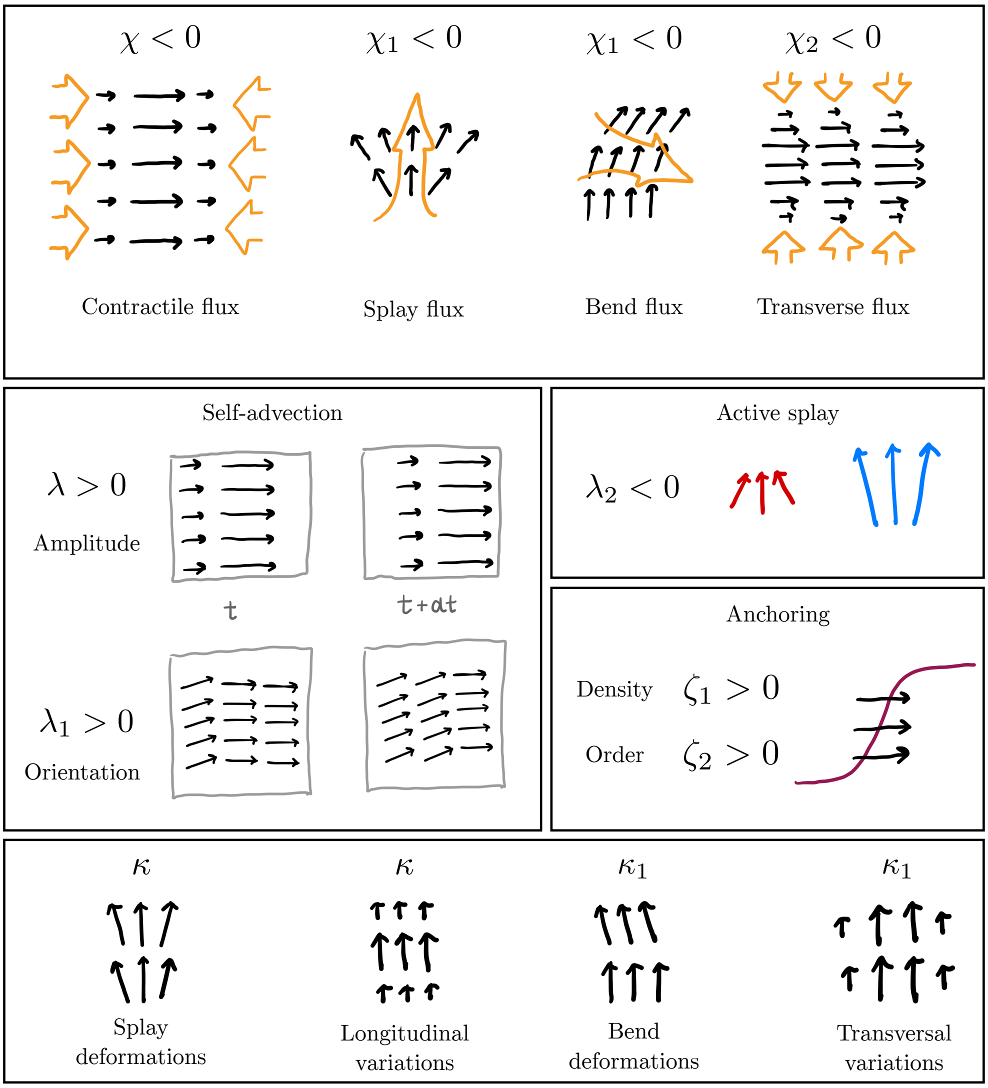

Figure 16: Cartoon illustrating the effects of some of the terms in the continuum equations (2.64).

this change is propagated along the polarisation vector: In other words, for $\lambda_1 > 0$, variations in the order orientation are advected *forward* with respect to the polarisation, and for $\lambda_1 < 0$ they are advected *backward*. Therefore, we call this term *orientational self-advection*.

A similar term appears in the order strength equation: $\partial_{\|} p$ describes how the order strength varies along the streamline. This change is then propagated forwards for $\lambda > 0$ and backwards for $\lambda < 0$. We refer to this as *self-advection of the order amplitude*. Note that the two kinds of self-advection have different coefficients, which can have different signs in general.

Next, we look at the ζ_1 term. In the orientational equation, it will rotate the order orientation towards gradients of ρ for $\zeta_1 > 0$, and against these gradients for $\zeta_1 < 0$. In the order strength equation, it increases the order when the density gradients and the polarisation are pointing in the same direction, and it decreases it when they are opposite.

We denote this effect as *density anchoring.* ζ_2 has a similar role, but it couples to gradients in the order strength: in this case, we speak of *self-anchoring.*

We are left to analyse the $\kappa_{1,2}$ terms. The easiest way to do this is to compare the equations to an equilibrium system. Indeed, we can define a free energy such that the polarisation follows model A dynamics, in addition to purely active terms that cannot be written as derivatives of the free energy (see [16]). The free energy reads:

$$\begin{aligned}\mathcal{F} = \int \mathrm{d}^2x \Bigg[&-\frac{1}{2}\left(\frac{m\rho}{\rho_c}-1\right)p^2 + \frac{\beta m^2}{4}p^4 \\ &- \zeta_1(\boldsymbol{p}\cdot\boldsymbol{\nabla})\rho - \zeta_2(\boldsymbol{p}\cdot\boldsymbol{\nabla})p^2 \\ &+ \frac{\kappa_1}{2}(\partial_i p_j)(\partial_i p_j) + \frac{\kappa_2}{2}(\boldsymbol{\nabla}\cdot\boldsymbol{p})^2\Bigg]. \end{aligned} \tag{3.7}$$

The dynamics of the polarisation can then be written as:

$$\partial_t \boldsymbol{p} = -\frac{\delta\mathcal{F}}{\delta\boldsymbol{p}} - \lambda_1(\boldsymbol{p}\cdot\boldsymbol{\nabla})\boldsymbol{p} - (\lambda_2 - 2\zeta_2)(\boldsymbol{\nabla}\cdot\boldsymbol{p})\boldsymbol{p}. \tag{3.8}$$

Note that in the absence of self-advection, i.e. $\lambda = \lambda_1 = 0$, the active terms vanish, and we are left with pure gradient dynamics. However, even in this case, the full system is still active, since the ρ equation cannot be derived from a free energy.

The first line of the free energy (3.7) leads to the Ginzburg-Landau transition, while the second line favours aligning the polarisation along gradients of the density and order for $\zeta_{1,2} > 0$ (or against them for $\zeta_{1,2} < 0$). This reproduces the anchoring discussed above. The line of interest for us is the last one, since it includes $\kappa_{1,2}$. Up to total derivatives, we have:

$$\begin{aligned}(\partial_i p_j)(\partial_i p_j) &= p^2(\boldsymbol{\nabla}\cdot\hat{\boldsymbol{n}})^2 + p^2(\partial_\parallel\hat{\boldsymbol{n}})^2 + (\boldsymbol{\nabla}p)^2 \\ &\quad + (\boldsymbol{\nabla}\cdot\hat{\boldsymbol{n}})\partial_\parallel p^2 - (\boldsymbol{\nabla}p^2)\cdot(\partial_\parallel\hat{\boldsymbol{n}}) && (3.9\text{a}) \\ (\boldsymbol{\nabla}\cdot\boldsymbol{p})^2 &= p^2(\boldsymbol{\nabla}\cdot\hat{\boldsymbol{n}})^2 + (\partial_\parallel p)^2 + (\boldsymbol{\nabla}\cdot\hat{\boldsymbol{n}})\partial_\parallel p^2. && (3.9\text{b})\end{aligned}$$

Hence, introducing $\kappa = \kappa_1 + \kappa_2$, the $\kappa_{1,2}$ terms in the free energy density can be written as:

$$\begin{aligned}&\frac{1}{2}\left(\kappa[p^2(\boldsymbol{\nabla}\cdot\hat{\boldsymbol{n}})^2 + (\partial_\parallel p)^2] + \kappa_1[p^2(\partial_\parallel\hat{\boldsymbol{n}})^2 + (\partial_\perp p)^2]\right) && (3.10\text{a}) \\ &+ \frac{\kappa}{2}\left((\boldsymbol{\nabla}\cdot\hat{\boldsymbol{n}})\partial_\parallel p^2 - (\boldsymbol{\nabla}p^2)\cdot(\partial_\parallel\hat{\boldsymbol{n}})\right). && (3.10\text{b})\end{aligned}$$

We see that κ penalises splay deformations of the order orientation as well as longitudinal variations of the order amplitude. On the other hand, κ_1 penalises bend deformations as well as transversal variations of the order amplitude. Finally, κ provides an additional anchoring effect, which favours orienting gradients in the polarisation antiparallel to the splay vector $(\boldsymbol{\nabla}\cdot\hat{\boldsymbol{n}})\hat{\boldsymbol{n}}$ as well as parallel to the bending direction. An overview over the effect of the various terms in the polarisation equation can be found in Fig. 16.

3.3 The phenomenological model

The equations (2.64) are rigorously derived from interaction rules. Each term there is a function of the parameters of our interaction model. This provides us with the tools

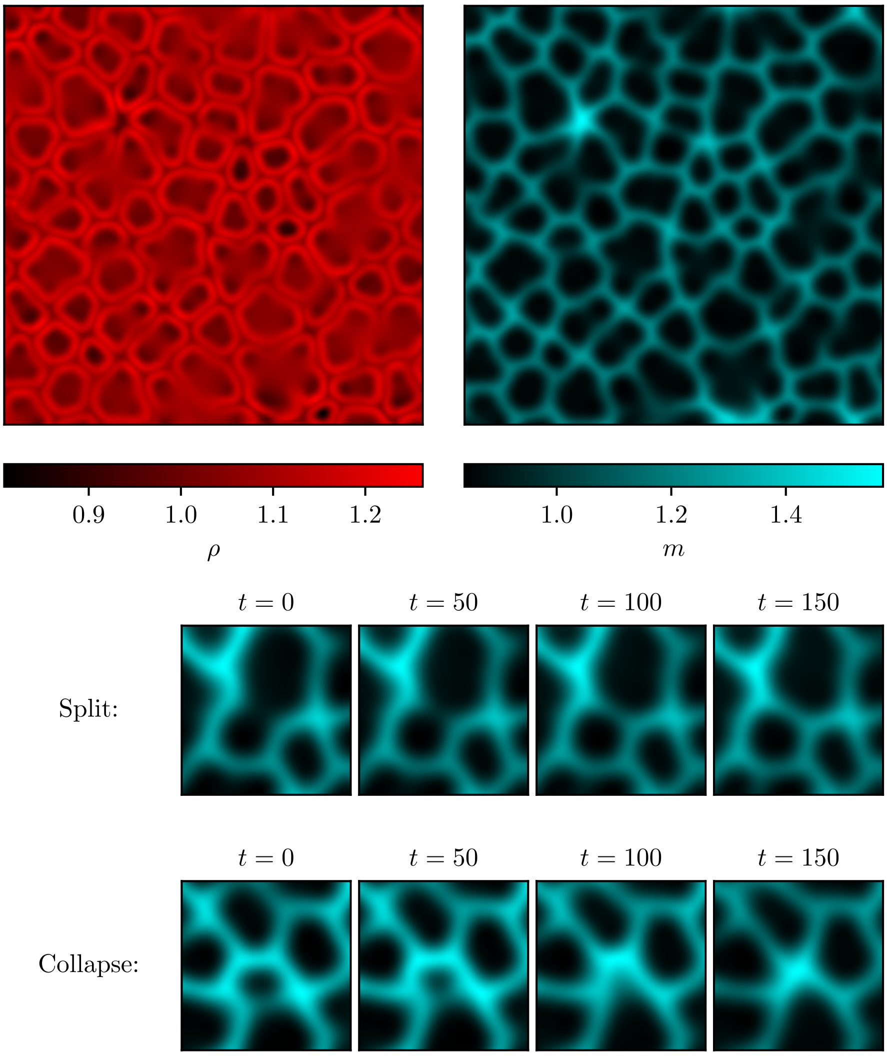

Figure 17: Top: Active foam found in the phenomenological model. Snapshot at $t = 1350$ of a simulation starting from a disordered homogeneous state in a 120×120 geometry, with $\bar{\rho} = 1.1$, $D_\rho = 0.1$, $\alpha_2 = \alpha_3 = 0.05$, $\hat{\chi}_1 = -0.2$, $\hat{\chi}_2 = 0.1$, $\hat{\kappa}_1 = 0.05$, $\hat{\lambda}_1 = 0.4$, $\hat{\lambda}_2 = -0.7$, $\hat{\zeta}_1 = 0.1$, $\hat{\kappa}_2 = \hat{\zeta}_2 = \nu = 0$, $D_m = 0.2$, $v_m = 0.04$. Bottom: A cell splitting event and a cell collapse event are shown to illustrate foam activity. The snapshots show the motor field in a 30×30 detail of the larger simulation. Two branches from different areas of the network can meet to form a new edge, thus splitting an existing cell into two parts (top row). A cell collapses when two of its bilayer walls meet (bottom row).

necessary to analyse the link between microscopy and collective behaviour on a qualitative level. To achieve greater generality, however, it can be useful to take a different perspective and to forget about the dependence of the continuum model on microscopic details. This is done by keeping the form of the equations intact, and treating the coefficients in the equations no longer as function of the microscopy, but instead as free parameters that can be varied arbitrarily.

Of course, this vastly amplifies the parameter space, allowing for a full exploration of the phenomenology contained in the set of equations that was derived from a very specific microscopic model. This approach is justified by the observation that a different microscopic model or a distinct choice of the coarse-graining procedure will lead to equations with the same shape, but a different functional dependence of the individual terms on interaction parameters, so that other parts of the full phenomenological parameter space might be accessed by changing the underlying microscopic model. Moreover, the phenomenological approach stresses the importance of the mesoscopic perspective on collective behaviour, where the phenomena are not interpreted on the level of individual interacting agents, but instead as feedback and competition mechanisms among different terms in the equations governing the coarse-grained fields. To this goal, the intuition we built up in the previous section is fundamental.

In the following, we will derive expressions for the length scales and instabilities emerging in the system in terms of the coefficients of the equations. To verify the validity of these expressions, it will be useful to take the phenomenological perspective and vary the different coefficients independently. In the derived model, $\chi_{1,2}$, $\kappa_{1,2}$, $\zeta_{1,2}$ and $\lambda_{1,2}$ are not only functions of the microscopic parameters, but also of the motor field m. We simplify this general functional dependence by making a linear ansatz for each of these coefficients, i.e by writing $\chi_1(m) = m\hat{\chi}_1$, $\kappa_1(m) = m\hat{\kappa}_1$, etc. Furthermore, we rescale the MT density ρ as well as the polarisation $\boldsymbol{p}$ such that $\rho_c = 1 = \beta$.

The phenomenological equations then read:

$$\begin{aligned}
\partial_t\rho &= \nabla^2\big(D_\rho\rho + \nu m\rho^2 + \alpha_2\rho^2 + \alpha_3\rho^3\big) \\
&\quad +\hat{\chi}_1\partial_i\partial_j(mp_ip_j) + \hat{\chi}_2\nabla^2\big(mp^2\big), \qquad (3.11a) \\
\partial_t\boldsymbol{p} &= \big[(m\rho-1) - m^2p^2\big]\,\boldsymbol{p} \\
&\quad +\hat{\kappa}_1 m\nabla^2\boldsymbol{p} + \hat{\kappa}_2 m\boldsymbol{\nabla}(\boldsymbol{\nabla}\cdot\boldsymbol{p}) \\
&\quad +\hat{\zeta}_1 m\boldsymbol{\nabla}\rho + \hat{\zeta}_2 m\boldsymbol{\nabla}p^2 \\
&\quad -\hat{\lambda}_1 m(\boldsymbol{p}\cdot\boldsymbol{\nabla})\boldsymbol{p} - \hat{\lambda}_2 m(\boldsymbol{\nabla}\cdot\boldsymbol{p})\boldsymbol{p}. \qquad (3.11b)
\end{aligned}$$

The quantities with the hat, as well as the parameters D_ρ, ν and $\alpha_{2,3}$, are now no longer functions of microscopic parameters, but free parameters of the model that can we vary independently.

3.3.1 Phenomenological active foams

As a first application of the phenomenological model, we search the new, extended parameter space for active foams that more closely resemble those observed in the experiments performed in [1] in terms of activity and smoothness of the network. Fig. 17 shows snapshots from an active foam obtained by varying the phenomenological parameters. The continuous reconfiguration of this foam consists in the creation of new branches along the bilayer edges, that can connect to other branches in other parts of the network to form new cells, as well as the collapse of cells as two bilayers collide.

3.4 Profiles and length scales

3.4.1 Bilayer profile

To analyse the bilayer profile, we assume that the fields vary only in one direction, namely the one perpendicular to the bilayer. We choose the coordinate system such that this coincides with the x axis. Additionally, we assume that the polarisation is perpendicular to the bilayer, $\boldsymbol{p} = p\hat{\boldsymbol{e}}_x$. Then, the polar continuum model (2.64) reduces to the following one-dimensional equations:

$$\partial_t \rho = \partial_x^2 (D_\rho \rho + m\nu\rho^2 + \alpha_2\rho^2 + \alpha_3\rho^3 + \chi p^2), \tag{3.12a}$$

$$\partial_t p = (m\rho/\rho_c - 1)p - \beta m^2 p^3 + \kappa\partial_x^2 p + \zeta_1 \partial_x \rho - \lambda p \partial_x p, \tag{3.12b}$$

$$\partial_t m = D_m \partial_x^2 m - v_m \partial_x (mp). \tag{3.12c}$$

We want to find a stationary solution of these equations, where the polarisation changes from plus-pointing to minus-pointing. Since we expect the fields to be continuous, this implies the existence of a point where $p = 0$, which will be the centre of the bilayer. We place this at $x = 0$. If we assume the bilayer to be symmetric, this point will also be a maximum in the motor field (due to the advection of motors from both sides of the bilayer into the centre) as well as a minimum in the density field (due to the contractile fluxes that will deplete the centre, accumulating material in the ordered regions on either side of the bilayer).

In the following, we assume γ to be small. Thus, in a first approximation, we can take the motor field to be constant, $m = m_0$.

Microtubule density profile

First, we look at the density equation, eq. (3.12a). Setting it to zero, and integrating it from $x = 0$ gives:

$$\partial_x (D_\rho \rho + m_0\nu\rho^2 + \alpha_2\rho^2 + \alpha_3\rho^3 + \chi p^2) = 0. \tag{3.13}$$

Here, we used that this expression vanishes at $x = 0$ due to the extremal condition of ρ, p^2 and m. Integrating it again, we find:

$$D_\rho \rho + m_0\nu\rho^2 + \alpha_2\rho^2 + \alpha_3\rho^3 + \chi p^2 = D_\rho \rho_- + m_0\nu\rho_-^2 + \alpha_2\rho_-^2 + \alpha_3\rho_-^3, \tag{3.14}$$

where $\rho_- = \rho(x = 0)$ is the density at the centre of the bilayer. Assuming weak phase separation, we can linearise the density around a reference value ρ_0. Then, we find:

$$\rho(x) = \rho_- - \frac{\chi}{D_{\text{eff}}} p^2(x), \tag{3.15}$$

where D_{eff} is given by the expression in eq. (3.3), with ρ_0 and m_0 used as the values for the microtubule and motor concentrations. This equation shows the effect of the contractile flux $\chi < 0$: in regions where the order is stronger, there will be an accumulation of density, while the centre of the bilayer is depleted.

Assuming that at the density maxima of the bilayer the polarisation profile is sufficiently flat, we can neglect the derivative terms in (3.12b) at that point, such that the polarisation at the maximum reads:

$$p_+^2 = \frac{m_0\rho_+ - \rho_c}{\beta m_0^2 \rho_c}, \tag{3.16}$$

where ρ_+ is the density at the maximum. Plugging this into (3.15), we find:

$$\Delta\rho := \rho_+ - \rho_- = -\bar{\chi}(\rho_+ - \rho_c/m_0), \tag{3.17}$$

showing again that phase separation is driven by the contractile flux. Here, $\bar{\chi}$ is defined as:

$$\bar{\chi} = \frac{\chi}{\beta m_0 \rho_c D_{\text{eff}}}. \tag{3.18}$$

This can be interpreted as the effective contractility emerging in ordered regions, measured in relation to the isotropic effective diffusivity D_{eff}. The total diffusivity along the order is given by $D_{\text{eff}}(1+\bar{\chi})$. Analogously, we define $\bar{\chi}_2$, so that $D_{\text{eff}}(1+\bar{\chi}_2)$ is the diffusivity transversally to the order.

Equation (3.17) can be rewritten as:

$$\frac{m_0\rho_- - \rho_c}{m_0\rho_+ - \rho_c} = 1 + \bar{\chi}. \tag{3.19}$$

Hence, when $\bar{\chi}$ reaches the critical value of -1, the centre of the bilayer drops below criticality, making the ratio on the left hand side of this equation negative.

Finally, if we use the average between the maximum and the minimum as the reference density for the linearisation, we can write $\rho_\pm = \rho_0 \pm \Delta\rho/2$ and express the amplitude of the phase separation in terms of ρ_0 only:

$$\Delta\rho = \frac{-2\bar{\chi}}{2+\bar{\chi}}(\rho_0 - \rho_c/m_0). \tag{3.20}$$

Polarisation profile: Limit of strong activity

Next, we inspect the polarisation profile. Plugging (3.15) into (3.12b) at stationarity, we find:

$$0 = (m_0\rho_-/\rho_c - 1)p - \beta m_0^2(1+\bar{\chi})p^3 + \kappa\partial_x^2 p - \bar{\lambda} p \partial_x p, \tag{3.21}$$

where we've defined:

$$\bar{\lambda} = \lambda + 2\zeta_1\chi/D_{\text{eff}}. \tag{3.22}$$

The differential equation (3.21) can be solved analytically in two limits, namely when either one of the last two terms is negligible compared to the other.

If the active term proportional to $\bar{\lambda}$ dominates over the elasticity term κ, equation (3.21) becomes a first-order ODE, which can be solved using separation of variables. With the condition $p(x=0) = x$, the solution is given by:

$$p(x) = \begin{cases} -A\tanh(x/\ell_{\text{BL}}) & \text{for} \quad (1+\bar{\chi})(m_0\rho_- - \rho_c) > 0, \\ -A\tan(x/\ell_{\text{BL}}) & \text{for} \quad (1+\bar{\chi})(m_0\rho_- - \rho_c) < 0. \end{cases} \tag{3.23}$$

Due to (3.19), the signs of $(1+\bar{\chi})$ and $(m_0\rho_- - \rho_c)$ always agree. So, we expect the bilayer to have a tanh profile in the strong $\bar{\lambda}$ limit. However, as we will see below, the second solution will be of relevance for the micelles, where this sign constraint is not necessarily fulfilled.

A is an amplitude parameter, which reads (using (3.19)):

$$A = \sqrt{\frac{m_0\rho_- - \rho_c}{(1+\bar{\chi})\beta m_0^2 \rho_c}} = \sqrt{\frac{m_0\rho_+ - \rho_c}{\beta m_0^2 \rho_c}}. \tag{3.24}$$

This gives us the equilibrium value of the polarisation at ρ_+, according to eq. (3.16).

The length scale ℓ_{BL} characterises the width of the profile, and is given by:

$$\ell_{\mathrm{BL}} = \frac{-A\bar{\lambda}}{m_0\rho_-/\rho_c - 1}. \tag{3.25}$$

To obtain a bilayer with inward-pointing microtubules (i.e. with the polarisation going from positive to negative values), this length should be positive. This requires $\bar{\lambda}$ and $m_0\rho_-/\rho_c - 1$ to have different signs. We can understand this as follows: a stationary bilayer with a finite length scale can only emerge if the Ginzburg-Landau ordering term and the $\bar{\lambda}$ term are in competition. $\bar{\lambda}$ includes the self-advection of the order strength λ as well as the density anchoring ζ_1. The former will tend to close the bilayer for $\lambda > 0$ (forward self-advection) and to open it up for $\lambda < 0$ (backward self-advection). The latter couples to the gradients in the microtubule density that arise via the action of the contractile flux χ (see the definition of $\bar{\lambda}$ in eq. (3.22)), and will tend to open up the bilayer for $\zeta_1 > 0$ and to close it for $\zeta_1 < 0$. The Ginzburg-Landau term, on the other hand, favours zero polarisation, and thus the existence of a wider bilayer, for $m_0\rho_-/\rho_c - 1 < 0$; instead, for $m_0\rho_-/\rho_c - 1 > 0$, it promotes order, and it will try to minimise the disordered region by closing the bilayer. It is the competition between these terms that selects the length scale on which a stationary bilayer can exist.

Polarisation profile: Limit of strong elasticity

The other limit of equation (3.21) is realised when the κ-dependent elasticity term dominates over the $\bar{\lambda}$ term. Since the equation is a 2nd order ODE in this limit, we need to provide a second condition in addition to $p(x=0)=0$ to obtain a solution. If we require the solution to saturate at $\mp A$ for $x \to \pm\infty$, we recover the well-known kink solution [31], assuming that the centre lies above criticality ($m_0\rho_- > \rho_c$):

$$p(x) = -A\tanh(x/\ell_{\mathrm{BL}}), \tag{3.26}$$

with A given by eq. (3.24), and the length scale ℓ_{BL} reading as follows:

$$\ell_{\mathrm{BL}}\Big|_{\bar{\lambda}=0} = \sqrt{\frac{2\kappa}{m_0\rho_-/\rho_c - 1}}. \tag{3.27}$$

This shows a competition between the Ginzburg-Landau term, which tries to minimise the region where there is no order even though the density is above criticality and pushes the bilayer together, and the elasticity term, which penalises gradients in the polarisation and hence pulls the bilayer apart.

To see what effect the $\bar{\lambda}$ term has in the limit where it is small compared to the κ term, we slowly turn it back on. To this goal, we assume that close to the centre of the bilayer the solution keeps approximately the same shape as in (3.26), with the main effect of the new term being a change of the length scale ℓ_{BL}. Close to $x \to 0$, we have $\partial_x p(x) \approx -A/\ell_{\mathrm{BL}}$. Substituting this into (3.21), we see that the linear term is modified, giving:

$$0 = \left(\frac{m_0\rho_-}{\rho_c} - 1 + \bar{\lambda}\frac{A}{\ell_{\mathrm{BL}}}\right) p - \beta m_0^2(1+\bar{\chi})p^3 + \kappa\partial_x^2 p. \tag{3.28}$$

This leads to a new term appearing in the length scale (3.27):

$$\ell_{\mathrm{BL}}\bigg|_{\bar{\lambda}=0} = \sqrt{\frac{2\kappa}{m_0\rho_-/\rho_c - 1 + \bar{\lambda}A\ell_{\mathrm{BL}}^{-1}}}, \tag{3.29}$$

yielding an implicit relation for ℓ_{BL}. Solving for the latter gives:

$$\ell_{\mathrm{BL}} = \Lambda_{\mathrm{BL}} + \sqrt{\Lambda_{\mathrm{BL}}^2 + \frac{2\kappa}{m_0\rho_-/\rho_c - 1}}, \tag{3.30}$$

with

$$\Lambda_{\mathrm{BL}} = \frac{-A\bar{\lambda}}{2(m_0\rho_-/\rho_c - 1)}. \tag{3.31}$$

We infer that the contribution of $\bar{\lambda}$ in the strong elasticity limit is similar to the one we discussed in eq. (3.25), namely that the combined action of self-advection λ and density anchoring ζ_1 leads to a narrower bilayer for $\bar{\lambda} > 0$, and a wider one for $\bar{\lambda} < 0$.

Equation (3.30) gives a criterion as to when we can neglect the $\bar{\lambda}$ term compared to the κ one, namely when the argument of the square root is dominated by κ – using (3.24), the condition reads:

$$\bar{\lambda}^2 \ll 8(m_0\rho_- - \rho_c)(1+\bar{\chi})\beta m_0^2\rho_c \cdot \kappa. \tag{3.32}$$

Note that for $\kappa \ll \bar{\lambda}^2$, eq. (3.30) gives back the length scale we derived in the other limit, eq. (3.25), provided that $\bar{\lambda}$ has the correct sign.

Besides the kink solution (3.26), the equation (3.21) also has other solutions in the strong κ limit, namely a different one for each value of the slope at the centre $\partial_x p(x=0)$. Since this slope should be negative to obtain a bilayer profile, however, we can still make a statement about its qualitative shape close to the centre. Indeed, by taking the derivative of (3.21), we find:

$$\partial_x^3 p(x=0) = -\frac{m_0\rho_-/\rho_c - 1}{\kappa}\partial_x p(x=0) + \bar{\lambda}[\partial_x p(x=0)]^2, \tag{3.33}$$

such that, for sufficiently small $\bar{\lambda}$, the third derivative of p is positive (like for a tanh profile) if the centre of the bilayer is above criticality, while it is negative (like for a tan profile) if the centre of the bilayer lies below criticality.

Motor concentration profile

To find the first-order correction to a constant motor profile, we require stationarity in the equation for the motor concentration (3.12c), using the solution for $\boldsymbol{p}$ derived for the $\gamma = 0$ case. Stationarity yields a flux balance condition of the form:

$$\partial_x \log m = \gamma p. \tag{3.34}$$

Integration gives:

$$m(x) = m_- \exp\biggl(\gamma \int_0^x \mathrm{d}x'\, p(x')\biggr), \tag{3.35}$$

where m_- is the motor concentration at the centre of the bilayer. Note that for $x > 0$ we have $p < 0$ and vice versa, so that this function decays on either side.

Using the tanh solution from eq. (3.23) and eq. (3.26), we find:

$$\begin{aligned} m(x) &= m_- \exp\biggl(-\gamma A \int_0^x \mathrm{d}x' \tanh\bigl(x'/\ell_{\mathrm{BL}}\bigr)\biggr) \\ &= m_- \exp\bigl(-\gamma A \ell_{\mathrm{BL}} \log\cosh\bigl(x'/\ell_{\mathrm{BL}}\bigr)\bigr) \\ &= m_- \cosh(x/\ell_{\mathrm{BL}})^{-\gamma A \ell_{\mathrm{BL}}}_{.} \end{aligned} \tag{3.36}$$

Bilayer profile: Summary

In summary, the stationarity condition yields a tanh-like solution for the polarisation in the strong $\bar{\lambda}$ limit (where $\bar{\lambda}$ should have the opposite sign compared to the Ginzburg-Landau term), as well as in the strong κ limit when the centre is above criticality. Inside the bilayer, between the two density maxima, we thus expect a profile of the following shape (where the density profile is obtained by plugging the polarisation solution into eq. (3.15)):

$$\rho(x) = \rho_- + \Delta\rho \tanh^2\biggl(\frac{x}{\ell_{\mathrm{BL}}}\biggr), \tag{3.37a}$$

$$p(x) = A \tanh\biggl(\frac{x}{\ell_{\mathrm{BL}}}\biggr), \tag{3.37b}$$

$$m(x) = m_- \cosh\biggl(\frac{x}{\ell_{\mathrm{BL}}}\biggr)^{-\gamma A \ell_{\mathrm{BL}}}_{.} \tag{3.37c}$$

When the centre of the profile lies below criticality (which requires strong contractility, $\bar{\chi} < -1$), on the other hand, in the strong κ limit we expect a change in the sign of $\partial_x^3 p(x = 0)$. This indicates a more complicated solution, which close the centre of the bilayer looks like a tan.

The length scale emerging from the tanh solution is given by (3.30), which agrees with eq. (3.25) in the strong $\bar{\lambda}$ limit (when $\mathrm{sgn}[(m_0\rho_- - \rho_c)\bar{\lambda}] = -1$). The length scale is selected by the competition of different terms:

Pulls bilayer apart (larger ℓ_{BL})	**Pushes bilayer together** (smaller ℓ_{BL})
Elasticity $\kappa > 0$	Ginzburg-Landau ordering $m_0\rho_- - \rho_c > 0$
Anchoring to density gradients $-\chi\zeta_1 > 0$	Self-advection $\lambda > 0$
Contractile flux $\chi < 0$	Effective diffusion $D_{\mathrm{eff}} > 0$

The two terms in the last line enter the length scale through the dependence on A: a larger $|\bar{\chi}|$ leads to stronger phase separation, making the bilayer wider.

Measuring the bilayer

To verify our predictions for the bilayer profile and its length scale, we performed numerical simulations of the phenomenological model (3.11) in the regime where active foams can be found, for different parameters listed in Fig. 18. For each parameter set, we measured the cross section profile of a bilayer, by choosing a pair of symmetric cells. The two density maxima were used as the limits of the inside of the bilayer, and the data points between these density maxima were used to fit the following functions, which generalise (3.37):

$$\rho(x) = c_1 + c_2 \tanh\left(\frac{x - x_0^\rho}{\ell_\rho}\right)^2, \tag{3.38a}$$

$$p(x) = -c_3 \tanh\left(\frac{x - x_0^p}{\ell_p}\right), \tag{3.38b}$$

$$m(x) = c_4 \cosh\left(\frac{x - x_0^m}{\ell_m}\right)^{-c_5}, \tag{3.38c}$$

where p is the component of the polarisation parallel to the cross section and the x_0^i, ℓ_i and c_i are fitting parameters. An example of such a fit is shown on the left side of Fig. 18. The right side of the figure shows the collapse of the profiles from all parameter sets obtained by plotting $(\rho - c_1)/c_2$, p/c_3 and $(m/c_4)^{1/c_5}$ against $(x - x_0)/\ell$.

To verify the validity of equation (3.30), we rewrite it as:

$$\tilde{\ell}_{\mathrm{BL}} = \tilde{\Lambda}_{\mathrm{BL}} + \sqrt{\tilde{\Lambda}_{\mathrm{BL}}^2 + \hat{\kappa}}, \tag{3.39}$$

where we plugged in $\kappa = m_0\hat{\kappa}$, and introduced a rescaled length scale $\tilde{\ell}_{\mathrm{BL}} = \sqrt{\frac{m_-\rho_- - 1}{2m_0}}\ell_{\mathrm{BL}}$ (note that $\rho_c \equiv 1$ in the phenomenological model), as well as a rescaled parameter $\tilde{\Lambda}_{\mathrm{BL}} = \sqrt{\frac{m_-\rho_- - 1}{2m_0}}\Lambda_{\mathrm{BL}}$. Here, we take into account the inhomogeneity of motors by distinguishing m_-, the motor concentration at the centre of the bilayer, and m_0, which we take to be the average of the motor field in the inside of the bilayer. As a reference density ρ_0 for the linearisation, we also took the average over the inside of the bilayer. Rewriting the equation for the length scale as we did in (3.39), we expect the data points to collapse on a different function for each value of $\hat{\kappa}$ when plotting $\tilde{\ell}_{\mathrm{BL}}$ against $\tilde{\Lambda}_{\mathrm{BL}}$. Indeed, this is

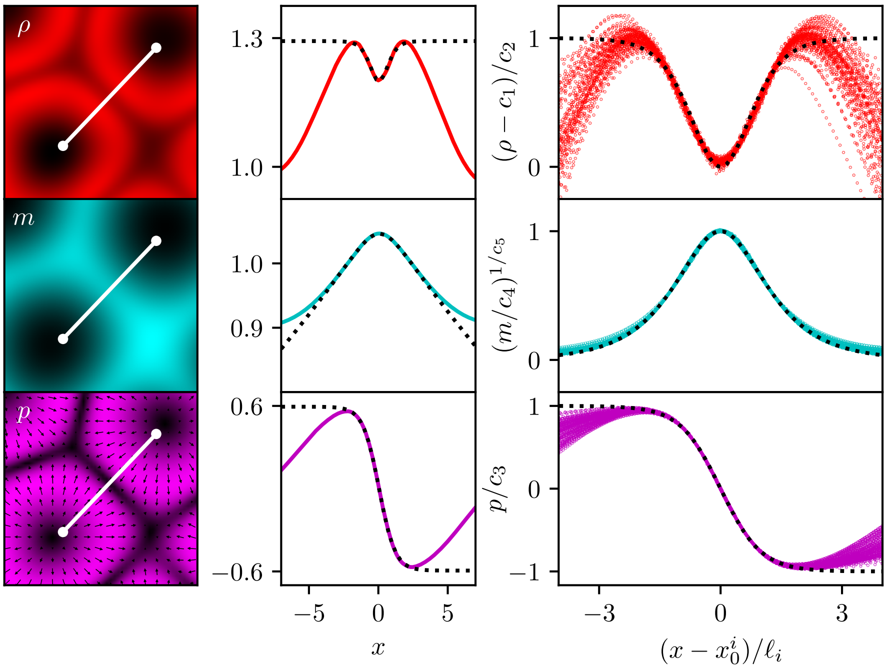

Figure 18: Simulations of the phenomenological model were performed for $\hat{\kappa}_1 \in \{0.08, 0.1, 0.12\}$, $\hat{\lambda}_2 \in \{-0.4, -0.5, -0.6\}$, $\hat{\zeta}_1 \in \{0.1, 0.2, 0.3\}$ and fixed $\bar{\rho} = 1.2$, $D_\rho = 1/32$, $\nu = 0.08$, $\alpha_2 = \alpha_3 = \hat{\kappa}_2 = \hat{\zeta}_2 = 0$, $\hat{\lambda}_1 = 0.5$, $v_m = 0.01$, $D_m = 0.2$ in a periodic box of size 80×80, for $t = 2000$. For each simulation, a bilayer cross section was measured and fitted using the functions (3.38). An example of the bilayer is shown on the left, where a detail of size 20×20 was cropped. The density, motor and polarisation profiles are plotted against the contour length x, and the fit is shown as a dotted line. On the right, the curve collapse obtained by plotting the rescaled functions $(\rho - c_1)/c_2$, p/c_3 and $(m/c_4)^{1/c_5}$ against $(x - x_0^i)/\ell_i$ is shown. The expected functions $\tanh^2(x)$, $\cosh(x)^{-1}$ and $-\tanh(x)$ are shown as black dots.

what we observe (top left plot in Fig. 19). Dividing eq. (3.39) by $\sqrt{\hat{\kappa}}$ on both sides, i.e. rescaling the axes by this quantity, the curves collapse onto a single curve (top right plot in Fig. 19).

A better quantitative agreement with the measured data can be achieved by choosing $m_0\rho_0 - 1$ instead of $m_-\rho_- - 1$ in the definition of the quantities with a tilde in eq. (3.39) The resulting curves are shown in the bottom plots of Fig. 19. This might be due to the fact that we had to linearise the density to obtain eq. (3.15).

3.4.2 Micelle profile

To find the micelle profile, we start by writing the equations (2.64) in polar coordinates. They are given in appendix A.4. We are looking for radially symmetric stationary solutions of these equations with inward-pointing polarisation. Hence, we discard angular dependences (∂_ϕ=0), and assume a radially oriented polarisation $\boldsymbol{p} = p\hat{\boldsymbol{e}}_r$, where $p < 0$.

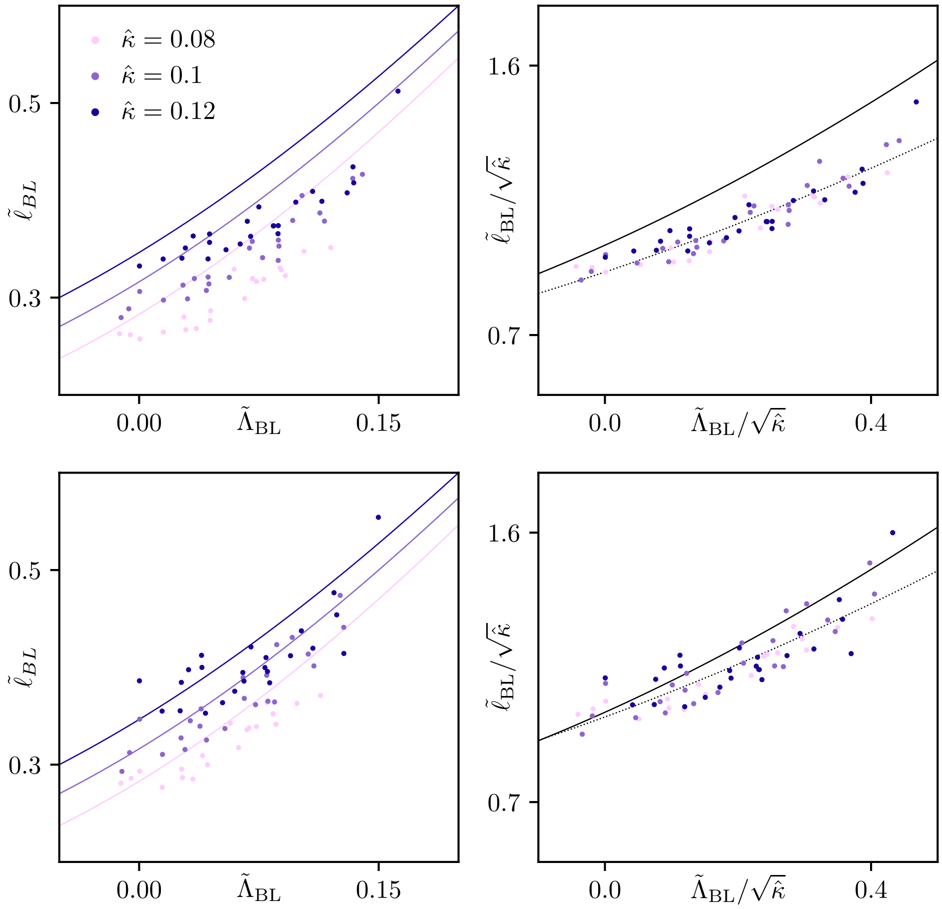

Figure 19: Curve collapse for the bilayer length scale predicted by eq. (3.39). The dots are the data points from the simulations listed in Fig. 18, and the solid lines show the theoretical predictions. For ℓ_{BL} and A, we used the fitted values ℓ_p and c_3 from eq. (3.38). On the left, we see data collapse on different curves for different values of $\hat{\kappa}$. On the right, rescaling the axes by $\sqrt{\hat{\kappa}}$, we see that all points collapse onto the same curve. The dotted curve shows a fit of the function $b_1 x + \sqrt{(b_1 x)^2 + b_2}$ with fit parameters b_i to the data. In the top row, we used $m_- \rho_-$ (with the values of the fields in the centre of the bilayer) in the definition of the quantities with a tilde; in the bottom row, we substituted this by $m_0 \rho_0$ (using the averaged fields), which gives better quantitative agreement with theory.

The resulting equations read:

$$\begin{aligned}\partial_t \rho &= r^{-1}\partial_r[r\partial_r(D_\rho \rho + m\nu\rho^2 + \alpha_2\rho^2 + \alpha_3\rho^3 + \chi p^2)] \\ &\quad + r^{-1}\partial_r[r\chi_1 p^2/r], \qquad (3.40\text{a}) \\ \partial_t p &= \left[(m\rho/\rho_c - 1) - \lambda_2 p/r - \beta m^2 p^2\right] p \\ &\quad + \kappa[\partial_r^2 p + \partial_r p/r - p/r^2] - \lambda p \partial_r p + \zeta_1 \partial_r \rho, \qquad (3.40\text{b}) \\ \partial_t m &= r^{-1}\partial_r[r(D_m \partial_r m - v_m m p)]. \qquad (3.40\text{c})\end{aligned}$$

Microtubule density profile

We proceed similarly to the analysis of the bilayer profile. The centre of the micelle fulfils the same conditions as the centre of the bilayer, i.e. it has $p(r = 0) = 0$ (for symmetry reasons), and is a minimum in ρ and a maximum in m. Assuming small γ, we set $m = m_0$ everywhere, and we linearise the microtubule density around a reference density ρ_0. Then, integrating equation (3.40a) twice, we find:

$$\rho(r) = \rho_- - \frac{\chi}{D_\text{eff}} p^2(r) - \frac{\chi_1}{D_\text{eff}} \int_0^r \mathrm{d}r' \, \frac{p^2(r')}{r'}. \qquad (3.41)$$

Comparing this to eq. (3.15), there is a new term proportional to χ_1 that enhances phase separation for $\chi_1 < 0$. This is due to the additional splay flux (see Fig. 16) emerging as a consequence of radial symmetry. Since the term is non-local, we cannot make predictions on the strength of phase separation as we did in (3.19).

Close to the bilayer, however, we can approximate the integral as follows. The Taylor expansion for p^2 reads:

$$\begin{aligned}p^2(r) &= p^2(r = 0) + 2[p\partial_r p]_{r=0} r + \left[(\partial_r p(r))^2 + p\partial_r^2 p\right]_{r=0} r^2 + \mathcal{O}(r^3) \\ &= C r^2 + \mathcal{O}(r^3), \qquad (3.42)\end{aligned}$$

where $C = [\partial_r p(r)]^2_{r=0}$. Plugging this into the integral from eq. (3.41) gives:

$$\int_0^r \mathrm{d}r' \, \frac{p^2(r')}{r'} \approx C \int_0^r \mathrm{d}r' \, r' = \frac{1}{2} C r^2 \approx \frac{p^2(r)}{2}. \qquad (3.43)$$

Thus, we can write:

$$\rho = \rho_- - \frac{\chi + \chi_1/2}{D_\text{eff}} p^2(r). \qquad (3.44)$$

Polarisation profile

Using this relation in (3.40b) and requiring stationarity, we find:

$$\begin{aligned}0 &= (m_0\rho_-/\rho_c - 1)p - \beta m_0^2(1 + \bar{\chi}_M)p^3 + \kappa\partial_r^2 p - \lambda_2 p^2/r - \bar{\lambda}_M p \partial_r p \\ &\quad + \kappa[\partial_r p/r - p/r^2], \qquad (3.45)\end{aligned}$$

where for brevity we've defined $\bar{\lambda}_M = \bar{\lambda} + \zeta_1\chi_1/D_\text{eff}$, as well as $\bar{\chi}_M = \bar{\chi} + \bar{\chi}_1/2$. These take into account the effect of the splay flux χ_1, that didn't play any role for the bilayer profile.

As before, we consider two limits of equation (3.45), in which either the $\bar{\lambda}_M$ term dominates, or the κ term does. The derivation is analogous to the bilayer case, except for the presence of new terms. In both cases, we will neglect the second line, which vanishes to linear order in r since we can Taylor expand $p(r) = \partial_r p|_{r=0}\, r$.

For $\bar{\lambda}_M$ large compared to the κ and λ_2 terms, we find, analogously to eq. (3.23):

$$p(r) = \begin{cases} -A\tanh(r/\ell_{\text{MIC}}) & \text{for} \quad (1+\bar{\chi}_M)(m_0\rho_- - \rho_c) > 0, \\ -A\tan(r/\ell_{\text{MIC}}) & \text{for} \quad (1+\bar{\chi}_M)(m_0\rho_- - \rho_c) < 0. \end{cases} \tag{3.46}$$

Unlike the bilayer case, due to the extra term in eq. (3.41), there is no condition like (3.19) that would pick out the tanh solution. Indeed, the signs of $1+\bar{\chi}_M$ and $m_0\rho_- - \rho_c$ don't have to match, even though phase separation is still controlled by the magnitude of $\bar{\chi}_M$. While the tanh solution saturates at $\pm A$, the tan solution diverges. Hence, it can only represent an approximation of the solution close to $x = 0$; the κ term and the other terms we have neglected will saturate the solution far from the centre.

A denotes the amplitude of the polarisation, and the length scale ℓ_{MIC} is given by:

$$\ell_{\text{MIC}} = \frac{-A\bar{\lambda}_M}{m_0\rho_-/\rho_c - 1}. \tag{3.47}$$

Comparing this to eq. (3.25), we see that a similar competition mechanism is at work to select the micelle length scale as for the bilayer in the strong $\bar{\lambda}$ limit, involving self-advection, anchoring and the Ginzburg-Landau ordering term. $\bar{\lambda}$ is modified to $\bar{\lambda}_M$, which takes into account that the density gradient the anchoring ζ_1 couples to acquires an additional contribution from the splay flux. $\bar{\lambda}_M < 0$ must hold to obtain a micelle with inward-pointing microtubules for $m_0\rho_- - \rho_c > 0$.

The effect of slowly activating the λ_2 term in (3.45), with κ still negligibly small, can be examined by assuming that the solution given in (3.47) maintains its shape, such that we can approximate $p(r) \approx -A\ell_{\text{MIC}}^{-1} r$. This results in a contribution to the linear term in (3.46):

$$-\lambda_2 \frac{p^2}{r} \approx \lambda_2 \frac{A}{\ell_{\text{MIC}}} p. \tag{3.48}$$

This term will enter the denominator of eq. (3.47). As before for the bilayer profile, we obtain an implicit relation for ℓ_{MIC}. It has the solution:

$$\ell_{\text{MIC}} = \frac{-A(\bar{\lambda}_M + \lambda_2)}{m_0\rho_-/\rho_c - 1}. \tag{3.49}$$

The active splay term λ_2 appears here because of the splay that naturally emerges in the micelle due to radial symmetry. For inward pointing polarisation, the splay is negative: thus, for $m_0\rho_-/\rho_c > 1$ and $\lambda_2 < 0$, the active splay suppresses the order in the centre of the micelle, thus leading to an increase of the length scale ℓ_{MIC}.

In the other limit, where κ dominates, the equation takes the form that we have already discussed for the bilayer. Likewise, we find a tanh-like kink solution if the centre of the micelle is above criticality, as in eq. (3.26):

$$p(r) = -A\tanh(r/\ell_{\text{MIC}}), \tag{3.50}$$

with the length scale:

$$\ell_{\rm MIC} = \sqrt{\frac{2\kappa}{m_0\rho_-/\rho_c - 1}}. \tag{3.51}$$

To take into account the other terms, we approximate $\partial_r p \approx -A/\ell_{\rm MIC}$ as well as $p \approx -A/\ell_{\rm MIC} r$. Then, the other terms in (3.45) give contributions to the linear term, such that we obtain:

$$\ell_{\rm MIC} = \Lambda_{\rm MIC} + \sqrt{\Lambda_{\rm MIC}^2 + \frac{2\kappa}{m_0\rho_-/\rho_c - 1}}, \tag{3.52}$$

with

$$\Lambda_{\rm MIC} = \frac{-A(\bar\lambda_M + \lambda_2)}{2(m_0\rho_-/\rho_c - 1)}. \tag{3.53}$$

This gives back eq. (3.49) for negligible elasticity.

In general, however, the slope at $r = 0$ will determine the shape of the solution. Analogously to what we found in eq. (3.33) for the bilayer, the sign of $m_0\rho_- - \rho_c$ implies the sign of the third derivative of the polarisation at the centre of the micelle.

Motor profile

The motor profile can be found analogously to (3.36). Here, we also take into account the possibility of a tan-like profile, such that close to the centre we find:

$$m(r) = \begin{cases} m_- \cosh(r/\ell_{\rm BL})^{-\gamma A \ell_{\rm MIC}} & \text{for} \quad p \sim \tanh, \\ m_- \cos(r/\ell_{\rm BL})^{\gamma A \ell_{\rm MIC}} & \text{for} \quad p \sim \tan. \end{cases} \tag{3.54}$$

Micelle profile: Summary

To wrap up the results above, we expect a tanh-like solution for the polarisation for the micelles in the strong $\bar\lambda_M$ limit for $\bar\lambda_M < 0$, $1 + \bar\chi_M > 0$ and $m_0\rho_- > 0$ (or when all these signs are reversed), as well as in the strong κ limit when the centre lies above criticality. The profiles then look like those pertaining to the bilayer (see eq. (3.37)), using r instead of x and $\ell_{\rm MIC}$ instead of $\ell_{\rm BL}$.

As for the bilayer, we expect a change in the sign of $\partial_x^3 p(x = 0)$ for $\kappa < 0$ when the centre of the profile lies below criticality, hinting at a change in the profile shape in proximity of the centre. In addition, this transition to a tan-like profile is expected for the strong $\bar\lambda_M$ limit as well, when the signs of $1 + \bar\chi_M$ and the Ginzburg-Landau term don't match. This is forbidden for the bilayer due to the condition (3.19).

The length scale $\ell_{\rm MIC}$ is selected by the competition between the following terms:

Pulls micelle apart (larger ℓ_{MIC})	**Pushes micelle together** (smaller ℓ_{MIC})
Elasticity $\kappa > 0$	Ginzburg-Landau ordering $m_0\rho_- - \rho_c > 0$
Anchoring to density gradients $-(\chi + \chi_1/2)\zeta_1 > 0$	Self-advection $\lambda > 0$
Contractile flux $\chi < 0$	Effective diffusion $D_{\mathrm{eff}} > 0$
Splay flux $\chi_1 < 0$	
Active splay $\lambda_2 < 0$	

Thus, in addition to the terms that play a role for the bilayer length scale ℓ_{BL}, we find a new contribution depending on the splay flux and the active splay. This is caused by the radial symmetry of the micelle, which naturally induces a splay deformation with negative sign in the polarisation field.

Measuring the micelles

As we did for the bilayer, we simulated a set of parameters in the regime of the phenomenological model where micelles appear to extract their profiles and length scales. We chose the parameters to lie in the strong $\bar{\lambda}_M$ regime, to verify the prediction on the tanh-to-tan transition in dependence on the strength of $\bar{\chi}_M$. To extract the radial profile of the micelles, we identified the local minima of the density field by a 2d peak detection algorithm for each simulation and discarded the density minima that did not correspond to micelle centres. Then, we extracted the 1d profile passing through the identified centres along an arbitrary axis, taking advantage of the micelles' radial symmetry.

For each micelle profile, we calculated the value of $\partial_x^3 p(x)$ at its centre. This derivative has a different sign for the two solutions in eq. (3.46), so it can be used to distinguish them. Figure 20 shows an example profile for each of the two profiles (tanh above and tan below), as well as the value of $\partial_x^3 p(x)|_{x=0}$ against $\bar{\chi}_M$ for the profiles whose centre lies above criticality. Indeed, as $|\bar{\chi}_M|$ crosses the threshold value of 1, we see that the third derivative changes its sign. This is in agreement with the prediction indicated in eq. (3.46).

For the micelles with $\partial_x^3 p(x)|_{x=0} > 0$, we proceeded like for the bilayer profiles, using the density maxima on each side of the centre to delimit the interior of the micelle and fitting the measured profiles using the functions indicated in eq. (3.38). Rescaling the profiles like we did for Fig. 18, we can then collapse them all onto one curve, shown in the left panel of Fig. 21. As for the length scale prediction, since we are in the strong $\bar{\lambda}_M$ regime, the length scale is given by eq. (3.49). The right panel of Fig. 21 shows that the theoretical prediction is in good agreement with the measured length scales.

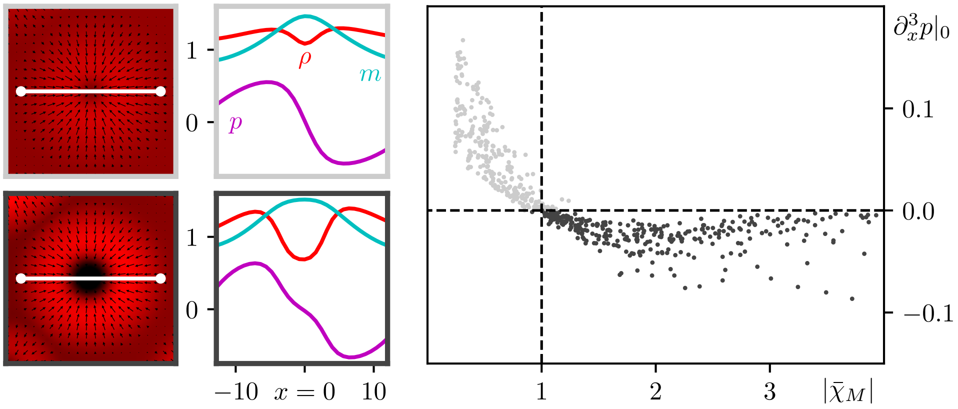

Figure 20: Simulations of the phenomenological model were performed for $\hat{\chi}_1 \in \{-0.15, -0.125, -0.1, -0.075\}$, $\hat{\chi}_2 \in \{0, 0.025, 0.05\}$, $\hat{\kappa}_1 \in \{0.05, 0.075, 0.1\}$, $\hat{\lambda}_2 \in \{-0.2, -0.4, -0.6\}$, and fixed $\bar{\rho} = 1.2$, $D_\rho = 1/32$, $\alpha_2 = \alpha_3 = -\nu = 0.05$, $\hat{\kappa}_2 = \hat{\zeta}_1 = 0$, $\hat{\lambda}_1 = -1.0$, $v_m = 0.02$, $D_m = 0.2$, in a periodic box of size 80×80, for $t = 600$. The micelle centres where identified by finding the minima of the density field with a 2d peak detection algorithm, and taking the cross section along an arbitrary axis passing through that point. The left panel shows two examples of observed profiles (ρ profile in red, m profile in cyan, p profile in magenta). The upper profile has $\partial_x^3 p|_{x=0} > 0$ (tanh-like profile, light grey), the lower one $\partial_x^3 p|_{x=0} < 0$ (tan-like profile, dark grey). In the right panel, the third derivative of the polarisation at the micelle centre is plotted against the value of $\bar{\chi}_M$ for all the profiles with centres above criticality, showing a tanh-to-tan transition as the critical value of $\bar{\chi}_M = 1$ is crossed.

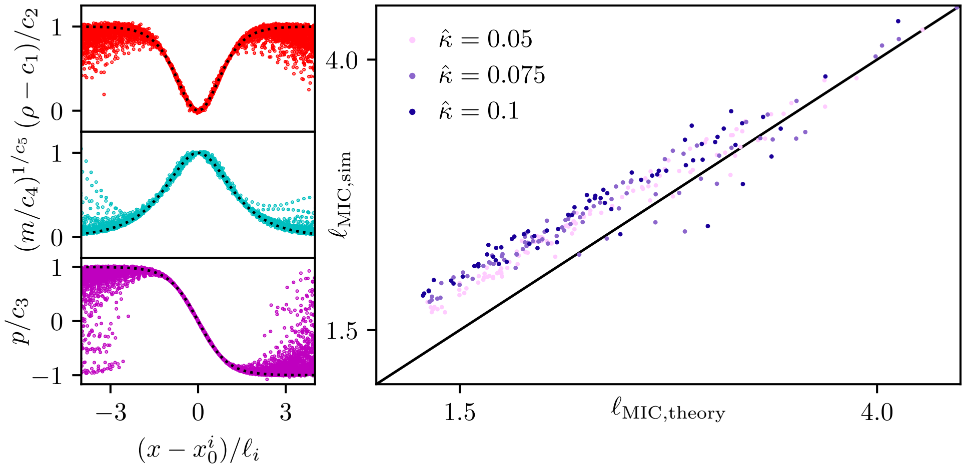

Figure 21: Left: Curve collapse obtained by plotting the rescaled data $(\rho - c_1)/c_2$, $(m/c_4)^{1/c_5}$ and p/c_3 against $(x - x_0^i)/\ell_i$ with the fit parameters from eq. (3.38) for the tanh-like profiles measured in the simulations indicated in Fig. 20. The expected functions $\tanh^2(x)$, $\cosh(x)^{-1}$ and $-\tanh(x)$ are shown as black dots. Right: the measured lengthscale $\ell_{\mathrm{MIC,sim}} = \ell_p$ is plotted against the theoretical prediction indicated in eq. (3.49), where we used c_3 from the fit (3.38) for A.

3.4.3 Length scales in the derived model

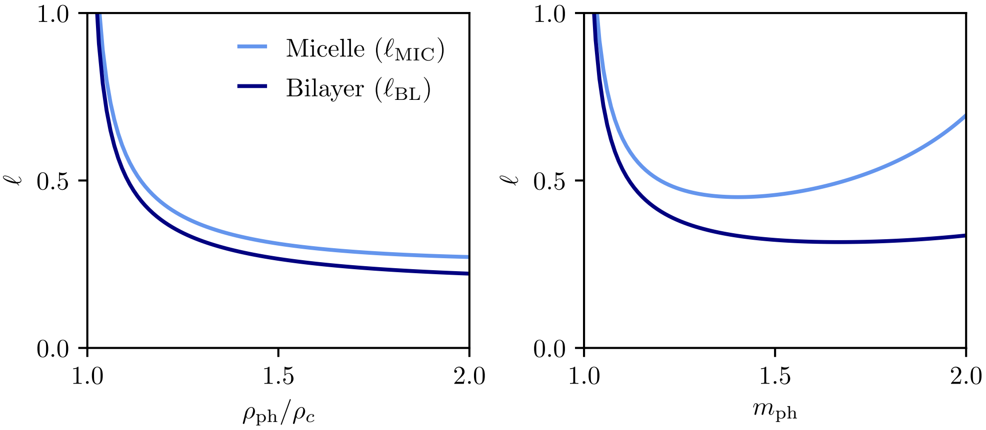

Figure 22: Dependence of the micelle and bilayer length scales on physical microtubule and motor densities in the derived model, for $\eta = 0.56$, $\omega_c = 2.18$, $\xi = 0$, $\alpha_{\mathrm{ph}} = 0.7$. We chose $\alpha = \alpha_{\mathrm{ph}}/m_{\mathrm{ph}}$ and $\rho = m_{\mathrm{ph}}\rho_{\mathrm{ph}}$, with $m_{\mathrm{ph}} = 1$ on the left and $\rho = \rho_c$ on the right. We see that all length scales decrease with increasing density close to the orientational transition. However, while they plateau for larger microtubule densities, the micelle length scale grows as the motor density is increased further.

We can use the results from this section to predict how the length scales change in dependence on microscopic parameters in the derived model. To this goal, we assume that the relation for the phase separation strength (3.20) is valid for the micelles as well, substituting $\bar{\chi}_M$ for $\bar{\chi}$. While such an assumption might not be correct in quantitative terms, we expect it to give the correct qualitative behaviour, since $\bar{\chi}_M$ drives density fluxes in a radially symmetric setting. In mathematical terms, this amounts to extending the approximation (3.44) to regions far from the centre. With this, we can use the expression for $\Delta\rho$ to obtain the densities $\rho_\pm$ at the maximum, and consequently the amplitude A of the polarisation via (3.24). Plugging this into equations (3.30) and (3.52), we find expressions for ℓ_{BL} and ℓ_{MIC} that depend on ρ_0 only.

Plotting the dependence of the bilayer and micelle length scales on the microtubule and motor densities (see Fig. 22), we find that both length scales decrease as the densities are increased close to criticality. This corresponds to our expectation from the Ginzburg-Landau scaling, where we had $\partial_x \sim p \sim \epsilon$, which means that we expect characteristic length scales to scale as $1/\sqrt{m_0\rho_0/\rho_c - 1}$ (see also (3.27)). However, while for high microtubule densities the length scales plateau at about a quarter of a microtubule length, the micelle length scale increases again at higher motor densities. This explains the opening up we saw in the numerical simulations for low values of α, see Fig. 14. A similar opening up of micelles for high motor concentrations was recently observed in agent-based simulations [32].

3.5 Linear stability analysis of homogenous states

Now that we have studied the stationary profiles of micelles and bilayers, our next goal is to inspect their stability. The tool to achieve this is linear stability analysis. In this section, we limit ourselves to the simplest states, the homogeneous ones. As we will see, the mechanisms involved will be relevant for bilayers and micelles as well.

3.5.1 LSA of the disordered state

We start by studying the instabilities of the isotropic ($p = 0$) homogeneous state. To this goal, we perform a linear stability analysis of equations (2.64) by introducing a periodic perturbation of the form:

$$\rho(x, y, t) = \rho_0 + \delta\rho(t)e^{ikx}, \tag{3.55a}$$

$$p_i(x, y, t) = \delta p_i(t)e^{ikx}, \tag{3.55b}$$

where we chose the coordinate system such that the x axis is aligned with the periodic modulation, without loss of generality. For small γ, the motor field won't contribute significantly to the onset of the instability and we can keep it constant, $m = m_0$.

Plugging (3.55) into equations (2.64), and keeping terms up to linear order in the perturbations, we obtain the equations:

$$\partial_t \delta\rho = -k^2 D_{\text{eff}} \delta\rho, \tag{3.56a}$$

$$\partial_t \delta p_x = (m_0\rho_0/\rho_c - 1)\delta p_x - \kappa k^2 \delta p_x + i\zeta_1 k \delta\rho, \tag{3.56b}$$

$$\partial_t \delta p_y = (m_0\rho_0/\rho_c - 1)\delta p_y - \kappa_1 k^2 \delta p_y, \tag{3.56c}$$

where D_{eff} was defined in equation (3.3). The resulting eigenvalues are:

$$\sigma_1 = -k^2 D_{\text{eff}}, \tag{3.57a}$$

$$\sigma_2 = (m_0\rho_0/\rho_c - 1) - \kappa k^2, \tag{3.57b}$$

$$\sigma_3 = (m_0\rho_0/\rho_c - 1) - \kappa_1 k^2. \tag{3.57c}$$

The first eigenvalue is positive for $|k| > 0$ and $D_{\text{eff}} < 0$, which can be the case only when $\nu < 0$. Then, a type II-s instability occurs (in the classification introduced in [33]). This instability has been discussed in [13] and [23] for the $\omega_c = \pi$ case, where it has been termed *density instability* because it occurs also when the perturbation is purely a density one, with $\delta p_{x,y} = 0$. To regularise the instability at short wavelengths, higher order gradient terms of the form $\nabla^4\rho$ must be introduced. However, as noted in [23], this can be avoided by choosing α large enough, such that $D_{\text{eff}} > 0$ and the instability does not occur. We will assume this in the following.

For $m_0\rho_0 > \rho_c$, i.e. above criticality, the two polarisation directions show a type III-s instability (in the nomenclature of [33]) with a maximum at $k = 0$, corresponding to the emergence of global order. While the system is stable with respect to short wavelength perturbations, perturbations with wavelengths longer than a critical wavelength ℓ_c trigger the emergence of global order.

3.5.2 LSA of the homogeneous ordered state

As we have seen, a Ginzburg-Landau transition occurs above criticality and the order parameter acquires a non-zero value globally. The simplest ordered state is the homogeneous one, where the microtubule and motor densities are constant, $\rho = \rho_0$ and $m = m_0$, and the order points in the same direction everywhere. The order amplitude is given by the stationarity condition in the polarisation equation, which in the absence of gradients amounts to balancing the linear and cubic terms in eq. (2.44), giving:

$$p_0 = \sqrt{\frac{m_0\rho_0 - \rho_c}{\beta m_0^2 \rho_c}}. \tag{3.58}$$

To understand under which conditions the homogeneous ordered state is unstable, we again perform a linear stability analysis of equations (2.64), by perturbing the state as follows:

$$\rho(x, y, t) = \rho_0 + \delta\rho(t) e^{i(k_x x + k_y y)}, \tag{3.59a}$$

$$p_i(x, y, t) = p_0 \delta_{i,x} + \delta p_i(t) e^{i(k_x x + k_y y)}. \tag{3.59b}$$

Here, we have chosen the x axis to lie along the global polarisation of the initial state. Thus, k_x and k_y set the length scales of the perturbation longitudinally and perpendicularly to the order, respectively. Moreover, the perturbations δp_x and δp_y can be identified with modulations respectively of the order strength and order direction.

By plugging this into (2.64), we find the equations:

$$\partial_t \delta\rho = -D_{\text{eff}} k^2 \delta\rho - 2(\chi_1 k_x k_j p_0 \delta p_j + \chi_2 k^2 p_0 \delta p_x), \tag{3.60a}$$

$$\begin{aligned}\partial_t \delta p_x = {} & m_0 p_0/\rho_c \delta\rho - 2\beta m_0^2 p_0^2 \delta p_x - \kappa_1 k^2 \delta p_x - \kappa_2 k_x k_j \delta p_j \\ & + i\zeta_1 k_x \delta\rho - i\lambda k_x p_0 \delta p_x - i\lambda_2 k_y p_0 \delta p_y,\end{aligned} \tag{3.60b}$$

$$\partial_t \delta p_y = -\kappa_1 k^2 \delta p_y - \kappa_2 k_y k_j \delta p_j + i\zeta_1 k_y \delta\rho + 2i\zeta_2 k_y p_0 \delta p_x - i\lambda_1 k_x p_0 \delta p_y, \tag{3.60c}$$

where summation over equal indices is implicit.

In the $\boldsymbol{k} \to 0$ (long wavelength) limit, only δp_x decays with a finite rate, as the system will bring the polarisation strength to the value imposed by the density via (3.58). Global changes in the density and orientation, on the other hand, are marginal as a consequence of density conservation and rotational invariance of the system, and have vanishing decay rate as $\boldsymbol{k} \to 0$. Therefore, we can perform an adiabatic elimination by setting $\partial_t \delta p_x = 0$, which gives us:

$$2\beta p_0 \delta p_x = \frac{\delta\rho}{m_0 \rho_c} - i\lambda_2/m_0^2 k_y \delta p_y. \tag{3.61}$$

Plugging this into equations (3.60) yields:

$$\partial_t \begin{pmatrix} \delta\rho \\ \delta p_y \end{pmatrix} = \begin{pmatrix} J_{11} & J_{12} \\ J_{21} & J_{22} \end{pmatrix} \begin{pmatrix} \delta\rho \\ \delta p_y \end{pmatrix}, \tag{3.62}$$

with the entries of the Jacobian reading as follows, to the lowest order we will need:

$$J_{11} = -D_{\text{eff}}(1+\bar{\chi}_2)k^2 - D_{\text{eff}}\bar{\chi}_1 k_x^2, \tag{3.63a}$$
$$J_{12} = -2\chi_1 p_0 k_x k_y + i\lambda_2\chi_2/(\beta m_0^2)k_y^3, \tag{3.63b}$$
$$J_{21} = i\bar{\zeta}k_y, \tag{3.63c}$$
$$J_{22} = -i\lambda_1 k_x p_0 + \lambda_2\zeta_2/(\beta m_0^2)k_y^2 - \kappa_1 k^2 - \kappa_2 k_y^2. \tag{3.63d}$$

Here, we've introduced $\bar{\zeta}$ as the effective total anchoring, taking into account the gradient in the order amplitude induced by a density variation:

$$\bar{\zeta} = \zeta_1 + \frac{\zeta_2}{\beta m_0 \rho_c}. \tag{3.64}$$

The eigenvalues of the Jacobian (3.63) are given by:

$$2\sigma_\pm = \operatorname{Tr} J \pm \sqrt{(\operatorname{Tr} J)^2 - 4\det J}. \tag{3.65}$$

The system in unstable when at least one of these eigenvalues acquires a positive real part. Below, we will see how this translates to conditions on the equation coefficients. We will have to treat different perturbation directions separately: we write $\boldsymbol{k} = (k\cos\varphi, k\sin\varphi)$, with φ signifying the angle between the wave vector and the order direction.

Longitudinal instability

For a purely longitudinal perturbation with $k_y = 0$, the orientational perturbation δp_y completely decouples from the density and order strength perturbations, as can be seen in (3.60). The two eigenvalues are then given by the diagonal entries of the Jacobian (3.63).

A perturbation which purely involves the density (and, consequently, the order strength, via (3.61)) will have the eigenvalue:

$$\sigma_1 = -D_{\text{eff}}(1+\bar{\chi})k_x^2, \tag{3.66}$$

which is real to lowest order in k. It becomes positive for $1+\bar{\chi} < 0$, i.e. when the contractile flux overcomes effective diffusion. This leads to fluxes along the order direction, amplifying the initial perturbation. Since the eigenvalue is 0 at $k = 0$, this is a type II-s instability.

On the other hand, the eigenvalue for the orientational perturbation reads $-\kappa_1 k_x^2 - i\lambda_1 k_x p_0$. It has positive real value for $\kappa_1 < 0$. Like for the density instability of the isotropic state, in order to regularise this instability for short wavelengths a bilaplacian of the form $\nabla^4\boldsymbol{p}$ would be required in the polarisation equation; in the following, we will therefore assume we are in the regime where $\kappa_1 > 0$.

Perpendicular instability

For a modulation which is purely perpendicular to the order, with $\varphi = \pm\pi/2$ and $k_x = 0$, the trace and the determinant of the Jacobian (3.63) become real to lowest order in k.

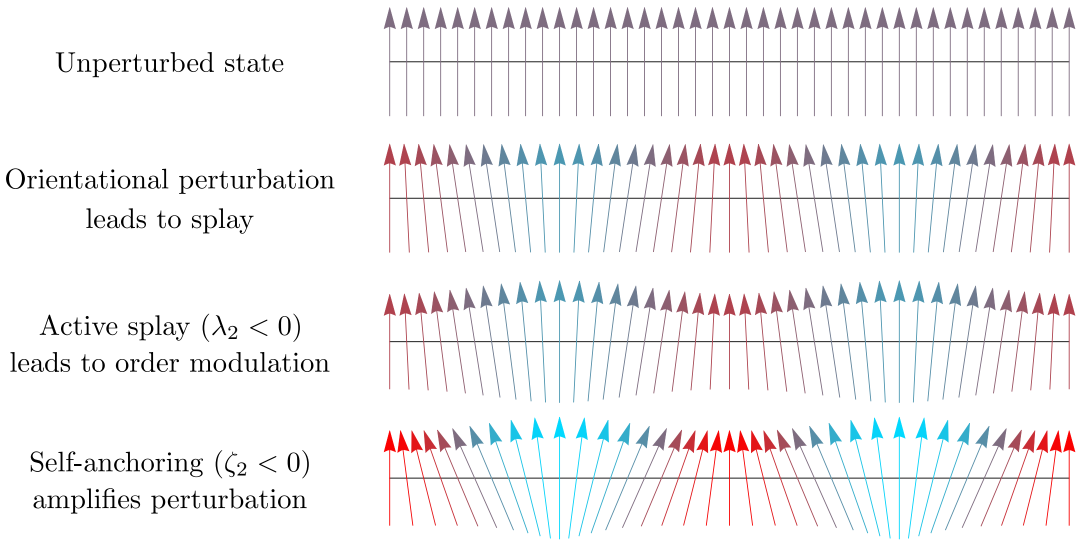

Figure 23: Feedback mechanism between active splay and self-anchoring for the perpendicular instability. As the orientation in an initial configuration is perturbed perpendicularly to the order, regions of positive (blue) and negative (red) splay emerge. For $\lambda_2 < 0$, the active splay increases the order in the blue regions and decreases it in the red regions. The self-anchoring $\zeta_2 < 0$ then rotates the orientation away from the regions with stronger order, resulting in even stronger splay.

Then, equation (3.65) gives at least one positive eigenvalue if $\operatorname{Tr} J > 0$ or if $\det J < 0$. The first condition gives the inequality:

$$\beta m_0^2[D_{\text{eff}}(1+\bar{\chi}_2)+\kappa] < \lambda_2\zeta_2, \tag{3.67a}$$

while the second condition results in the inequality:

$$\beta m_0^2(1+\bar{\chi}_2)\kappa < \lambda_2(\zeta_2 - \chi_2\zeta_1/D_{\text{eff}}). \tag{3.67b}$$

When either of these inequalities is fulfilled, we obtain a type II-s instability. The instability is mainly of orientational character, as can be seen by inspecting the eigenvectors corresponding to the eigenvalues $\sigma_\pm$ given in (3.65). These can be written as:

$$\boldsymbol{v}_\pm = \begin{pmatrix} \sigma_\pm - J_{22} \\ J_{21} \end{pmatrix}. \tag{3.68}$$

When $k_x = 0$, the eigenvalue is of order $\mathcal{O}(k^2)$, as is the component J_{22} of the Jacobian (3.63). On the other hand, for $\bar{\zeta} \neq 0$, the component J_{21} is of order $\mathcal{O}(k)$: hence, both eigenvectors have a predominant δp_y component, and the two perpendicular instabilities are mainly orientational. This means that the dynamics of the instabilities will be dominated by the perturbation of the order direction.

This knowledge allows us to interpret the instability conditions (3.67). The right hand side of those inequalities can be read as a feedback mechanism between the active splay term λ_2 and the anchoring terms $\zeta_{1,2}$. Indeed, as the orientational order in the homogeneous state is perturbed transversely, regions of positive and negative splay will emerge. The term λ_2 will enhance or suppress the amplitude of the order depending on the sign of the splay. The self-anchoring ζ_2 will then rotate the orientational order towards or away from these regions, thus amplifying the perturbation for $\operatorname{sgn}\zeta_2 = \operatorname{sgn}\lambda_2$, or bringing the system back to the homogeneous state when the two terms have opposite signs. This feedback mechanism is illustrated in Fig. 23 for $\lambda_2 < 0$ and $\zeta_2 < 0$; the case where the signs are reversed works analogously. On the left hand side of the inequalities, working against the instability, we find the elasticity κ, which penalises splay deformations. We also find the total transversal diffusivity $D_{\text{eff}}(1 + \bar{\chi}_2)$, which evens out gradients in density and order strength (the two are connected via eq. (3.61)).

The other term on the right hand side of eq. (3.67b) stems from the coupling to the density equation. Due to the modulation of the order strength (see Fig. 23), a transversal flux emerges, which is controlled by χ_2 (see Fig 16). This leads to inhomogeneities in the density field, which the density anchoring ζ_1 couples to, rotating the orientation towards or against high-density regions, depending on its sign. For the right combination of signs, this contributes positively to the feedback discussed above: for example, for $\lambda_2 < 0$, $\chi_2 < 0$ will accumulate density in the positive splay regions, and $\zeta_1 < 0$ will turn the orientation away from these regions, amplifying the splay.

Mixed instabilities

We are left to consider perturbations which are neither purely perpendicular nor purely longitudinal with respect to the order, i.e. $k_x \neq 0 \neq k_y$. Since we mix these two components, we'll refer to the emerging instabilities as mixed instabilities. Assuming $\lambda_1 \neq 0$, the expression in the square root of eq. (3.65) (i.e. the discriminant) reads as follows, up to third order in k:

$$-\lambda_1^2 k_x^2 p_0^2 \left(1 + \frac{2i}{\lambda_1 k_x p_0}(X k_x^2 + Y k_y^2)\right). \tag{3.69}$$

with

$$X = D_{\text{eff}}(1 + \bar{\chi}) - \kappa_1, \tag{3.70a}$$

$$Y = D_{\text{eff}}(1 + \bar{\chi}_2) + 4\frac{\chi_1 \bar{\zeta}}{\lambda_1} + \frac{\lambda_2 \zeta_2}{\beta m_0^2} - \kappa. \tag{3.70b}$$

In the long wavelength limit $k \to 0$, the term $k_y^2/k_x = k \sin\varphi \tan\varphi$ is much smaller than 1 as long as $|\tan\varphi| \ll k^{-1}$. If that is the case, taking the square root of (3.69), we can use $\sqrt{1+x} = 1 + \frac{x}{2} + \mathcal{O}(x^2)$ to obtain:

$$i|\lambda_1 k_x| p_0 - \operatorname{sgn}(\lambda_1 k_x) \left[X k_x^2 + Y k_y^2\right] + \mathcal{O}(k^3). \tag{3.71}$$

Plugging this result back into equation (3.65), and absorbing $\operatorname{sgn}(\lambda_1 k_x)$ into ±, we find the real parts of the two eigenvalues to be (up to second order in k):

$$\operatorname{Re}\sigma_+ = -D_{\text{eff}}(1 + \bar{\chi}) k_x^2 - \left[2\chi_1 \bar{\zeta}/\lambda_1 + D_{\text{eff}}(1 + \bar{\chi}_2)\right] k_y^2, \tag{3.72a}$$

$$\operatorname{Re}\sigma_- = -\kappa_1 k_x^2 + \left[\frac{\lambda_2 \zeta_2}{\beta m_0^2} + 2\chi_1 \bar{\zeta}/\lambda_1 - \kappa\right] k_y^2. \tag{3.72b}$$

When at least one of these expressions is positive, the homogeneous state is unstable. The imaginary parts read:

$$\operatorname{Im}\sigma_+ = 0 + \mathcal{O}(k^3), \tag{3.73a}$$

$$\operatorname{Im}\sigma_- = -\lambda_1 p_0 k_x + \mathcal{O}(k^3). \tag{3.73b}$$

The eigenvectors for the two eigenvalues can be written as:

$$\boldsymbol{v}_+ = \begin{pmatrix} J_{12} \\ \sigma_+ - J_{11} \end{pmatrix} = \begin{pmatrix} -2\chi_1 p_0 k_x k_y + i\lambda_2\chi_2/(\beta m_0^2)k_y^3 \\ -2\chi_1\bar{\zeta}/\lambda_1 k_y^2 \end{pmatrix}, \tag{3.74a}$$

$$\boldsymbol{v}_- = \begin{pmatrix} \sigma_- - J_{22} \\ J_{21} \end{pmatrix} = \begin{pmatrix} 2\chi_1\bar{\zeta}/\lambda_1 k_y^2 \\ i\bar{\zeta} k_y \end{pmatrix}. \tag{3.74b}$$

Thus, while σ_- indicates a predominantly orientational perturbation in the long wavelength limit, the ratio between the density ($\delta\rho$) and orientational (δp_y) components in $\boldsymbol{v}_+$ reads $\lambda_1/\bar{\zeta} p_0 \cot\varphi$, and thus the instability goes from predominantly density-like to predominantly orientational as φ is tuned from 0 to $\pi/2$.

For $k_y = 0$, we recover the eigenvalues discussed above for the longitudinal case, where σ_+ belonged to a pure density perturbation and σ_- to a purely orientational one. Assuming that the longitudinal instabilities are not activated, the k_x^2 terms stabilise the system. Hence, to identify new instability conditions, the $k_x \to 0$ limit is of interest. This corresponds to a perpendicular perturbation with a weak longitudinal component. However, we must be careful, since we assumed $|\tan\varphi| \ll k^{-1}$. We must therefore take the limit $\varphi \to \pi/2$ after the limit $k \to 0$.

For this choice of the wave vector, the k_y^2 terms in (3.72) dominate. Hence, (3.72a) becomes positive for:

$$-2\frac{\bar{\zeta}\chi_1}{\lambda_1} > D_{\text{eff}}(1 + \bar{\chi}_2). \tag{3.75}$$

This inequality has an interpretation in terms of a feedback loop between the density and polarisation fields, illustrated in Fig. 24, which involves the effective anchoring term $\bar{\zeta}$, the orientational self-advection λ_1 as well as the splay and bend fluxes proportional to χ_1. These fluxes compete with the total transverse flux given by $D_{\text{eff}}(1 + \bar{\chi}_2)$, which stabilises the homogeneous state; for a finite longitudinal component, as is evident from eq. (3.72a), the total longitudinal flux $D_{\text{eff}}(1 + \bar{\chi})$ also works against the destabilising feedback. Since for sufficient longitudinal admixture this instability becomes predominantly density-like, we refer to it as the *mixed density instability*, which is a type II-s instability.

On the other hand, the second eigenvalue (3.72b) is positive for:

$$\frac{\lambda_2\zeta_2}{\beta m_0^2} + 2\frac{\bar{\zeta}\chi_1}{\lambda_1} > \kappa. \tag{3.76}$$

This shows the same feedback between active splay λ_2 and self-anchoring ζ_2 discussed for the perpendicular instability, which is contrasted by the elasticity κ, see eq. (3.67). Here, there is an additional term coming from the longitudinal component, which again can be interpreted as a feedback loop, shown in Fig. 25. Note that this term has opposite sign compared to eq. (3.75), as the feedback operates in the opposite way. We refer to this instability as the *mixed orientational instability*, which is a type II-o instability.

Finally, the case $\lambda_1 = 0$ is special, since the second order term in k in (3.69) vanishes. In this case, the leading order term in (3.65) is given by:

$$2\sigma_\pm = \pm\sqrt{-8i\bar{\zeta}\chi_1 p_0 k_x k_y^2}. \tag{3.77}$$

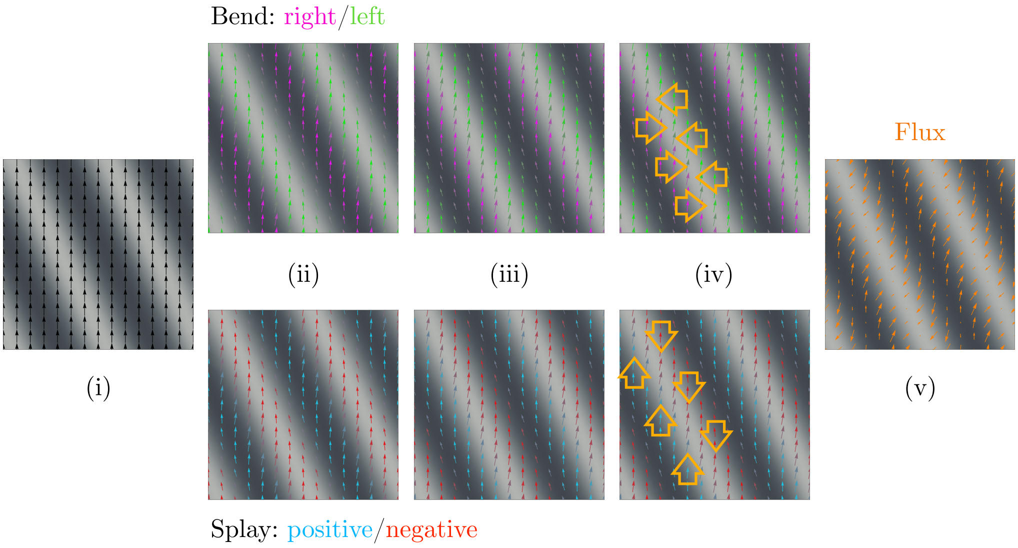

Figure 24: Feedback mechanism leading to the mixed density instability. (i) Initial periodic perturbation in the density (and order strength) with both perpendicular and longitudinal components. Bright regions have higher density than dark regions. (ii) Due to the effective anchoring, chosen here as $\bar{\zeta} > 0$, the orientation aligns itself along the density gradients. This results in a bend deformation, with some parts of the orientational field bending to the right (magenta) and others to the left (green), as well as a splay deformation, with positive (blue) and negative (red) splay regions. (iii) The orientational self-advection ($\lambda_1 > 0$) shifts the orientational distortion pattern along the order. (iv) The splay and bend distortions give rise to fluxes. For $\chi_1 < 0$, the bend flux (shown above) points to the inside of the osculating circle of the polarisation streamlines, i.e. to the right for a right-turning bend and to the left for a left-turning bend. Likewise, the splay flux (shown below) will point along the orientational vector for positive splay and against it for negative splay. (v) Flux field resulting from the sum of the splay and bend fluxes. This leads to further accumulation of density in the higher density regions for the right set of signs, i.e. $\mathrm{sgn}(\lambda_1 \chi_1 \bar{\zeta}) = -1$.

Taking the real part, we find:

$$\mathrm{Re}\, \sigma_\pm = \pm |k_y| \sqrt{|\chi_1 p_0 \bar{\zeta} k_x|}. \tag{3.78}$$

Thus, for $\lambda_1 = 0$ the homogeneous state is always unstable with respect to mixed perturbations.

3.5.3 Instabilities in the derived model

Using our results from the linear stability analysis, we can now inspect where the instabilities we have discussed appear in the derived model. To this goal, in Fig. 26 we plot the inequalities we have derived, i.e. $1 + \bar{\chi} < 0$ for the longitudinal (contractile) instability, the conditions (3.67) for the perpendicular instability, and (3.75) and (3.76) for the mixed instabilities, in dependence on the microscopic parameters.

As becomes apparent from panels a) and b) of that figure, the orientational instabilities – i.e. the perpendicular one and the mixed orientational one – appear for high densities for sufficiently high η and sufficiently low ω_c. This shows a striking similarity to the regime

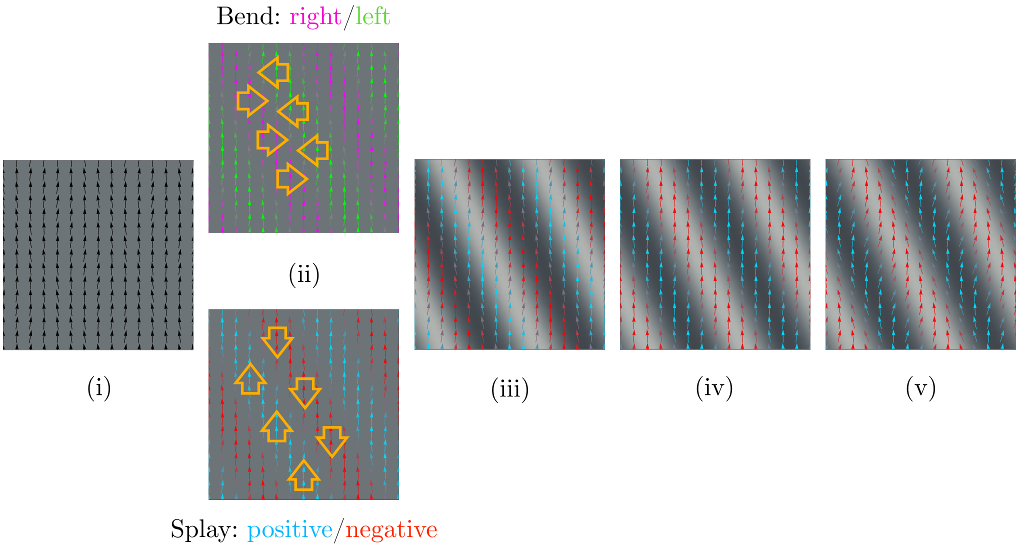

Figure 25: Feedback mechanism leading to the mixed orientational instability, that adds to the self-anchoring/active splay feedback discussed in Fig. 23. (i) Initial periodic perturbation in the orientation of the polarisation field with both perpendicular and longitudinal components. (ii) The orientational deformations lead to the emergence of splay and bend fluxes, shown here for $\chi_1 < 0$ as orange arrows, cfr. Fig. 24iv. (iii) The fluxes result in density inhomogeneities. (iv) The orientational pattern is advected backwards for $\lambda_1 < 0$. (v) Via the anchoring term $\bar{\zeta}$, the orientational field couples to the density gradients, leading to an amplified perturbation for $\mathrm{sgn}(\lambda_1 \chi_1 \bar{\zeta}) = +1$.

where micelles undergo branching and form active foams in the numerical simulations of the derived model. Indeed, Fig. 8 and Fig. 26a show the same structure. Furthermore, as we discussed in Fig. 11, active foams and branching micelles give way to stable micelles as one increases the critical angle ω_c, favouring polar interactions more strongly. Likewise, the orientational instabilities vanish as one increases ω_c in Fig. 26b.

As for the density instabilities, i.e. the mixed density instability and the contractile instability, they appear for low density values with a weak dependence on η and ω_c. However, they strongly depend on α: as shown in Fig. 26c, they regimes where they occur grow larger when α is decreased. Recalling the results from sec. 3.1.4, decreasing α also leads to the shape instability we saw for micelles in Fig. 15.

Thus, the instabilities of the homogeneous model seem to be related to micellular instabilities. We will inspect this connection more deeply in the next section.

At the bottom of Fig. 26, we show the dispersion relations for the four instabilities appearing in panel c), calculating the eigenvalues of the full three-dimensional Jacobian matrix (3.60) numerically. We find the instabilities we predicted making use of the adiabatic elimination of the order strength and the long-wavelength limit to appear also in the full problem. Furthermore, we confirm our results on the imaginary part of the eigenvalues: while the imaginary part of the density instabilities is of higher order in k, it is linear in k for the mixed orientational instability (compare eq. (3.73)). The perpendicular instability, on the other hand, exhibits a real eigenvalue as long as the radicand in (3.65) is positive, so that the imaginary part of the instability vanishes.

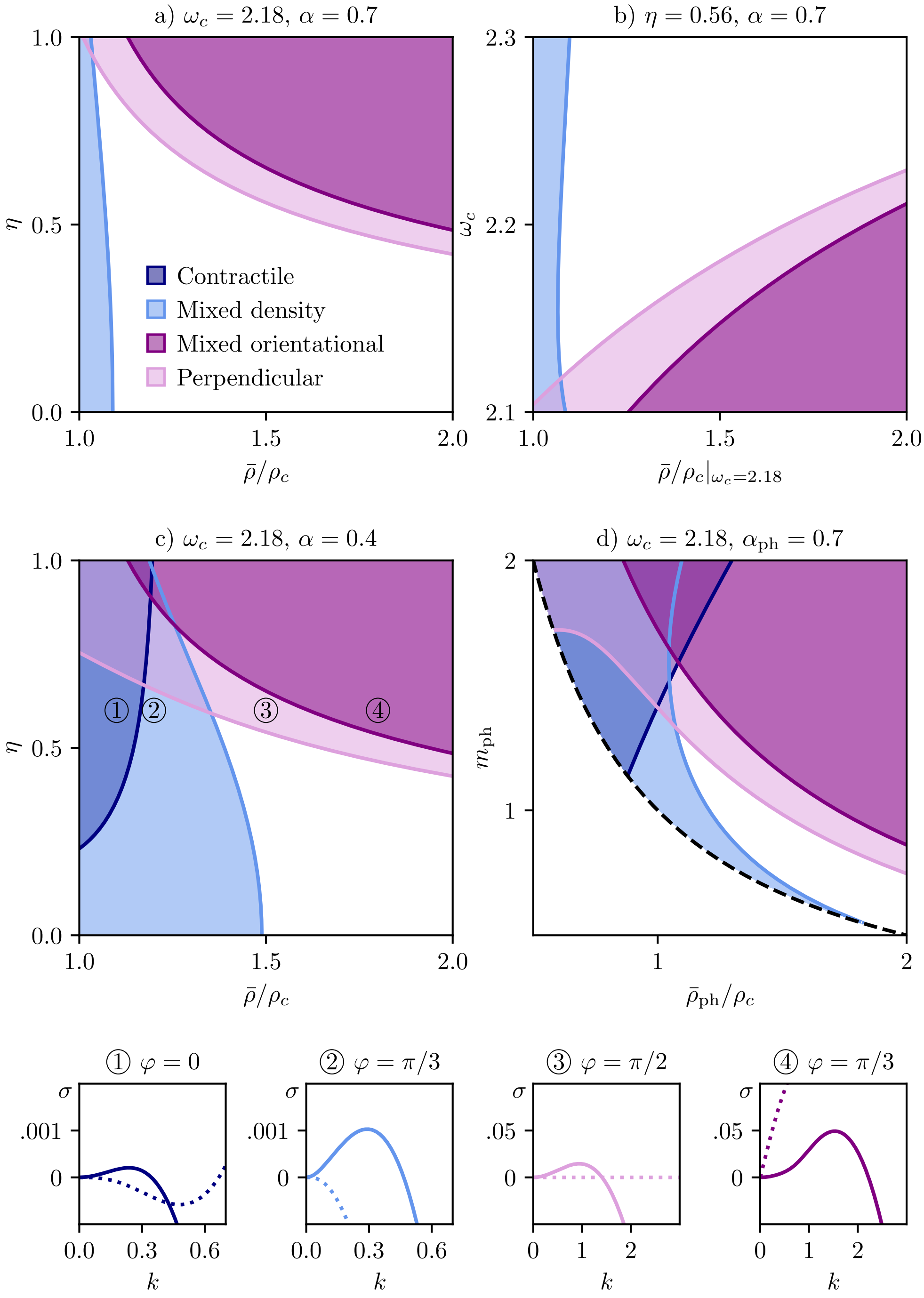

Figure 26: Regions where the various instabilities of the homogeneous state are activated in the derived model for $\xi = 0$. a) For sufficiently low ω_c, the orientational instabilities (mixed and perpendicular) are activated for high values of η. The mixed density instability is found at low densities. b) The orientational instabilities vanish at higher values of ω_c. c) For lower values of α, the regime where density instabilities (mixed and contractile) are found becomes larger. Dispersion relations obtained numerically from the full three-dimensional Jacobian (3.60) for various points in the phase diagram are shown below. Solid lines represent the real part of the dominant eigenvalue and dashed lines the imaginary part. d) Instability regimes in dependence on physical concentrations, with $\bar{\rho} = m_{\mathrm{ph}}\bar{\rho}_{\mathrm{ph}}$ and $\alpha = \alpha_{\mathrm{ph}}/m_{\mathrm{ph}}$.

In Fig. 26d), we plot the instabilites at fixed η, ω_c and α_{ph} for varying physical microtubule and motor densities. We see that all four instabilities can be activated. Thus, in a physical system, where the interaction parameters are fixed, we expect there to be distinct regimes where different instabilities are relevant. This can happen on a local scale, since the concentrations can vary throughout the system.

3.6 Micelle instabilities

3.6.1 LSA of radially symmetric solutions

In this section, we want to understand how the results we have obtained for the homogeneous state can be transferred to micelle solutions. We expect that the instabilities will be activated in the high-density ordered part of the micelle, where the density and polarisation plateaus are relatively flat. Hence, we will focus on a range of radii within this density plateau. We inspect the limit where the micelles are much larger than the length of a microtubule, i.e. their radius obeys $r \gg 1$.

We start by taking a radially symmetric stationary solution of the equations (3.40), i.e. a micelle profile with density $\rho_0(r)$ and polarisation $p_0(r)\hat{\boldsymbol{e}}_r$, and applying a periodic perturbation as follows:

$$\rho(r,\phi,t) = \rho_0(r) + \delta\rho(t)e^{in\phi}e^{ik_r r}, \tag{3.79a}$$

$$\boldsymbol{p}(r,\phi,t) = (p_0(r) + \delta p_r(t)e^{in\phi}e^{ik_r r})\hat{\boldsymbol{e}}_r + \delta p_\phi(t)e^{in\phi}e^{ik_r r}\hat{\boldsymbol{e}}_\phi. \tag{3.79b}$$

Hence, k_r is the wave vector of the radial perturbation and n the mode number of the perturbation along the ring. We assume k_r to be of order $\mathcal{O}(1/r)$, i.e. the length scale of the perturbation to be comparable with the radius of the micelle. On the other hand, n is an integer number, which is not small.

The radial function $p_0(r)$ is a stationary solution of eq. (3.40b). Keeping terms up to order $\mathcal{O}(r^{-2})$ in that equation, as well as neglecting radial derivatives, yields:

$$0 = m_0\rho_0/\rho_c - 1 - m_0^2\beta p_0^2 - \lambda_2 p_0/r. \tag{3.80}$$

Taking the radial derivative of this expression gives:

$$0 = m_0\partial_r\rho_0/\rho_c - 2m_0^2\beta p_0\partial_r p_0 - \lambda_2(\partial_r p_0/r - p_0/r^2).$$

Solving for $\partial_r p_0$ shows that radial derivatives are of order $\mathcal{O}(r^{-2})$, so that removing them in equation (3.80) is the consistent choice to make in a large r expansion up to order $\mathcal{O}(r^{-2})$.

Plugging the perturbation above into the dynamic equations of the model in polar coordinates (given in app. A.4), using the condition (3.80), and keeping terms to lowest order in

$1/r$ for each power of n, we find:

$$\begin{aligned}
\partial_t \delta\rho &= -\frac{n^2}{r^2} D_{\text{eff}} \delta\rho - 2\frac{n^2\chi_2 - in\chi_1}{r^2} p_0 \delta p_r \\
&\quad + \left[\frac{ik_r}{r} - k_r^2\right] D_{\text{eff}} \delta\rho + 2\chi \left[\frac{2ik_r}{r} - k_r^2\right] p_0 \delta p_r - 2\chi_1 \frac{p_0 n k_r}{r} \delta p_\phi, \qquad (3.81a) \\
\partial_t \delta p_r &= m_0 p_0/\rho_c \delta\rho - 2\beta m_0^2 p_0^2 \delta p_r - in\frac{\lambda_2 p_0}{r} \delta p_\phi, \qquad (3.81b) \\
\partial_t \delta p_\phi &= -\left[\frac{n^2\kappa}{r^2} + \frac{\lambda_1 p_0}{r}\right] \delta p_\phi + in\zeta_1 r \delta\rho + in\frac{2\zeta_2 p_0}{r} \delta p_r - ik_r \lambda_1 p_0 \delta p_\phi. \qquad (3.81c)
\end{aligned}$$

Firstly, we note that for $n = k_r = 0$ the δp_ϕ equation decouples, and it shows an instability for $\lambda_1 p_0 < 0$. This is a consequence of the radial orientation of the polarisation, as emerges from the following argumentation. The coefficient λ_1 controls the self-advection of the order orientation. In a perfectly radial configuration, the order orientation does not change along the order, and thus the self-advection has no effect. In contrast, when the orientation is perturbed, the order acquires an angular component, and the splayed configuration of the polarisation becomes of relevance for the self-advection. A negative λ_1 leads to a backward propagation of the perturbation along the ring, bringing back the system to its original state. In contrast, a positive λ_1 leads to a forward propagation of the perturbation, which consequently self-amplifies. This means that for $\lambda_1 > 0$ no inward-pointing micelles can exist, since they are unstable to orientational perturbations.

Adiabatically eliminating δp_r as we did in the linear stability analysis of the homogeneous state, we can reduce the dynamics of the perturbations to a two-dimensional Jacobian:

$$\partial_t \begin{pmatrix} \delta\rho \\ \delta p_\phi \end{pmatrix} = \begin{pmatrix} J_{11} & J_{12} \\ J_{21} & J_{22} \end{pmatrix} \begin{pmatrix} \delta\rho \\ \delta p_\phi \end{pmatrix}, \qquad (3.82)$$

with the entries of the Jacobian reading as follows, to the lowest order we will need:

$$\begin{aligned}
J_{11} &= \left(\frac{-n^2(1+\bar{\chi}_2) + in\bar{\chi}_1}{r^2} + \frac{ik_r(1+2\bar{\chi})}{r} - k_r^2(1+\bar{\chi}) \right) D_{\text{eff}}, \qquad (3.83a) \\
J_{12} &= -\frac{2p_0\chi_1 n k_r}{r}, \qquad (3.83b) \\
J_{21} &= i\bar{\zeta}\frac{n}{r}, \qquad (3.83c) \\
J_{22} &= -\lambda_1 \left(ik_r + r^{-1}\right) p_0 - \frac{n^2\kappa}{r^2} + \frac{\lambda_2\zeta_2}{\beta m_0^2}\frac{n^2}{r^2}. \qquad (3.83d)
\end{aligned}$$

To identify the unstable eigenvalues of this matrix, we make use of (3.65) again. The lowest order term in r^{-1} inside the square root of that equation reads:

$$\lambda_1^2 p_0^2 (ik_r + r^{-1})^2. \qquad (3.84)$$

Note that, in contrast to the corresponding expression (3.69) in the linear stability analysis of the homogeneous state, this does not vanish for $k_r = 0$. The next order term is given by:

$$-2\lambda_1 p_0 \left(ik_r + r^{-1}\right) \left[-\frac{n^2\kappa}{r^2} + \frac{\lambda_2\zeta_2}{\beta m_0^2}\frac{n^2}{r^2} - J_{11}\right] + 8i\frac{n^2 k_r}{r^2} p_0 \chi_1 \bar{\zeta}. \qquad (3.85)$$

Factoring out $\lambda_1^2 p_0^2 (ik_r + r^{-1})^2$, we can use $\sqrt{1+x} \approx 1 + x/2$. The square root term then reads:

$$\pm \left(\lambda_1 p_0 (ik_r + r^{-1}) + \frac{n^2 \kappa}{r^2} - \frac{\lambda_2 \zeta_2}{\beta m_0^2} \frac{n^2}{r^2} + J_{11} + 4i \frac{\chi_1 \bar{\zeta}}{\lambda_1} \frac{n^2 k_r}{r^2 \, (ik_r + r^{-1})} \right) \tag{3.86}$$

Putting everything together, we find the real parts of the eigenvalues:

$$\operatorname{Re} \sigma_+ = - \left(\frac{n^2 (1 + \bar{\chi}_2)}{r^2} + k_r^2 (1 + \bar{\chi}) \right) D_{\text{eff}} + 2 \frac{\chi_1 \bar{\zeta}}{\lambda_1} \frac{n^2 k_r^2}{r^2 \, (k_r^2 + r^{-2})}, \tag{3.87a}$$

$$\operatorname{Re} \sigma_- = - \frac{\lambda_1 p_0}{r} - \frac{n^2 \kappa}{r^2} + \frac{\lambda_2 \zeta_2}{\beta m_0^2} \frac{n^2}{r^2} - 2 \frac{\chi_1 \bar{\zeta}}{\lambda_1} \frac{n^2 k_r^2}{r^2 \, (k_r^2 + r^{-2})}. \tag{3.87b}$$

In the limit where the radial perturbation occurs on a length scale which is much shorter than the radius of the micelle, $\frac{k_r^2}{(k_r^2 + r^{-2})} \to 1$ and we recover the mixed instabilities of the homogeneous solution, (3.72), up to the additional λ_1 / r term, which stabilises orientational instabilities for small node numbers n, turning the mixed orientational instability into a type I instability.

For completeness, the imaginary parts read:

$$\operatorname{Im} \sigma_+ = \left(\frac{n \bar{\chi}_1}{r^2} + \frac{k_r (1 + 2\bar{\chi})}{r} \right) D_{\text{eff}} + 2 \frac{\chi_1 \bar{\zeta}}{\lambda_1} \frac{n^2 k_r}{r^3 \, (k_r^2 + r^{-2})}, \tag{3.88a}$$

$$\operatorname{Im} \sigma_- = -\lambda_1 p_0 k_r - 2 \frac{\chi_1 \bar{\zeta}}{\lambda_1} \frac{n^2 k_r}{r^3 \, (k_r^2 + r^{-2})}. \tag{3.88b}$$

The calculation we performed here shows that the mechanisms leading to the instability of the homogeneous states extends to inhomogeneous solutions as well, taking the appropriate limits. The instability conditions (3.75) and (3.76) are thus also relevant for micelles. They are not exact, however, due to the new λ_1 / r term in the case of the mixed orientational instability, as well as the fact that real micelles have finite radius and the derivation of this section can thus only give a qualitative impression of the mechanisms at work. In the next section, we will perform numerical simulations to observe how the instabilities evolve dynamically, and to check the qualitative connection between micelle instabilities and mixed orientational instabilities we have made.

3.6.2 Micelle instabilities in simulations

To investigate these questions, we made use of the phenomenological equations (3.11) again. We started by running a simulation in a 40×40 geometry, with $\bar{\rho} = 1.1$, $D_\rho = 1/32$, $\alpha_2 = \alpha_3 = -\nu = 0.05$, $\hat{\chi}_1 = -0.15$, $\hat{\chi}_2 = \hat{\kappa}_2 = \hat{\zeta}_1 = 0$, $v_m = 0.02$, $D_m = 0.2$, and importantly $\hat{\lambda}_1 = -1.0$, $\hat{\kappa}_1 = 0.03$, $\hat{\lambda}_2 = 0$ and $\hat{\zeta}_2 = -0.1$, to obtain a stable micelle. Next, we took the obtained solutions and changed the parameters abruptly, to see whether the instabilities would be activated. While for some parameters the micelle merely adjusted its length scale, but otherwise kept its symmetry, for others it lost its stability. We observed two different instabilities, which we refer to as the fingering instability and the branching instability.

Fingering instability

Reducing the strength of the orientational self-advection to $\hat{\lambda}_1 = -0.7$, the micelle became unstable by modulating its shape, breaking the radial symmetry. The position of the density interface was modulated around the ring, selecting different node numbers in dependence on the value of $\hat{\zeta}_2$: as we increased this parameter, the node number increased as well (see Figures 27 and 28). Since we kept $\hat{\lambda}_2 = 0$ fixed, this hints at the fact that we entered the regime of the mixed density instability governed by the inequality (3.75). Indeed, as $\hat{\zeta}_2$ is increased, the term quadratic in n in eq. (3.87a) becomes more dominant. The selection of the node number of maximum growth takes place via the competition of the quadratic term with terms of higher order in n that regularise the instability, so it is not surprising that this implies a higher node number in the dynamics close to the onset.

We can thus identify the observed instability with the mixed density instability from the discussion above. Since it leads to the modulation of the density interface, it is more apt to name it *fingering instability.* Since the mixed density instability has components of the density and orientational perturbations that are of the same order (see discussion below eq. (3.74)), as the instability kicks in the density and splay perturbations grow simultaneously.

The connection between the mixed density instability from the stability analysis of the homogeneous state and the fingering instability seen in micelles explains why we find this instability in the derived model for low α (see Fig. 15). Indeed, that is the regime where the mixed density instability is found, as shown in Fig. 26c.

Branching instability

Reducing the strength of $\hat{\lambda}_1$ to $\hat{\lambda}_1 = -0.5$, increasing the self-anchoring strength to $\hat{\zeta}_2 = -0.8$ and introducing active splay by setting $\lambda_2 = -1.1$, the micelle became unstable in a different way than before. At first, the splay along the micelle was modulated, breaking the radial symmetry. At later times, the density field changed as well, creating bilayer-like throughs along the micelle ring. Thus, in contrast to what we saw in the fingering instability, the high-density ring broke up, with branches forming that extended radially outward. Thus, we refer to this micellular instability as *branching instability.*

By varying $\hat{\kappa}_1$, we could select different node numbers for this instability as well. For weaker elasticity, the node number increased (see Figures 29 and 30). Since $\hat{\lambda}_2$ was activated, and the instability kicked in at much earlier times compared to the fingering instability investigated above, this hints at the fact that this instability is related to the mixed orientational instability governed by the inequality (3.76). Indeed, as $\hat{\kappa}_1$ is decreased, the term quadratic in n in eq. (3.87b) becomes more dominant. As for the fingering instability, this results in higher node numbers because the quadratic term wins over the regularising higher-order terms for a range of n that grows larger as the quadratic term is amplified.

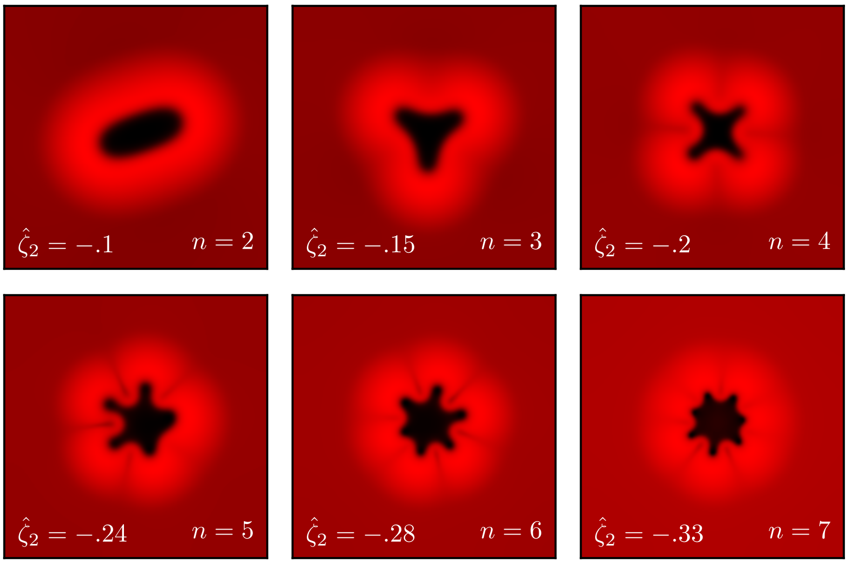

Figure 27: Micellular fingering instability in the phenomenological model. A stable micelle was prepared using the parameters indicated in sec. 3.6.2. Then, the self-advection strength was reduced to $\hat{\lambda}_1 = -0.7$ to activate the mixed density instability. By varying the strength of the self-anchoring $\hat{\zeta}_2$, different mode numbers n could be activated. The density field is shown, with brighter values signifying higher density. The range of values was normalised for each snapshot.

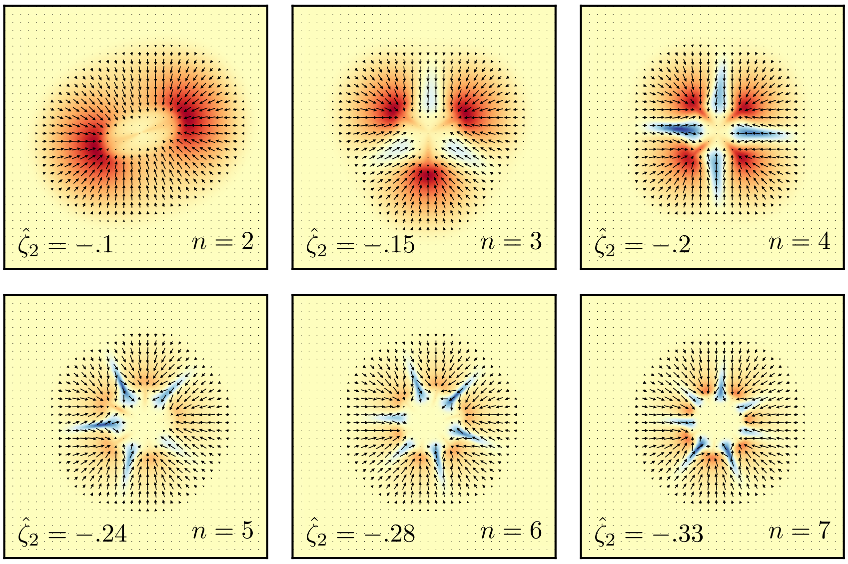

Figure 28: Polarisation field for the simulation snapshots shown in 27. The colors show the splay field $\boldsymbol{\nabla} \cdot \hat{\boldsymbol{n}}$, where $\hat{\boldsymbol{n}} = \boldsymbol{p}/|\boldsymbol{p}|$. Red corresponds to negative splay, and blue to positive splay. The color range was normalised for each snapshot.

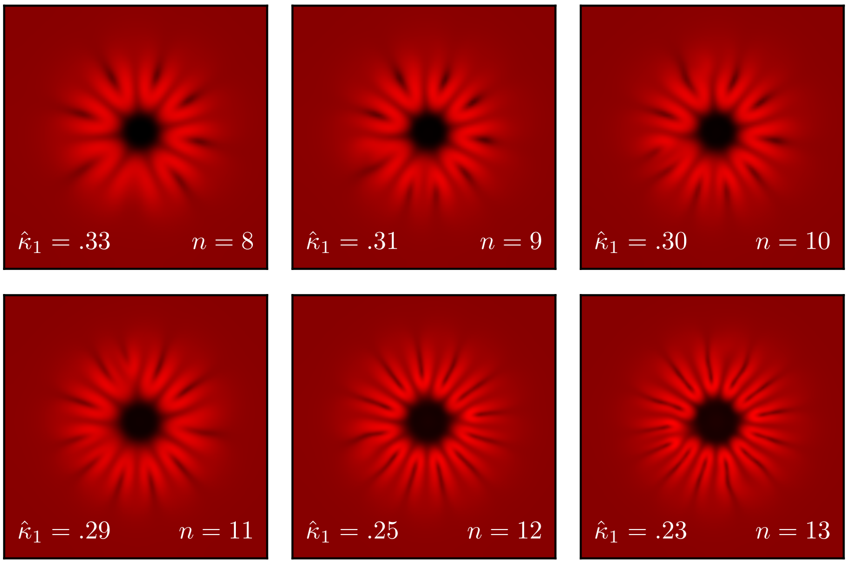

Figure 29: Micellular branching instability in the phenomenological model. The same micelle was prepared as initial condition as for the fingering instability. Then, the self-advection strength was reduced to $\hat{\lambda}_1 = -0.5$, the self-anchoring strength increased to $\hat{\zeta}_2 = -0.8$ and the active splay set to $\hat{\lambda}_2 = -1.1$ to activate the mixed orientational instability. By varying the strength of the elasticity $\hat{\kappa}_1$, different mode numbers n could be activated. Here, the density field is shown.

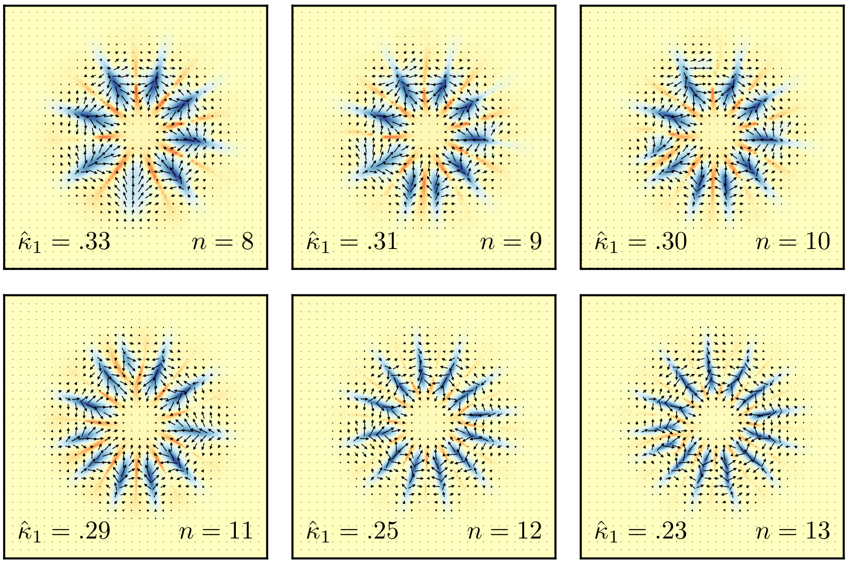

Figure 30: Polarisation field for the simulation snapshots shown in 29. The colors show the splay field $\boldsymbol{\nabla} \cdot \hat{\boldsymbol{n}}$, where $\hat{\boldsymbol{n}} = \boldsymbol{p}/|\boldsymbol{p}|$. Red corresponds to negative splay, and blue to positive splay. The color range was normalised for each snapshot.

Chapter 4

Discussion and Outlook

The goal of this thesis was to derive a mesoscopic theory for microtubule-motor mixtures from a set of microscopic interaction rules. In contrast to previous work using similar methods, which assumed either fully polar [12, 13, 23, 34] or fully symmetric interactions [14], we chose to allow for an asymmetric mixture of polar and antipolar alignment interactions in dependence on the intersection angle. This was inspired by experimental evidence suggesting that some motor proteins are able to perform different tasks depending on the initial configuration of the filaments [10, 11]. As was done for self-propelled particles in [15], we introduced this asymmetry via a critical angle parameter that controls the bias towards either kind of interaction. Furthermore, to account for stalling effects observed in [11], we included tuneable antiparallel sliding. We took into account the anisotropy of interaction at the level of single microtubules due to an inhomogeneous profile of bound molecular motors showing tip accumulation, and we discussed how the number of parameters describing this anisotropy can be reduced from two to one by taking a strong tip accumulation limit. Furthermore, we took the collective advection of motors in ordered regions into account.

Using the Boltzmann-Ginzburg-Landau formalism, we derived continuum equations for the slow variables of the system. While the density field is always a slow variable, the type of order that emerges in the system depends on the choice of the critical angle ω_c. Indeed, for a range of values centered around the perfectly symmetric case $\omega_c = \pi/2$, the nematic order is unstable above a critical density, while for larger ω_c, including the case of fully polar interaction ($\omega_c = \pi$), the polar order can becomes unstable. The two regimes intersect, such that there exists a range of values where both types of order can emerge at high enough densities. While this hints at the possibility of an interesting interplay between nematic and polar patterns, as discussed in [15], in this work we focused on the range of critical angles where one of the two orders can be adiabatically eliminated and expressed in terms of the other. Thus, we obtained two sets of continuum equations, one for the regime of nematic dominance and one for the polar regime.

In the rest of the thesis, we studied the equations for the polar regime in detail. As a first step, we performed numerical simulations to explore the phase diagram of our model as a function of the parameters of the microscopic interaction, i.e. the critical angle, the sliding strength, the anisotropy parameter and the motor Péclet number, as well as the microtubule and motor densities. In a certain parameter regime, we observed a transition between radially symmetric micelles at low microtubule densities and a non-equilibrium foam-like phase at high densities. While for low densities the radially symmetric micelles are stable, when the microtubule density is increased they undergo an instability, forming bilayer-like branches that extend outward in the radial direction. As the density is increased even more, the bilayers connect to form an active network, which over time undergoes continuous reconfiguration. We refer to this novel phase as active foam.

Active foam-like phases have been observed in the theoretical literature before: in agent-based simulations of self-propelled particles with nematic interactions [35], in continuum theories for a scalar field breaking detailed balance [36], as well as in a phenomenological model for density and nematic order [28]. These active foams differ from the phase found in our polar model by an important aspect: they are not bilayer-based. Nonetheless, understanding the relationship between our model and the foams observed previously, especially the nematic foam found in [28] (as this model is very similar to the continuum equations we derived in the nematic regime), is an interesting question to be tackled in further research.

Since our model is derived from microscopic rules, we can take two different perspectives on the micelle-foam transition. One perspective is the microscopic one, where we consider it in terms of the parameters of the interaction. The transition takes place only when the admixture of antipolar interactions is strong enough and the interaction includes sliding. This seems to be necessary to stabilise the bilayers, which are the elementary constituent of the active foam phase. Indeed, thinking about the bilayer as a combination of two monolayers of microtubules pointing in opposite directions, polar interactions are needed to align the microtubules belonging to the same monolayer, while antipolar interactions are necessary to keep the microtubules on the two opposite sides aligned along the same axis. In this picture, sliding is essential to maintain the two monolayers well separated. This illustrates the importance of studying asymmetric interaction rules: while fully polar interactions would not feature the crucial mechanism of antiparallel sliding, fully symmetric models fail to give rise to dominating polar order, which is needed to form polar structures like micelles and bilayers. Another important ingredient is the inhomogeneity of the motor field, and thus of the interaction rate. This enhances the interaction strength within the bilayer, while inhibiting it outside.

The other perspective we can take on the micelle-foam transition is the mesoscopic one, where it is interpreted in terms of a feedback mechanism among different terms in the continuum equations leading to an instability. With this in mind, we performed a linear stability analysis of the homogeneous states, and we showed that the instabilities derived in this setting are relevant for micelles as well. This allowed us to identify the mechanism that is responsible for the micellular branching instability, namely a feedback between the active splay and self-anchoring terms in the polarisation equation. Since a different microscopic model for the same system will lead to continuum equations that have the same form but a different dependence of the coefficients on microscopic parameters, this perspective is more general than the microscopic one. On one hand, it applies to phenomenological models as well, which can be useful when a rigorous derivation like the one we performed is not possible, and on the other hand it formulates a constraint that microscopic models need to fulfil to reproduce the sought phenomenology. If the branching instability is to be reproduced, for example, the active splay and the self-anchoring need to have different signs. Microscopic models that do not fulfil this condition will not show branching micelles.

The micelle-foam transition we observed in our model is reminiscent of recent experimental discoveries. Investigating mixtures of kinesin-4 motors and microtubules, it was found that a number of non-equilibrium phases emerge, including asters at low tubulin concentrations and active foams with bilayer edges at high tubulin concentrations ([1], see Fig. 1c). While the geometry of these experiments is three-dimensional, the fact that we found such a transition in our model suggests that the two-dimensional equations already capture the key mechanism necessary for the transition. Indeed, the branching instability we have identified as driving the micelle-foam transition can be generalised to three dimensions. Nevertheless, to achieve full correspondence between theory and experiment, the formulation of a three-dimensional model might be required. In principle, this is feasible by applying the Boltzmann-Ginzburg-Landau procedure in three dimensions, as was done for Vicsek-like models in [37].

In addition to the branching instability, the linear stability analysis we performed also predicts a micellular fingering instability. This relies on a different feedback mechanism (involving self-advection, anchoring and splay/bend fluxes) on the mesoscopic level, and occurs in a different regime of phase space in terms of the microscopic parameters, i.e. at low microtubule but high motor concentrations. Theoretically, a similar fingering instability has been discussed for active polar monolayers [38] as well as active nematic droplets [39]. However, the mechanism of the instability there is quite different, since the order is not acquired by a Ginzburg-Landau transition, but instead imposed by interfacial anchoring, which gives rise to the instability in combination with contractile active stresses.

Moreover, we investigated the emergence of the inner length scales in micelles and bilayers. Numerical simulations showed that micelles can "open up", showing a large depleted centre which sets them apart from the asters found in previous theoretical studies. This is reminiscent of structures seen in experiments ([5], see Fig. 1a). By examining stationary solutions of our continuum model, we found that the length scale selection in bilayer and micelle profiles is a result of the competition between various terms in the equations: between elasticity and ordering, between anchoring and self-advection, between contractile and diffusive fluxes. In micelles, due to the splay emerging as a consequence of the radial symmetry, the splay flux and the active splay play a role as well and lead to a larger length scale compared to the bilayer. Examining the length scales as a function of the physical parameters appearing in the derived model, we found that for high motor concentrations the length scale of the depleted centre of the micelle is increased, confirming the results of numerical simulations. A similar observation was made in agent-based simulations for a system of microtubules with cross-linking motor proteins: as the concentration of motor proteins was increased, the centres of the micelle-like structures opened up [32]. This correspondence raises the question whether other properties of our model, like the micelle-foam transition, can be reproduced in agent-based simulations as well.

Several open questions remain to be investigated. Our model is fully deterministic, and it might be interesting to introduce noise terms into the continuum equations to investigate stochastic effects. Furthermore, an open research question is the role of the microtubule length: while the work presented in this thesis demonstrates that the phases observed experimentally can be reproduced even in a population with fixed microtubule length, it is unclear how a finite-variance microtubule length distribution that can potentially evolve in time affects the physics. On the level of the microscopic interaction rules, the model allows room for refinement: for example, studying the effect of a dependence of the interaction parameters on microtubule and motor concentrations could be of interest.

Our work sets the scene for a higher-level investigation of polar active foams. Using our phenomenological model as a starting point, a minimal model facilitating the analytical treatment of these novel structures could be formulated. This would make it possible to study the mechanisms responsible for foam activity, as well as the emergence of geometric properties of the foam such as the cell size distribution and the vertex degree distribution. Finally, it is an interesting question whether our polar active foams and the nematic foams proposed in [28] can be described by a unified theory, and whether foams with coexisting orders can exist.

Bibliography

[1] B. Lemma, N. P. Mitchell, R. Subramanian, D. J. Needleman, and Z. Dogic, "Active microphase separation in mixtures of microtubules and tip-accumulating molecular motors," *Phys. Rev. X*, vol. 12, p. 031006, 2022.

[2] D. Needleman and Z. Dogic, "Active matter at the interface between materials science and cell biology," *Nature Reviews Materials*, vol. 2, no. 9, p. 17048, 2017.

[3] R. A. Cross and A. McAinsh, "Prime movers: the mechanochemistry of mitotic kinesins," *Nature Reviews Molecular Cell Biology*, vol. 15, no. 4, pp. 257–271, 2014.

[4] M. Dogterom and T. Surrey, "Microtubule organization in vitro," *Current Opinion in Cell Biology*, vol. 25, no. 1, pp. 23–29, 2013. Cell architecture.

[5] T. J. Mitchison, P. Nguyen, M. Coughlin, and A. C. Groen, "Self-organization of stabilized microtubules by both spindle and midzone mechanisms in xenopus egg cytosol.," *Mol Biol Cell*, vol. 24, no. 10, pp. 1559–1573, 2013.

[6] F. J. Nédélec, T. Surrey, A. C. Maggs, and S. Leibler, "Self-organization of microtubules and motors," *Nature*, vol. 389, no. 6648, pp. 305–308, 1997.

[7] K. E. Sawin, K. LeGuellec, M. Philippe, and T. J. Mitchison, "Mitotic spindle organization by a plus-end-directed microtubule motor.," *Nature*, vol. 359, no. 6395, pp. 540–543, 1992.

[8] H. Youn Lee and M. Kardar, "Macroscopic equations for pattern formation in mixtures of microtubules and molecular motors," *Phys. Rev. E*, vol. 64, p. 056113, 2001.

[9] K. S. Burbank, T. J. Mitchison, and D. S. Fisher, "Slide-and-cluster models for spindle assembly," *Current Biology*, vol. 17, no. 16, pp. 1373–1383, 2007.

[10] L. C. Kapitein, E. J. G. Peterman, B. H. Kwok, J. H. Kim, T. M. Kapoor, and C. F. Schmidt, "The bipolar mitotic kinesin eg5 moves on both microtubules that it crosslinks," *Nature*, vol. 435, no. 7038, pp. 114–118, 2005.

[11] S. Wijeratne and R. Subramanian, "Geometry of antiparallel microtubule bundles regulates relative sliding and stalling by prc1 and kif4a," *eLife*, vol. 7, p. e32595, 2018.

[12] I. S. Aranson and L. S. Tsimring, "Pattern formation of microtubules and motors: Inelastic interaction of polar rods," *Phys. Rev. E*, vol. 71, p. 050901(R), 2005.

[13] I. S. Aranson and L. S. Tsimring, "Theory of self-assembly of microtubules and motors," *Phys. Rev. E*, vol. 74, p. 031915, 2006.

[14] I. Maryshev, A. B. Goryachev, D. Marenduzzo, and A. Morozov, “Dry active turbulence in a model for microtubule–motor mixtures,” *Soft Matter*, vol. 15, pp. 6038–6043, 2019.

[15] J. Denk and E. Frey, “Pattern-induced local symmetry breaking in active-matter systems,” *PNAS*, vol. 117, pp. 31623–31630, 2020.

[16] M. C. Marchetti, J. F. Joanny, S. Ramaswamy, T. B. Liverpool, J. Prost, M. Rao, and R. A. Simha, “Hydrodynamics of soft active matter,” *Rev. Mod. Phys.*, vol. 85, p. 1143, 2007.

[17] A. Peshkov, I. S. Aranson, E. Bertin, H. Chaté, and F. Ginelli, “Boltzmann-Ginzburg-Landau approach for continuous descriptions of generic Vicsek-like models,” *Phys. Rev. Lett.*, vol. 109, p. 268701, 2014.

[18] T. B. Liverpool and M. C. Marchetti, “Instabilities of isotropic solutions of active polar filaments,” *Phys. Rev. Lett.*, vol. 90, p. 138102, 2003.

[19] T. B. Liverpool and M. C. Marchetti, “Bridging the microscopic and the hydrodynamic in active filament solutions,” *Europhysics Letters (EPL)*, vol. 69, no. 5, pp. 846–852, 2005.

[20] A. Ahmadi, T. B. Liverpool, and M. C. Marchetti, “Nematic and polar order in active filament solutions,” *Phys. Rev. E*, vol. 72, p. 060901(R), 2005.

[21] A. Ahmadi, M. C. Marchetti, and T. B. Liverpool, “Hydrodynamics of isotropic and liquid crystalline active polymer solutions,” *Phys. Rev. E*, vol. 74, p. 061913, 2006.

[22] F. Ziebert and W. Zimmermann, “Nonlinear competition between asters and stripes in filament-motor systems,” *The European Physical Journal E*, vol. 18, no. 1, pp. 41–54, 2005.

[23] I. Maryshev, D. Marenduzzo, A. B. Goryachev, and A. Morozov, “Kinetic theory of pattern formation in mixtures of microtubules and molecular motors,” *Phys. Rev. E*, vol. 97, p. 022412, 2018.

[24] H. Chaté and B. Mahault, “Dry, aligning, dilute, active matter: A synthetic and self-contained overview,” 2019, arXiv:1906.05542.

[25] H. Chaté, “Dry aligning dilute active matter,” *Annual Review of Condensed Matter Physics*, vol. 11, no. 1, pp. 189–212, 2020.

[26] C. Leduc, K. Padberg-Gehle, V. Varga, D. Helbing, S. Diez, and J. Howard, “Molecular crowding creates traffic jams of kinesin motors on microtubules.,” *Proc Natl Acad Sci U S A*, vol. 109, no. 16, pp. 6100–6105, 2012.

[27] B. A. Bezuglyi, N. A. Ivanova, and L. V. Sizova, “Transport phenomena and dimensionless numbers: towards a new methodological approach,” *European Journal of Physics*, vol. 38, no. 3, p. 033001, 2017.

[28] I. Maryshev, A. Morozov, A. B. Goryachev, and D. Marenduzzo, “Pattern formation in active model C with anchoring: bands, aster networks, and foams,” *Soft Matter*, vol. 16, pp. 8775–8781, 2020.

[29] J. Toner and Y. Tu, "Flocks, herds, and schools: A quantitative theory of flocking," *Phys. Rev. E*, vol. 58, p. 4828, 1998.

[30] E. M. Terentjev and D. A. Weitz, *The Oxford Handbook of Soft Condensed Matter*. Oxford University Press, 2015.

[31] J. W. Cahn and J. E. Hilliard, "Free energy of a nonuniform system. i. interfacial free energy," *The Journal of Chemical Physics*, vol. 28, no. 2, pp. 258–267, 1958.

[32] S. Ansari, W. Yan, A. R. Lamson, M. J. Shelley, M. A. Glaser, and M. D. Betterton, "Active condensation of filaments under spatial confinement," *Frontiers in Physics*, vol. 10, 2022.

[33] M. C. Cross and P. C. Hohenberg, "Pattern formation outside of equilibrium," *Rev. Mod. Phys. 65, 851*, vol. 65, pp. 851–1112, 1993.

[34] F. Ziebert, I. S. Aranson, and L. S. Tsimring, "Effects of cross-links on motor-mediated filament organization," *New Journal of Physics*, vol. 9, p. 421, 2007.

[35] K. H. Nagai, Y. Sumino, R. Montagne, I. S. Aranson, and H. Chaté, "Collective motion of self-propelled particles with memory," *Phys. Rev. Lett.*, vol. 114, p. 168001, 2015.

[36] G. Fausti, E. Tjhung, M. E. Cates, and C. Nardini, "Capillary interfacial tension in active phase separation," *Phys. Rev. Lett.*, vol. 127, p. 068001, 2021.

[37] B. Mahault, A. Patelli, and H. Chaté, "Deriving hydrodynamic equations from dry active matter models in three dimensions," *Journal of Statistical Mechanics: Theory and Experiment*, vol. 2018, no. 9, p. 093202, 2018.

[38] R. Alert, C. Blanch-Mercader, and J. Casademunt, "Active fingering instability in tissue spreading," *Phys. Rev. Lett.*, vol. 122, p. 088104, 2019.

[39] R. Alert, "Fingering instability of active nematic droplets," *Journal of Physics A: Mathematical and Theoretical*, vol. 55, no. 23, p. 234009, 2022.

Appendix

A.1 Ordering transitions in the derived model

Using the following integral:

$$\int \mathrm{d}\omega \sin\omega \cos(a\omega) = \begin{cases} [\cos\omega\cos(a\omega) + a\sin\omega\sin(a\omega)]/(a^2-1) & \text{for } a \neq \pm 1 \\ -\cos(2\omega)/4 & \text{else,} \end{cases} \tag{A.1}$$

we can write the integrals introduced in eq. (2.39) as:

$$I_\omega^{\mathrm{pol}}(k) = \begin{cases} 1/2(1-\cos(2\omega_c)) = \sin^2\omega_c & \text{for } k = \pm 2, \\ \frac{4}{k^2-4}[2\cos\omega_c\cos(k\omega_c/2) + k\sin\omega_c\sin(k\omega_c/2) - 2] & \text{for } k \neq \pm 2, \end{cases}$$

$$I_\omega^{\mathrm{apol}}(k) = \begin{cases} 1/2(\cos(2\omega_c) - 1) = -\sin^2\omega_c & \text{for } k = \pm 2, \\ -\frac{4}{k^2-4}[2\cos\omega_c\cos(k\omega_c/2) + k\sin\omega_c\sin(k\omega_c/2) + 2(-1)^{k/2}] & \text{for } k \neq \pm 2 \text{ even,} \end{cases}$$

$$I_\omega^{\mathrm{loss}}(k) = \begin{cases} -4/(k^2-1) & \text{for } k \text{ even,} \\ 0 & \text{for } k \text{ odd.} \end{cases}$$

We now inspect the expression found in the round bracket in eq. (2.41) for different values of k:

$$2I_\omega^{\mathrm{pol}}(k) + (-1)^{k/2}(1+(-1)^k)I_\omega^{\mathrm{apol}}(k) - I_\omega^{\mathrm{loss}}(k) - 4. \tag{A.2}$$

Note that for $k = 0$ (density equation), this vanishes due to mass conservation.

Polar ordering transition

For $k = \pm 1$ (polar order), the expression (A.2) yields:

$$\begin{aligned} 2I_\omega^{\mathrm{pol}}(1) - 4 &= -2\frac{8\cos\omega_c\cos(\omega_c/2) + 4\sin\omega_c\sin(\omega_c/2) - 8 + 12}{3} \\ &= \frac{4}{3}\left(1 - 3\cos\frac{\omega_c}{2} - \cos\frac{3\omega_c}{2}\right). \end{aligned}$$

This expression is positive for a certain range of ω_c, in which an ordering transition occurs above the critical density $\rho_c^{(p)}$ given in eq. (2.43a).

Nematic ordering transition

For $k = \pm 2$ (nematic order), (A.2) reads:

$$2I_\omega^{\text{pol}}(2) - 2I_\omega^{\text{apol}}(2) - I_\omega^{\text{loss}}(2) - 4 = 4\sin^2\omega_c - \frac{8}{3}.$$

Since $4 > 8/3$, this can be positive for a certain range of ω_c. There, an ordering transition occurs above the critical density $\rho_c^{(n)}$ given in eq. (2.43b).

Absence of ordering transitions for higher Fourier modes

For $|k| > 2$, the expression (A.2) is always negative, so that no ordering transition occurs no matter how high the density.

Indeed, for odd $|k| > 1$, (A.2) gives:

$$2I_\omega^{\text{pol}}(k) - 4 = \frac{16\cos\omega_c\cos(k\omega_c/2) + 8k\sin\omega_c\sin(k\omega_c/2) - 4k^2}{k^2 - 4}$$

This is always negative. Indeed, for $k = \pm 3$, using $\cos(x - y) = \cos x\cos y - \sin x\sin y$, the nominator reads:

$$16\cos(\omega_c/2) + 8\sin\omega_c\sin(3\omega_c/2) - 36 \leq 24 - 36 < 0,$$

and for $|k| \geq 5$:

$$16\cos\omega_c\cos(k\omega_c/2) + 8k\sin\omega_c\sin(k\omega_c/2) - 4k^2 \leq 16 + 4(2 - k)k < 0.$$

As for the even ks, for $|k| > 2$ multiples of 4 we find:

$$2(I_\omega^p(k) + I_\omega^{\text{apol}}(k)) - I_\omega^{\text{loss}}(k) - 4 = -\frac{32}{k^2 - 4} - 4\frac{k^2 - 2}{k^2 - 1} < 0,$$

while for even $|k| > 2$ which are not multiples of 4, (A.2) yields:

$$\begin{aligned}
&2(I_\omega^p(k) - I_\omega^{\text{apol}}(k)) - I_\omega^{\text{loss}}(k) - 4 \\
&= 4\frac{8\cos\omega_c\cos(\omega_c/2) + 2\sin\omega_c\sin(\omega_c/2) - 2 - k^2}{k^2 - 4} - \frac{4}{k^2 - 1} \\
&< 4\frac{8 - k^2}{k^2 - 4} < 0.
\end{aligned}$$

A.2 Example of a collision integral with spatial dependence

As an example for how the calculation of the collision integrals from eq. (2.31) is performed in the general case, when the spatial dependence of the PDFs is not neglected, we want to examine the terms linear in η and quadratic in $\boldsymbol{p}$ that emerge in the $\partial_t\boldsymbol{p}$ equation from the collision integral. Since $p \sim \epsilon$ and $\partial_i \sim \epsilon$ in the closure scheme presented in sec. 2.2.4, and we are expanding the polarisation equation up to $\mathcal{O}(\epsilon^3)$, we only need to consider contributions with up to one gradient.

The only dependence on η lies in the antipolar gain integral (2.31b), so this is the only one we need to take into account. Plugging in the gradient expansion (2.55), and neglecting terms of second order in the gradients, we find:

$$
\begin{aligned}
I^{\mathrm{ap}}_{\mathrm{gain}} &= \int_{\omega_c}^{2\pi-\omega_c} \mathrm{d}\omega \int\limits_{W(\phi+\pi/2,\omega)} \mathrm{d}^2 s\, P\left(\boldsymbol{r} + \frac{\eta L \bar{\boldsymbol{n}}_\perp - \boldsymbol{s}}{2}; \phi_- + \frac{\pi}{2}\right) P\left(\boldsymbol{r} + \frac{\eta L \bar{\boldsymbol{n}}_\perp + \boldsymbol{s}}{2}; \phi_+ + \frac{\pi}{2}\right) \\
&= \int_{\omega_c}^{2\pi-\omega_c} \mathrm{d}\omega \int\limits_{W(\phi+\pi/2,\omega)} \mathrm{d}^2 s \left[P_- P_+ + \frac{1}{2} P_- \left(\eta L \bar{\boldsymbol{n}}_\perp + \boldsymbol{s}\right) \cdot \boldsymbol{\nabla} P_+ + \frac{1}{2} P_+ \left(\eta L \bar{\boldsymbol{n}}_\perp - \boldsymbol{s}\right) P_-\right] \\
&= \int_{\omega_c}^{2\pi-\omega_c} \mathrm{d}\omega \left[I_s^W(0,0) P_- P_+ + \frac{1}{2} P_- (I_s^W(1,0)\partial_\parallel + (\eta L \cdot I_s^W(0,0) + I_s^W(0,1))\partial_\perp) P_+ \right. \\
&\qquad\qquad \left. + \frac{1}{2} P_- (-I_s^W(1,0)\partial_\parallel + (\eta L \cdot I_s^W(0,0) - I_s^W(0,1))\partial_\perp) P_+ \right].
\end{aligned}
$$

For readability, we introduced the shorthands $P_\pm = P\left(\boldsymbol{r}; \phi_\pm + \frac{\pi}{2}\right)$, as well as $\partial_\parallel = \hat{\boldsymbol{n}}(\phi + \pi/2) \cdot \boldsymbol{\nabla}$ and $\partial_\perp = \hat{\boldsymbol{n}}_\perp(\phi + \pi/2) \cdot \boldsymbol{\nabla}$. Note that $\bar{\boldsymbol{n}}_\perp = \hat{\boldsymbol{n}}_\perp(\phi + \pi/2) = \hat{\boldsymbol{n}}(\phi)$ holds. We now focus on the contribution linear in η. Using the value of $I_s^W(0,0)$ from the table in sec. 2.2.6 of the main text, it reads:

$$
\begin{aligned}
I^{(\eta)} &= \frac{\eta L}{2} \int_{\omega_c}^{2\pi-\omega_c} \mathrm{d}\omega I_s^W(0,0)(P_- \partial_\perp P_+ + P_+ \partial_\perp P_-) \\
&= Gm \frac{(1+a_1)\eta L^3}{2} \int_{\omega_c}^{2\pi-\omega_c} \mathrm{d}\omega |\sin\omega| (P_-(\hat{\boldsymbol{n}}(\phi) \cdot \boldsymbol{\nabla}) P_+ + P_+(\hat{\boldsymbol{n}}(\phi) \cdot \boldsymbol{\nabla}) P_-).
\end{aligned}
$$

Plugging in the Fourier transform (2.33) for $P_\pm$ as well as $I^{(\eta)}$, and abbreviating $P_k(\boldsymbol{r}) = P_k$, we obtain:

$$
\begin{aligned}
\frac{\sum_k e^{ik\phi} I_k^{(\eta)}}{(1+a_1)GL^3 m} &= \eta \sum_{k,q} e^{i(k+q)(\phi+\pi/2)} P_k \int_{\omega_c}^{2\pi-\omega_c} \mathrm{d}\omega |\sin\omega| \cos\frac{(k-q)\omega}{2} (\hat{\boldsymbol{n}}(\phi) \cdot \boldsymbol{\nabla}) P_q \\
&= \frac{\eta}{2} \sum_{k,q} e^{i(k+q)(\phi+\pi/2)} I_\omega^{(\eta)}(k,q) P_k (e^{i\phi}\nabla_+ + e^{-i\phi}\nabla_-) P_q, \qquad \text{(A.3)}
\end{aligned}
$$

where the integral $I_\omega^{(\eta)}(k,q)$ reads:

$$
\begin{aligned}
I_\omega(k,q) &= \int_{\omega_c}^{2\pi-\omega_c} \mathrm{d}\omega |\sin\omega| \cos\frac{(k-q)\omega}{2} \\
&= \int_{\omega_c}^{\pi} \mathrm{d}\omega \sin\omega \cos\frac{(k-q)\omega}{2} - \int_{\pi}^{2\pi-\omega_c} \mathrm{d}\omega \sin\omega \cos\frac{(k-q)\omega}{2} \\
&= \int_{\omega_c}^{\pi} \mathrm{d}\omega \sin\omega \cos\frac{(k-q)\omega}{2} + \int_{-2\pi+\omega_c}^{-\pi} \mathrm{d}\omega \sin\omega \cos\frac{(k-q)\omega}{2} \\
&= \begin{cases} 2\int_{\omega_c}^{\pi} \mathrm{d}\omega \sin\omega \cos\frac{(k-q)\omega}{2} & \text{for } k-q \text{ even} \\ 0 & \text{for } k-q \text{ odd.} \end{cases}
\end{aligned}
$$

To obtain the contribution to the $\partial_t \boldsymbol{p}$ equation, we project out the (-1)-st Fourier mode in (A.3). This gives:

$$I_{-1}^{(\eta)} = Gm(1+a_1)\frac{\eta L^3}{2}\sum_k \left[I_\omega(k,-k)P_k \nabla_- P_{-k} - I_\omega(k,-k-2)P_k \nabla_+ P_{-k-2}\right]. \tag{A.4}$$

First, consider the ∇_- term. The terms quadratic in $\boldsymbol{p}$ have $k=\pm 1$. Note that:

$$I_\omega^{(\eta)}(\pm 1, \mp 1) = 2\int_{\omega_c}^{\pi} \sin\omega\cos\omega = -\sin^2\omega_c.$$

Thus, the terms with $k=\pm 1$ from the sum in eq. (A.4) read:

$$-\sin^2\omega_c \left[P_1 \nabla_- P_{-1} + P_{-1}\nabla_- P_1\right].$$

This contributes to $\partial_t P_{-1}$. To obtain the contribution to the $\boldsymbol{p}$ equation, we have to take the real and imaginary part of this, as follows from the definitions in eq. (2.34). We write $2\pi P_{\pm 1} = p_x \mp i p_y$, and obtain:

$$\begin{aligned}(2\pi)^2[P_1\nabla_- P_{-1} + P_{-1}\nabla_- P_1] &= (p_x - ip_y)(\partial_x + i\partial_y)(p_x + ip_y)\\ &\quad + (p_x + ip_y)(\partial_x + i\partial_y)(p_x - ip_y)\\ &= 2\left[(p_x\partial_x p_x + p_y\partial_x p_y) + i(p_y\partial_y p_y + p_x\partial_y p_x)\right]\\ &= \partial_x p^2 + i\partial_y p^2.\end{aligned}$$

Rescaling space, time and the fields as indicated in (2.37), this results in a contribution to the $\partial_t \boldsymbol{p}$ equation that reads:

$$\partial_t \boldsymbol{p} = \cdots - m(1+a_1)\eta\frac{\sin^2\omega_c}{4\pi}\boldsymbol{\nabla} p^2, \tag{A.5}$$

and affects $\tilde{\zeta}_2$ in eq. (2.62).

Now we consider the ∇_+ term in eq. (A.4), and $k=-1$ to extract the term quadratic in $\boldsymbol{p}$. The integral gives:

$$I_\omega^{(\eta)}(-1,-1) = 2\int_{\omega_c}^{\pi}\sin\omega = 2(1+\cos\omega_c).$$

We write the relevant expression in terms of the polarisation:

$$\begin{aligned}(2\pi)^2 P_{-1}\bar{\nabla}P_{-1} &= (p_x + ip_y)(\partial_x - i\partial_y)(p_x + ip_y)\\ &= [(p_x\partial_x p_x + p_y\partial_y p_x + p_x\partial_y p_y - p_y\partial_x p_y)\\ &\qquad + i(p_y\partial_x p_x - p_x\partial_y p_x + p_y\partial_y p_y + p_x\partial_x p_y)].\end{aligned}$$

Plugging this into eq. (A.4), this gives rise to the following terms in $\partial_t \boldsymbol{p}$, which contribute to $\tilde{\zeta}_2$ as well as $\tilde{\lambda}_{1,2}$ in eq. (2.62):

$$\partial_t \boldsymbol{p} = \cdots + \frac{m(1+a_1)\eta}{2\pi}\left(\frac{1}{2}\boldsymbol{\nabla} p^2 - (\boldsymbol{p}\cdot\boldsymbol{\nabla})\boldsymbol{p} - (\boldsymbol{\nabla}\cdot\boldsymbol{p})\boldsymbol{p}\right). \tag{A.6}$$

A.3 Coefficients in the Derived Model

Density equation

$$D_\rho = \frac{1}{32} \quad D_Q = \frac{1}{96}, \qquad \alpha_2 = \frac{\alpha}{32\pi}, \quad \alpha_3 = \frac{\alpha^2}{192\pi},$$

$$\nu = (1+a_1)\frac{\cos^2\frac{\omega_c}{2}}{8\pi}\eta^2 - \frac{1+a_3}{48\pi}, \qquad \tilde{\chi}_1 = -(1+a_1)\frac{\cos^2\frac{\omega_c}{2}}{4\pi}\eta^2,$$

$$\tilde{\chi}_Q = (1+a_1)\frac{\sin^2\omega_c}{16\pi}\eta^2\bar{\rho} - \frac{1+a_3}{72\pi}\bar{\rho}, \qquad \tilde{\chi}_2 = (1+a_1)\frac{\cos\omega_c\cos^2\frac{\omega}{2}}{8\pi}\eta^2.$$

Polarisation equation

$$\rho_c^{(p)} = \frac{3\pi}{2(1+a_1)\left[1 - 3\cos\left(\frac{\omega_c}{2}\right) - \cos\left(\frac{3\omega_c}{2}\right)\right]}, \quad \tilde{\beta}^{(p)} = \frac{4\left[7 - 15\cos\frac{\omega_c}{2} + 3\cos\frac{5\omega_c}{2}\right]}{30\pi}(1+a_1),$$

$$\tilde{\kappa}_1 = \frac{5}{192}, \quad \tilde{\kappa}_2 = \frac{1}{96},$$

$$\tilde{\kappa}_1' = \left(\frac{24 - 20\cos\frac{\omega_c}{2} - 5\cos\frac{3\omega_c}{2} + \cos\frac{5\omega_c}{2}}{960\pi}(1+a_3) - \frac{5 + 4\cos\omega_c - \cos(2\omega_c)}{256\pi}a_2\eta\right)\bar{\rho}$$

$$\tilde{\kappa}_2' = \left(\frac{8 - 5\cos\frac{3\omega_c}{2} - 3\cos\frac{5\omega_c}{2}}{1440\pi}(1+a_3) - \frac{5 + 4\cos\omega_c - \cos(2\omega_c)}{128\pi}a_2\eta\right)\bar{\rho}$$

$$\tilde{\zeta}_1 = 2\left(-\frac{1}{16\pi}a_2 + \frac{1+\cos\omega_c}{4\pi}(1+a_1)\eta\right)\bar{\rho}$$

$$\tilde{\zeta}_2 = -\frac{1}{48\pi}a_2 + \frac{1 + 2\cos\omega_c + \cos(2\omega_c)}{8\pi}(1+a_1)\eta$$

$$\tilde{\lambda}_1 = -\left(\frac{27 - 30\cos\frac{\omega_c}{2} - 5\cos\frac{3\omega_c}{2} + 3\cos\frac{5\omega_c}{2}}{120\pi}a_2 - \frac{1+\cos\omega_c}{2\pi}(1+a_1)\eta\right)$$

$$\tilde{\lambda}_2 = -\left(\frac{3 + 30\cos\frac{\omega_c}{2} + 5\cos\frac{3\omega_c}{2} - 3\cos\frac{5\omega_c}{2}}{120\pi}a_2 - \frac{1+\cos\omega_c}{2\pi}(1+a_1)\eta\right)$$

$$\tilde{\lambda}_Q = \left(\frac{-22 + 30\cos\frac{\omega_c}{2} + 5\cos\frac{3\omega_c}{2} - 3\cos\frac{5\omega_c}{2}}{240\pi}a_2 + \frac{1 - \cos(2\omega_c)}{8\pi}(1+a_1)\eta\right)\bar{\rho}.$$

Nematic tensor equation

$$\rho_c^{(n)} = \frac{12\pi}{-(1+a_1)[1 + 3\cos(2\omega_c)]}, \quad \beta^{(n)} = \frac{(1+a_1)^2(3 + 10\cos(2\omega_c) - 5\cos(4\omega_c))}{24\pi[5\pi + \bar{\rho}(1+a_1)]}$$

$$\tilde{\kappa}_Q = \frac{1}{32}, \quad \tilde{\zeta}_Q = \frac{1}{192} \quad \tilde{\kappa}_Q' = \frac{11 - 3\cos(2\omega_c)}{288\pi}(1+a_3)\bar{\rho} + \frac{1 - 2\cos(2\omega_c)}{32\pi}(1+a_1)\eta^2\bar{\rho}$$

$$\tilde{\zeta}_Q' = -\frac{5 + 3\cos(2\omega_c)}{576\pi}(1+a_3)\bar{\rho} + \frac{1+\cos\omega_c}{16\pi}(1+a_1)\eta^2\bar{\rho}$$

$$\zeta_P = -\frac{7 + 12\cos\omega_c - 3\cos(2\omega_c)}{96\pi}a_2\bar{\rho}, \quad g_P = -\frac{2(1+a_1)\cos\omega_c}{\pi}$$

A.4 Equations in polar coordinates

Using the following expressions from vector analysis:

$$\begin{aligned}
\boldsymbol{\nabla} f &= \partial_r f \hat{\boldsymbol{e}}_r + r^{-1}\partial_\phi f \hat{\boldsymbol{e}}_\phi, \\
\nabla^2 f &= r^{-1}\partial_r(r\partial_r f) + r^{-2}\partial_\phi^2 f, \\
\boldsymbol{\nabla}\cdot\boldsymbol{v} &= r^{-1}\partial_r(r v_r) + r^{-1}\partial_\phi v_\phi, \\
\nabla^2 \boldsymbol{v} &= [\nabla^2 v_r - r^{-2}(v_r + 2\partial_\phi v_\phi)]\hat{\boldsymbol{e}}_r + [\nabla^2 v_\phi - r^{-2}(v_\phi - 2\partial_\phi v_r)]\hat{\boldsymbol{e}}_\phi, \\
(\boldsymbol{v}\cdot\boldsymbol{\nabla})\boldsymbol{w} &= [v_r\partial_r w_r + r^{-1}(v_\phi\partial_\phi w_r - v_\phi w_\phi)]\hat{\boldsymbol{e}}_r + [v_r\partial_r w_\phi + r^{-1}(v_\phi\partial_\phi w_\phi + v_\phi w_r)]\hat{\boldsymbol{e}}_\phi,
\end{aligned}$$

we can rewrite the equations (2.64) in polar coordinates. In the ρ equation, all terms are trivial but the χ_1 term, which for constant m reads:

$$\begin{aligned}
\partial_i\partial_j(p_i p_j) &= \boldsymbol{\nabla}\cdot[(\boldsymbol{\nabla}\cdot\boldsymbol{p})\boldsymbol{p} + (\boldsymbol{p}\cdot\boldsymbol{\nabla})\boldsymbol{p}] \\
&= \partial_r^2 p_r^2 + \frac{2\partial_r p_r^2 - \partial_r p_\phi^2 + 2\partial_\phi\partial_r(p_r p_\phi)}{r} + \frac{2\partial_\phi(p_r p_\phi) + \partial_\phi^2 p_\phi^2}{r^2}. \qquad \text{(A.7)}
\end{aligned}$$

The p equations read:

$$\begin{aligned}
\partial_t p_r = {} & \left[(m\rho/\rho_c - 1) - \beta m^2 p^2\right] p_r \\
& + \kappa_1[\partial_r^2 p_r + r^{-1}\partial_r p_r + r^{-2}\partial_\phi^2 p_r - r^{-2}(p_r + 2\partial_\phi p_\phi)] \\
& + \kappa_2[\partial_r^2 p_r + r^{-1}\partial_r p_r + r^{-1}\partial_r\partial_\phi p_\phi - r^{-2}(p_r + \partial_\phi p_\phi)] \\
& - \lambda_1[p_r\partial_r p_r + r^{-1}(p_\phi\partial_\phi p_r - p_\phi^2)] - \lambda_2(\partial_r p_r + r^{-1}p_r + r^{-1}\partial_\phi p_\phi)p_r \\
& + \zeta_1\partial_r\rho + \zeta_2\partial_r p^2, \qquad \text{(A.8)} \\
\partial_t p_\phi = {} & \left[(m\rho/\rho_c - 1) - \beta m^2 p^2\right] p_\phi \\
& + \kappa_1[\partial_r^2 p_\phi + r^{-1}\partial_r p_\phi + r^{-2}\partial_\phi^2 p_\phi - r^{-2}(p_\phi - 2\partial_\phi p_r)] \\
& + \kappa_2[r^{-1}\partial_r\partial_\phi p_r + r^{-2}(\partial_\phi^2 p_\phi + \partial_\phi p_r)] \\
& - \lambda_1[p_r\partial_r p_\phi + r^{-1}(p_\phi\partial_\phi p_\phi + p_r p_\phi)] - \lambda_2(\partial_r p_r + r^{-1}p_r + r^{-1}\partial_\phi p_\phi)p_\phi \\
& + \zeta_1 r^{-1}\partial_\phi\rho + \zeta_2 r^{-1}\partial_\phi p^2. \qquad \text{(A.9)}
\end{aligned}$$

Finally, the m equation reads:

$$\begin{aligned}
\partial_t m = {} & D_m r^{-1}\partial_r(r\partial_r m) + D_m r^{-2}\partial_\phi^2 m \\
& - v_m(p_r\partial_r m + r^{-1}p_\phi\partial_\phi m) \\
& - v_m m[r^{-1}\partial_r(r p_r) + r^{-1}\partial_\phi p_\phi]. \qquad \text{(A.10)}
\end{aligned}$$

Acknowledgements

Firstly, I would like to express my gratitude to Ivan Maryshev for his inspiring supervision and for the innumerable discussions, and to Prof. Erwin Frey for letting me work on this project at his chair and for his valuable guidance. Many thanks to all members of the Frey group for providing a creative and encouraging environment. I truly enjoyed my stay. A huge thank you to all my friends in Munich and across Europe for their support and affection, and to my family back in Rome for their unwavering love, which I am grateful for every day.

Selbständigkeitserklärung

Ich versichere hiermit, die vorliegende Arbeit mit dem Titel

Pattern Formation of Active Filaments with Polar and Antipolar Interactions

selbständig verfasst zu haben und keine anderen als die angegebenen Quellen und Hilfsmittel verwendet zu haben.

Filippo De Luca

München, den 17. Oktober 2022